INVESTIGATION OF ROTATING DETONATION COMBUSTION DYNAMICS USING ADVANCED IN-SITU OPTICAL DIAGNOSTICS

by

Venkatasubramanian Athmanathan

A Dissertation

Submitted to the Faculty of Purdue University

In Partial Fulfillment of the Requirements for the degree of

Doctor of Philosophy

School of Aeronautics and Astronautics

West Lafayette, Indiana

August 2021

THE PURDUE UNIVERSITY GRADUATE SCHOOL
STATEMENT OF COMMITTEE APPROVAL

Dr. Terrence R. Meyer, Co-chair

School of Mechanical Engineering
School of Aeronautics and Astronautics (by courtesy)

Dr. Mikhail N. Slipchenko, Co-chair

School of Mechanical Engineering

Dr. Timothée L. Pourpoint

School of Aeronautics and Astronautics
School of Mechanical Engineering (by courtesy)

Dr. Robert P. Lucht

School of Mechanical Engineering
School of Aeronautics and Astronautics (by courtesy)

Dr. Guillermo P. Paniagua

School of Mechanical Engineering
School of Aeronautics and Astronautics (by courtesy)

Dr. James Braun

School of Mechanical Engineering

Approved by:

Dr. Gregory A. Blaisdell

To my parents Shanthi and Athmanathan

Dr. Werner von Braun and Sergei Korolyov, two figures who inspired me to pursue a career in Aerospace Propulsion.

ACKNOWLEDGMENTS

The last four years in Dr. Terrence Meyer's group were the highlight of my graduate career at Purdue, and I am highly indebted to his guidance and mentorship. Without a doubt, Terry is that gold-standard advisor that one could ask for and words fail to explain Terry's infectious love for science and his students. I joined Terry's lab in Summer of 2017 with absolutely no knowledge of laser diagnostics but by the end of the program, I could, without hesitation, tinker, rebuild and tune lasers/camera systems as needed. Terry took me under his wing to lead the design and build-up of Test-Cell 2 and provided plenty of funds and encouragement to build a world class laser-diagnostics focused propulsion testing facility in the first two years. He knew that I had a specific interest in rotating detonation engines and just to enable my interest in studying this phenomenon, and my almost short-sighted "I think we can do it" statement, he spent a great deal of his time, effort, and money to dive into newer research territories. While things did pan out for the best, I am still perplexed the sheer magnitudes of faith Terry vests in his students to explore the forefront of propulsion research and peek into the physics of the unknown, knowing full well that things might not work at all. Our long discussions, (sometimes lasting over 4 hours) about the research problem, papers and potentially new experiments are some of the most cherished memories from my time in my PhD program.

I would also like to convey my sincere gratitude to Dr. Mikhail Slipchenko (my second advisor) hailed by my colleagues as 'laser-god'. Mikhail was instrumental in honing my experimental skills through his practical and sometimes unconventional teaching methods (which includes a good amount of "I think you need to read the Wikipedia page"). He always encouraged me to experiment with super expensive lasers systems and never let me feel the pressure of 'breaking expensive things', which could very well cost a lot and slow progress. His car certainly has a Genie sitting inside, for every time I need something or break something, just like magic, he will pull out a spare from his car! I am super happy that I will spend a few more years in his company!

My sincere thanks to Dr. Guillermo Paniagua and Dr. James Braun, both of whom also provided guidance and funds to enable this experimental work on RDCs. Especially their parallel efforts in URANS numerical simulations, a necessary tool that was instrumental in allowing me to formulate the science behind the experimental results presented in this work. I would also extend

my gratitude to Dr. Timothee Pourpoint and Dr. Robert Lucht for serving on my committee and providing guidance. I am grateful to Scott Meyer and Rob McGuire, for playing a key role helping me design good experiments during the formative years at graduate school. I would also like to thank Dr. Sukesh Roy and Dr. Chris Fugger from Spectral Energies, both of whom, just like Terry, took a leap of faith and provided extensive funding for our RDC program here at Purdue. I am glad I got to work with them, and I am looking forward to our continued interactions. I extend my gratitude to Roger Mears at Spectral Energies, for machining the RDC.

I am very lucky to have found a lab group that provided me with a cohesive, supportive, and welcoming environment and I rubbed shoulders with some of the best minds. Special shoutout to Daniel Lauriola, Zach Ayers, Alber Douglawi, Mike Smyser, Naveed Rahman, Alex Brown, Erik Braun, Austin Webb and Mateo Gomez, each of whom have helped me in numerous occasions during my PhD days. Special mention to Dr. Kazi Arafat Rahman, my close friend, mentor, and colleague who cared deeply about science. Our long discussions, almost every weekend trip to Indy for desi food and never-ending conversations over chai/food, and all-nighter experiments are cherished memories that I sorely miss.

This work would not have been possible without the unwavering and abundant support of my family and friends, especially my parents Shanthi and Athmanathan. Their love, support, patience, and belief in me provided the strongest foundation one could ever ask for and I am deeply indebted to them. My family, including Uma, Shankar, Jiju and Brahadha paati stood by me through all my low and high points and I am lucky to have their constant support. Thank you Anu, for your steady companionship through my graduate school days; your encouragement, support and love were key to helping me cross this bridge. Thanks a lot, Skanda, Shravanti, Farhan, Abhinandan, Jayakumar and Deepak for being exceptional friends. Thank you Dr. Ramgopal and Dr. Trinath; our academic conversations and otherwise, were necessary doses of inspiration. I would also like to express my gratitude to my mentors Mr. Ravi Shankar and Prof. Surendra Bogadi, their guidance played a pivotal role in helping me developing a keen sense of scientific thinking. You have indeed helped me get here.

TABLE OF CONTENTS

LIST OF TABLES

LIST OF FIGURES

ABSTRACT

Rotating detonation combustors (RDCs) provide a promising avenue for incorporating step changes in thermodynamic efficiency improvements through isochoric heat release for gas turbine and rocket propulsion systems. However, these systems have multiple challenges that need to be addressed to realize practical pressure gain systems. Chief among them is the total pressure loss, which can be caused by multiple processes including wake shock features, non-ideal detonations, heat losses, mixed-mode heat release (deflagrative and detonative) and geometry-induced flow losses. While multiple experiments in the past have used probe-based techniques and imaging systems to characterize the flow losses, very few experiments have spatio-temporally resolved the detonation structure and propagation using advanced high repetition rate optical diagnostics.

In this work, a novel high-pressure optically accessible RDC is designed and developed for implementing advanced high repetition rate qualitative and quantitative laser-based diagnostics to facilitate detailed detonation characterization in annular channels. The RDC uses axial-injection of air and radial injection of hydrogen with full optical access extending from the oxidizer injection plenum to the exit plane of the RDC. Several in-situ diagnostics are deployed to characterize the three-dimensional propagation characteristics of detonation waves and their dependence on mass flux, global equivalence ratio and geometry. In parallel to the experimental measurements, 3D Unsteady Reynolds-Averaged Navier-Stokes (URANS), simulations are performed for this geometry and were used in interpreting the experimental results.

By combining MHz-rate broadband flame chemiluminescence, MHz-rate OH planar laser-induced fluorescence (PLIF), and URANS simulations, the complex 3D features of the non-premixed detonation waves were characterized as a function of the rate of reactant mixing. Due to the large fuel/oxidizer stratification in the injection nearfield within a non-premixed RDC, the detonation in this region is relatively weak, with some unburned reactants passing through the leading detonation wave and combusting in a trailing wave stabilized behind the leading wave via an azimuthal shock-induced detonation. These results explain why the detonation in the injection near field has a characteristic dual-wave structure over a wide range of mass flow rates. Further downstream along the axial length of the RDC, the reactant mixedness improves, leading to a single-wave structure with a higher detonation strength. While the freely propagating leading detonation waves have a higher-pressure ratio across the detonation, a shock-induced trailing

detonation has a relatively lower pressure ratio. The elucidation of the physical mechanism for mixed-mode combustion of freely propagating detonation and shock-induced detonation leads to a better understanding of the origins of non-ideal flow losses in non-premixed RDCs, particularly in the context of complex shock-flow interactions occurring for due the dynamics of axial reflected shocks that also affect the detonation wave structure. These imaging studies also reveal a non-ideal cellular propagation of detonation waves around the annulus with cell sizes increasing with increasing axial distance from the injection plane.

In addition to the experimental studies having reactant injection into a stepped combustor chamber, a design with the reactants expanding fully into the annular channel via a ramped cross-section was also designed and evaluated at the same operating conditions. This design eliminates product recirculation regions induced by the backward facing step (BFS) of the stepped combustor design. The detonation wave shape drastically varied in case of the ramp inlet geometry, compared to that of the stepped inlet. Additionally, multiple trailing shock induced detonation waves were observed, which leads to an overall drop in the C-J velocity for the ramp design at the same operating conditions. However, the ramp-design provided a lower lean limit with stable operation at lean conditions compared the stepped design, highlighting the sensitivity of the detonation wave to the chamber annular geometry and the need to understand its impact on RDC performance.

To evaluate the propagation of combustion waves into the exhaust, and potentially into downstream post-combustion devices, quantitative measurements of temperature were performed in the exhaust of an RDC with a custom outlet plenum by using hybrid fs/ps rotational Coherent anti-Stokes Raman (RCARS). Through the use of URANS simulations, extensive analysis was performed to understand the uncertainty associated with RCARS in a detonating environment. The experimental and numerical results show that the temperature variation in the exhaust is ~ 300 K with both the numerical and the experimental results predicting a combustor pattern factor of ~0.20 and ~0.19 respectively, a nominal value similar to modern day Brayton cycle-based gas turbines. These results show the utility of advanced in-situ optical diagnostics for understanding the dynamics and performance implications of various RDC configurations.

1. INTRODUCTION

Rotating detonation engines (RDE) are being considered as the propulsion and power generation cycles for a new generation of gas turbines and rocket combustors because of their ability to sustain constant volume combustion in a valve-less configuration. Detonative combustion promises thermodynamic cycle efficiency improvements with the same class of fuels being used in the propulsion and power sector currently [1–4]. Hydrogen is an ideal fuel for future gas turbine engines due to its high detonability over a wide range of equivalence ratios and mass fluxes, as well as zero carbon emissions. In the current state of the art, implementation of detonative combustion is impeded by a host of challenges that need to be overcome. These challenges prevent the realization of performance increases and the maturing the technology from a research scale to large scale engine applications. Some of the challenges that are being addressed by different combustion research groups include: combustion efficiency, thermal and heat management, inlet loses through non-standard injection schemes, secondary flow loses, shock losses, prediction and control of detonation fill height, limits of detonation, prediction of detonation structure, control of direction of detonations, flashback and flame-holding in premixed zones, etc. [5–9]

The last two decades has resulted in several analysis techniques at various levels of abstractions to understand the thermodynamic advantage presented by RDCs, which improves cycle performance levels on the order of a few tens of percent. Among which, the time-independent closed-cycle analysis approach developed by Heiser and Pratt [10] provides a means to understand the upper bounds of traditional propulsion performance measures (F_{thrust}, SFC, $\eta_{thermal}$ etc.). Heiser and Pratt's model retains component level analysis of the Brayton cycle for all components (diffuser, compressor, turbine, nozzle), except for the heat addition step (combustor).

A representative T-s diagram for the detonation, constant volume and constant pressure combustion cycle is shown in Figure 1.1 (a). Station 0 -2 represents the isentropic increase in flow enthalpy from diffuser/compressor system, station 2-3 represents three different modes of combustion, and station 3-4 represents flow/expansion work output from nozzles/turbines. The detonation cycle is clearly favored over the constant pressure and constant volume cycle due to lower entropy generation at station 3 – the exit plane of the combustor. Heiser and Pratt use the constraints of a Zeldovich-von Neumann and Döring (ZND) model for the detonation wave. The ZND model assumes the detonation wave as a compound wave propagating through an

undisturbed fuel-air premixture, nearly at rest, followed by the release of sensible heat in a constant-area region (Rayleigh flow) as shown in Figure 1.1 (b).

$$\eta_{thermal} = 1 - \left[\frac{1}{M_{CJ}^2}\left(\frac{1+\gamma M_{CJ}^2}{\gamma+1}\right)^{\frac{\gamma+1}{\gamma}} - 1\right] / \dot{q} \qquad (1.1)$$

where M_{CJ} is a function of the reactant thermodynamic properties of the reactants and the heat-release from the reactants. While this analysis provides the necessary upper bounds on expected cycle efficiency, there are multiple practical considerations that need to be addressed in the design of RDCs. These include efficiency losses in the compressor, due to shocks, from incomplete combustion, and in the exhaust due to nozzle inefficiency and non-uniform thrust across the nozzle surface. Additionally, the ZND assumption of the detonation model assumes a premixed linearized detonation wave. This approach discounts that practical RDCs have non-uniformities due to stratification of the fuel-oxidizer mixture in the combustor annulus and that the detonation propagation has curved wall effects and is highly three dimensional in nature, all of which cause a significant departure from the ideal model.

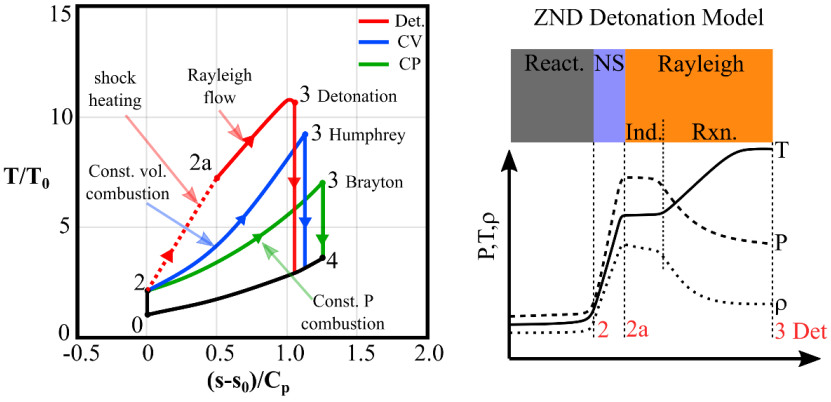

Figure 1.1: (a) Shows the cycle analysis for a detonation cycle, constant volume combustion cycle (Humphrey), and constant pressure combustion cycle (Brayton). (b) The ZND detonation structure.

Because of these non-ideal detonation conditions and the impact on RDC performance, several researchers in the past have studied in detail the development of the structure of the detonation waves in RDCs. For annular RDCs, the commonly used design is axial fuel injection and radial oxidizer injection [5,11–14], and the alternate design comprises axial oxidizer injection and radial fuel injection [6,15–17]. There are considerable losses in turning the bulk flow direction from radial to axial; however, the complexity in obtaining optical access is minimal.

Understanding the fundamental structure of the detonation wave is important for characterizing the global behavior of the RDC. The coupled interactions of the geometry and the flow physics have important implications on the structure of detonation wave, which in turn affects the performance of these systems. Hence, to gain a richer understanding of detonation wave dynamics, high-speed optical measurements are becoming more important. A commonly used optical analogue of the RDC is a linear detonation channel with optical access [18–20]. These channels have allowed the study of coupled detonation-plenum dynamics and injection recovery after wave interaction. However, these single-shot experiments are unable to capture cyclic interactions of the detonation exhaust products within an annular RDC [20–23]. Additionally, detonation physics involving the ignition and consumption of reactants and the structure of detonation interaction with curved surfaces are different in cylindrical RDCs in comparison to their linear analogues [24–27].

A hybrid approach is an obround RDC with two semicircular channels connected with two straight channels [17,28]. However, the transition from straight to curved geometry in this design causes more complex flow interactions in the transition from curved to straight walls that are not fully understood and may not be representative of annular RDCs. Hence, optically accessible annular test sections with a quartz outer-body are becoming more prevalent for studying RDCs [11,16,29]. These test sections provide the most relevant conditions for studying detonation physics in engine-representative environments. This approach is used for the design and evaluation of the RDC described in the current work, with custom design considerations to allow complete optical access for optical diagnostics from the inlet plenum to the exhaust.

1.1 Research Goals

This primary goal of this dissertation is to deploy advanced state-of-the-art laser diagnostics with unprecedented spatio-temporal resolution in detonation environments to address open questions in the current literature. These goals are summarized below:

- Understand the 3-D structure of detonation waves in non-premixed RDCs through spatio-temporally resolved MHz-rate broadband and OH* chemiluminescence imaging. This study aims to address the effects of mixture fill and stratification on the wave's steady state (limit cycle) behavior for non-premixed RDCs.

- Investigate the effects of curved surfaces on the detonation propagation behavior and provide insights into secondary combustion mechanisms including secondary waves, deflagrative burning, and shock-induced detonation.
- Study the cellular propagation behavior in non-premixed RDCs and investigate their departure from traditional soot foil measurements performed in premixed systems.
- Study the influence of channel confinement, recirculation zones, and trapped-hot gas zones on detonation propagation behavior.
- Provide quantitative measurements on the exhaust plume dynamic temperatures for downstream turbomachinery component integration.

1.2 Experimental Approach

In this work a novel optically accessible RDC was designed and constructed for deploying the advanced laser-based diagnostics to understand the detonation wave propagation mechanisms and structure. The details of the test-stand, and diagnostics that were used throughout this thesis are described in this section.

The RDC has an axial air injection and radial hydrogen injection scheme. This injection zone is followed by a backward facing step or a ramp that opens the channel to a 10.7 mm annular gap. This design has optical access from the air-plenum through the exit of the combustor to study the interaction of detonation wave with the injection manifold. MHz rate high speed imaging of broadband chemiluminescence, MHz rate OH-PLIF and kHz rate CARS thermometry are performed to obtain time resolved dynamics of the detonation wave. In addition to the experiment, a 3D unsteady Reynolds Averaged Navier-Stokes (URANS) simulation is run for this RDC geometry with a stoichiometric premixed hydrogen-air using a 1-step reaction model. Results from these simulations provide an understanding of the flow features developed in RDCs of similar injection configuration.

1.2.1 Test article and Test stand description

A cross section of the flow path with a metal and optical outer body is shown in Figure 1.2 (a) and (b) respectively. The outer diameter of the test section is 135 mm and the length of the combustion chamber section downstream of the backward-facing step (BFS) is 90mm. The

combustor annular gap is 10.7 mm, which is comparable to other studies done for this class of RDC [24,26,30]. Air is delivered from a plenum and is choked through a through a converging diverging section at a throat gap of 1.45 mm. The diverging section has an expansion angle of 10 degrees. From the throat location, the channel is expanded at a constant rate until reaching an A/A* = 1.16 where hydrogen is injected through individual holes in a jet in cross flow arrangement. A 10 mm deep plenum pocket feeds 100 milled slots of diameter 0.4 mm and depth 0.6 mm formed between the copper fuel injection plate (red) and the air-throat contraction body (green) as shown in Figure 1.2. Following this flat section where fuel is injected, expansion is continued until an A/A* = 1.8 is achieved and the flow is subjected to a backward facing step leading into the combustor annular gap of 10.7 mm. Downstream of the combustor section, the geometry is expanded further from A/A* = 7 to A/A* = 10.9 to transition flow through a supersonic turbine. Additional details of the turbine, which are beyond the scope of this study, are described in the previous work [16]. An instrumented outer body is constructed from a 15 mm thick stainless-steel (SS-316) cylindrical section, with instrumentation ports for measuring mean attenuated pressure and surface temperatures.

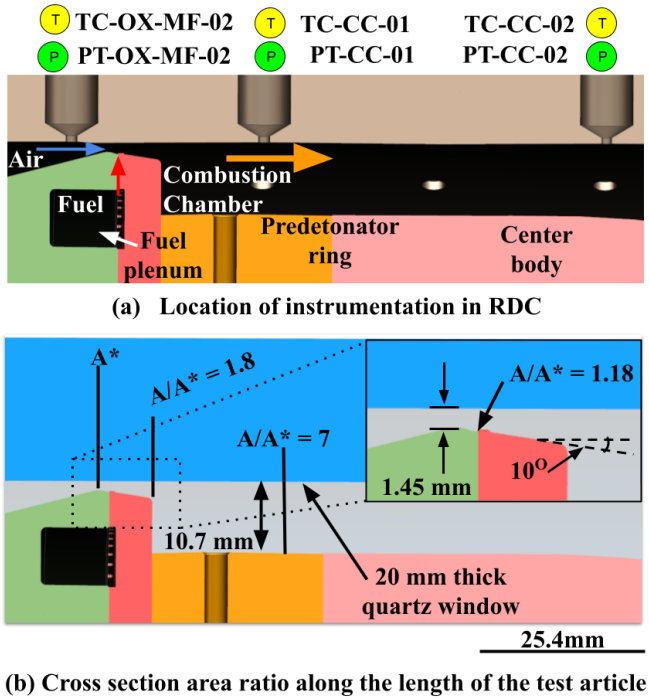

(a) Location of instrumentation in RDC

(b) Cross section area ratio along the length of the test article

Figure 1.2: Schematic of the two configurations of RDC with an instrumented outer body and a quartz outer body.

The instrumented outer-body can be swapped with a quartz cylinder for visualizing the propagation of detonations in the combustion chamber. The optical access of the combustor extends from the air-plenum contraction to the exit plane of the combustor. Downstream of the BFS, a 6 mm threaded port delivers a detonation charge to initiate the detonations in the RDC, as shown in Figure 1.2 The entire RDC has a 50 mm radial clearance through the centerline axis for delivering the ignition charge through a 1/8" tube. A picture of the RDC in operation is shown in Figure 1.3.

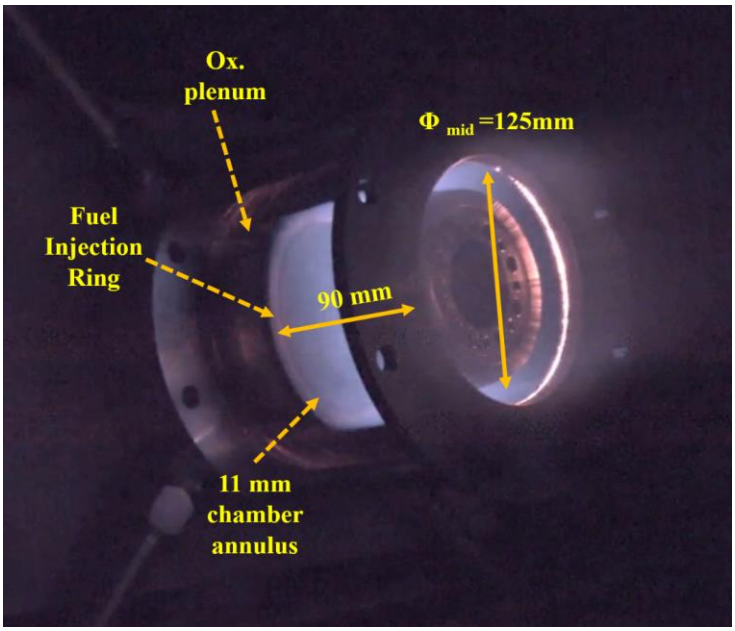

Figure 1.3: Picture of the optically accessible RDC during a test run. 4 x 1" tubes deliver air radially inward into the air plenum. Fuel is injected from 100 holes at the interface of the copper injection ring and the stainless-steel contraction.

By monitoring pressure and temperature upstream of ASME MFC-7M (Flowmaxx Engineering) profile critical venturis [31], flow metering is performed on all fluid supply circuits. Air is delivered radially into the oxidizer plenum through 4 equally spaced 1" diameter supply lines. Fuel is supplied to a manifold block which redistributes the flow into 4 x ¼" lines that supply the fuel manifold at four locations. Two run valves are close coupled to the experiment for precise time-controlled operation of the fuel and purge flows (< 30 ms accuracy). A stainless steel (SS-316) predetonator block is fed with solenoid valve-controlled lines of hydrogen and oxygen. The hydrogen and oxygen lines have respective check valves close coupled to the predetonator block.

The spark gap of an aviation standard sparkplug (Auburn SI-140) is exposed to a small volume, in the predetonator block, fed by the hydrogen and oxygen lines. On ignition of the propellants in the predetonator block by the spark plug, the exhaust is carried out by an 1/8" SS tube and is delivered to the predetonator ring in the RDC as shown Figure 1.2.

Data acquisition and control is performed using a NI DAQ sampling at 2 kHz. Pressure measurements are done using a GE UNIK 5000 (+/- 0.1% FS) transducer which is located at a 10 cm standoff from static pressure port. Grounded K-type thermocouples are used for measuring the temperature along the surface of the inner diameter of the RDC.

1.2.2 Diagnostics

For both the instrumented outer-body experiments and quartz-outer body experiments, a Photron SA-Z camera with a 300 mm visible lens is used. This camera is focused on the combustion chamber for exhaust plume visualization of detonations along the longitudinal axis by means of a silver mirror mounted 12 feet away from RDC.

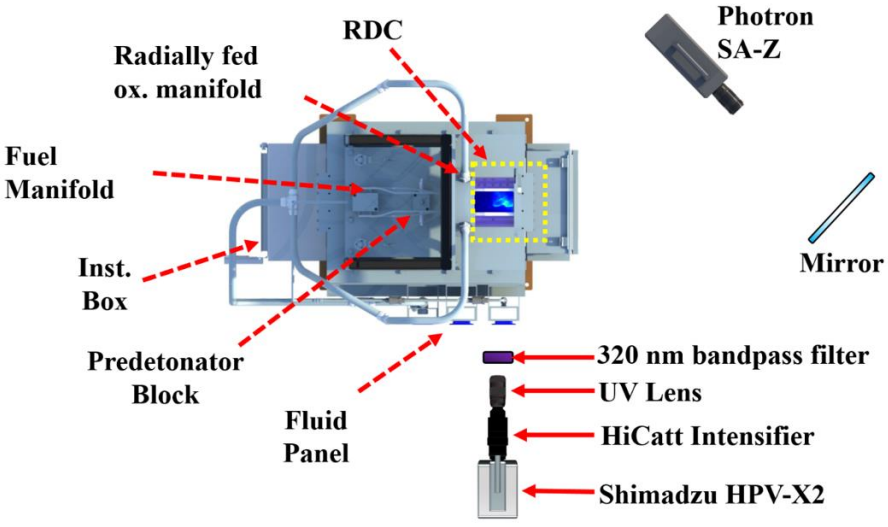

Figure 1.4: Schematic location of test-stand and optical diagnostic equipment with salient features marked. Tests are typically conducted with a 3-camera setup and the quartz outer-body, with each camera running at speeds from 100 kHz up to 1 MHz. In the case of OH*

This view determines the number of detonation waves, the speed of the detonation wave and the dynamics during the startup transient and steady state operation. The SA-Z camera exposure is set to 8.3 µs while the repetition rate is set to 100 kHz. In tests conducted with the quartz outer-body a Shimadzu HPV-X2 camera coupled with an image intensifier, Lambert Instruments HiCatt 25 is used. A 105 mm UV lens is used in tandem with the intensifier and camera configuration. The intensifier gates the chemiluminescence signal to short exposures (between 100 and 500 ns) while increasing the signal count. These short exposures provide instantaneous image of the flame front with minimal displacement of the detonation during the exposure of the image. Hydrogen-air flames have broadband chemiluminescence ranging from 250 nm to 4 µm [32]. The image intensifier has a quantum efficiency cut-off in the IR range above 850 nm. Hence when no spectral filters are used the image intensifier captures emissions from 250 – 900 nm emanating from hydrogen-air combustion. An optional 320 +/- 40 nm band pass filter (Semrock BrightLine FF02-320/40-50) is used to spectrally separate OH* chemiluminescence from broadband flame emission. The Shimadzu camera's memory limits the capture of a maximum of 256 frames at any repetition rate. This allows for a total capture time of 512 µs for 500 kHz repetition rate and 256 µs at 1 MHz Thus, images captured from the Shimadzu were during steady state operation of the RDC, typically at 500 ms after the initiation of ignition. The RDC reaches steady state at 100 ms after ignition.

1.2.3 Timing and test sequence

The test sequence involves a series of sequential control of valves and pressure regulators. The timing diagram of different operations performed in the RDC is shown Figure 1.5. Prior to the start of the test, the airflow is set to the appropriate mass flow rate. Nitrogen is purged through the fuel circuit to keep the fuel injector system free of contaminants. At the start of the test t = 0 s, the fuel run valve is commanded to remain closed while the nitrogen purge valve and predetonator hydrogen and oxygen run valves open. At 100 ms, the fuel run valve is opened, and nitrogen purge run valve closed simultaneously. This establishes hydrogen flow through the fuel circuit, which primes the test section for testing. At 150 ms the sparkplug in the predetonator block is commanded to start firing. This marks the start of the test. Simultaneously, Phantom v2012 cameras is commanded to start recording at 100 kHz with a TTL pulse. The spark-plug fires for 100 ms before it is turned off along with the predetonator fuel and oxidizer valves. At 500 ms after the initiation

of spark, the Shimadzu camera is triggered to start capturing the 250 – 500 µs evolution of detonations at steady state. At 1.1 seconds after the initiation of spark, the fuel run valve is closed, and the purge valve is opened. This marks the end of the test. Finally, the air flow and nitrogen purge are stopped after sufficiently cooling the test section, typically 3 -5 seconds after the end of the test. No additional abort thresholds are established since the test is intentionally aborted at the end of the sequence.

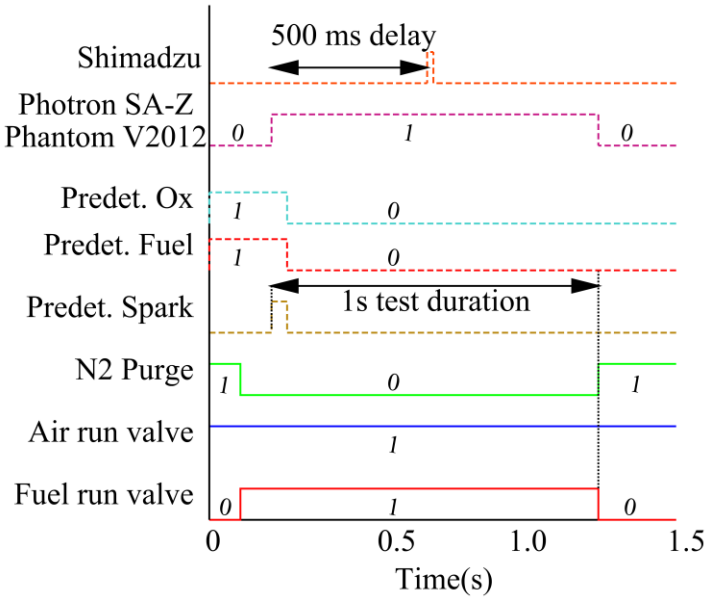

Figure 1.5: Timing diagram for RDC operation.

1.3 Thesis document overview

The work presented in this document is a culmination of the development of an optically accessible non-premixed H_2-air RDC test platform with the implementation of high repetition rate diagnostics that represent the current state of the art. This work provides the first measurements of spatio-temporally resolved ultra-high-speed laser diagnostics at repetition rates of up to 1 MHz in these highspeed aerothermal flows. The high repetition laser-diagnostics, combined with the URANS simulations effort in collaboration with Profs. James Braun and Guillermo Paniagua, provides key insights into the detonation wave behavior in non-premixed RDC. Sections 2, 3 and 7 appear in the literature, Section 4 is under review and Section 5 and 6 are being compiled for publication in the near future.

A short description of the diagnostic implemented, and the scientific contribution of each section is given below:

- **Section 2**: MHz-rate OH* chemiluminescence measurements are performed in a non-premixed hydrogen-air RDC. The scope of this section is to understand the three-dimensional detonation wave structure by studying the radial-axial and radial azimuthal structures of the detonation wave. Additionally, mass-flux variations were introduced to study the wave response to increasing axial momentum.
- **Section 3**: OH-Planar Laser Induced Fluorescence (OH-PLIF) at repetition rates of up to 2 MHz was performed for the first time and implemented in the radial axial plane of the RDC by exciting the $Q_1(9)$ transition of hydroxyl radical. These measurements spatio-temporally resolve the detonation wave passing through the radial axial plane, providing time resolved 3D structure of rotating detonations.
- **Section 4**: MHz rate broadband chemiluminescence, simultaneous MHz rate OH* chemiluminescence/OH PLIF, and results from URANS simulations were explored to understand the role of mixture stratification in detonation wave structure. These results provide the first detailed experimental evidence of a freely propagating and shock-induced detonation in non-premixed RDCs.
- **Section 5**: MHz rate broadband chemiluminescence was used to understand the cellular propagation of hydrogen-air in a stratified reactant flow. Such cellular structures are not typically apparent within highly non-uniform detonation waves within non-premixed RDCs, and this work provides definitive evidence of their occurrence.
- **Section 6:** MHz rate OH* chemiluminescence and OH PLIF are used to understand the effect of confinement and the role of the product recirculation due to a backward facing step at the inlet of non-premixed RDCs. These results indicate that the BFS design has a single steep fronted detonation followed by an azimuthally trailing shock induced detonation present only in the injection nearfield. While in the case of a ramp design, the elimination of the BFS lateral relief leads to multiple detonation wave surfaces spread azimuthally behind a relatively weak detonation wave. This lateral relief also helped the detonation wave speed reach higher values in the BFS design as opposed to the ramp design.
- **Section 7**: Hybrid fs/ps RCARS thermometry was carried out at 1 kHz repetition rate in the exhaust of the RDC for the first time. Extensive theoretical analysis was performed to

understand the uncertainty limits of this quantitative diagnostic in such highly dynamic environment. Computed combustor pattern factor of 0.20 from the experiments closely matched the pattern factor estimation from URANS simulations of 0.19, illustrating the ability of such measurements to validate numerical predictions.

Sections 4 and 5 have manuscripts under peer-review for publication in Combustion and Flame as full-length article and brief-communications, respectively. **Section 6** is under compilation for submission to Combustion and Flame for peer review.

The sections that appear in the literature are:

Section 2: **Athmanathan, V.,** Braun, J., Ayers, Z., Fisher, J., Fugger, C., Roy, S., Paniagua, G., and Meyer, T. 2020. Detonation structure evolution in an optically accessible non-premixed H2-air RDC using MHz rate imaging. In *AIAA SciTech 2020 Forum*. American Institute of Aeronautics and Astronautics.

Section 3: Hsu, P., Slipchenko, M., Jiang, N., Fugger, C., Webb, A., **Athmanathan, V.,** Meyer, T., and Roy, S. 2020. Megahertz-rate OH planar laser-induced fluorescence imaging in a rotating detonation combustor. *Opt. Lett., 45*(20).

Section 7: Athmanathan, V., Rahman, K., Lauriola, D., Braun, J., Paniagua, G., Slipchenko, M., Roy, S., and Meyer, T. 2021. Femtosecond/picosecond rotational coherent anti-Stokes Raman scattering thermometry in the exhaust of a rotating detonation combustor. *Combust. Flame, 231*, p.111504.

2. DETONATION STRUCTURE EVOLUTION IN AN OPTICALLY ACCESSIBLE NON-PREMIXED H_2-AIR RDC USING MHZ RATE IMAGING

Investigations of the structure of non-premixed rotating detonation waves and the influence of the fuel-air injection system are presented in this work. A hydrogen-air rotating detonation combustor (RDC) with optical access extending from the oxidizer injection plenum to the exit plane is used. Via intensified high-speed cameras, the structure of propagating detonation waves is resolved at frame rates up to 1 MHz. At high mass flux, weaker detonation zones are observed via broadband chemiluminescence near the injection plane and stronger zones further downstream. The detonation wave longitudinally couples with the injection plane and produces minimal observable combustion product back-flow through the injectors. The axial variations in the detonation strength are attributed to fuel stratification, mixing, and local variation in thermodynamic properties of the mixture. The longitudinal coupling is attributed to periodic variations of the height of the detonation wave. These phenomena are investigated for varying mass flux, which affects the detonation wave structure and coupling with the injection plenum. Unsteady Reynolds-Averaged Navier-Stokes simulations are used to complement the experimental observations and provide insight into the fuel-air mixing and product flows for the same combustor geometry and conditions. These investigations are part of ongoing efforts to understand the effects of combustor design and operating parameters on combustion efficiency and RDC operation.

2.1 Introduction

Rotating detonation combustors, in which a rotating shock is continuously burning the reactants, can theoretically lead to increased gas turbine cycle efficiencies from operating in a valveless constant volume combustion [3,25,33,34]. Over the past decade, substantial research has been performed to understand the flow physics within rotating detonation combustors over a wide range of operating conditions for premixed as well as non-premixed systems, both numerically [25,26,35–38] and experimentally [4,5,11,16]. Achieving pressure-gain combustion, however, remains a challenge due to mixing inefficiency and pressure losses across the injector, necessitating experimental investigation of these detonation structures in non-premixed RDCs. To resolve kHz-rate detonation cycles, high frequency pressure sensors are typically used for

experimental studies [21,39,40]. Alternatively, to optically characterize refill height, shock structure, and parasitic combustion, linear or obround geometries with optical access have been used [19,39]. However, to understand the detonation structures more fully in these systems, an optical analog is preferred over linear and obround geometries since circular geometries preserve the physics of detonation interactions with curved surfaces.

In this paper, an optically accessible RDC was built to investigate the dynamics of the detonation wave with the injection system. This RDC's unique optical access to the oxidizer plenum provides real-time information on injection plenum coupling behavior and the associated effects on RDC performance. High frequency chemiluminescence imaging was performed to resolve the instantaneous flow features and describe the structure of the detonation waves, along with complementary Unsteady Reynolds-Averaged Navier-Stokes (URANS) simulations.

2.2 Experimental Setup

2.2.1 Test Article Description

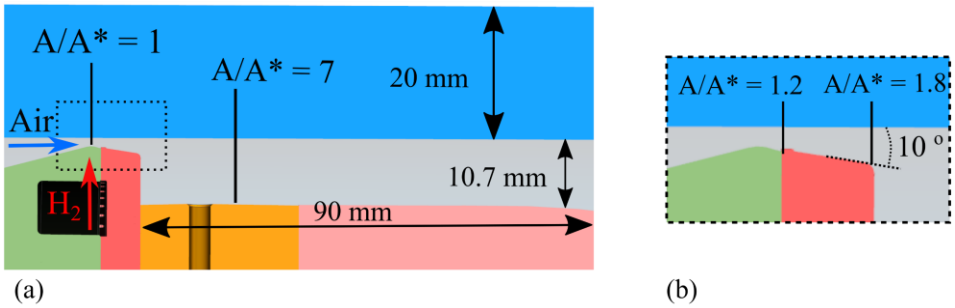

Figure 2.1: (a) Schematic of the flow path of propellants in the non-premixed hydrogen air RDC. Area ratios at salient locations are marked. (b) Close-up view from the boxed region in (a).

A schematic of the injector and combustion chamber flow-path is presented in Figure 2.1. This RDC has axial air injection and radial hydrogen injection. The air plenum contracts to a throat and the air flow is expanded at a 10° expansion angle into the combustion chamber. At an area ratio (A/A*) of 1.2, 100 individual slots inject hydrogen in a jet-in-crossflow fashion. The non-premixed reactants are expanded to an area ratio of 1.8 and a sudden expansion through a backward facing step (BFS) increases the area ratio to 7. Downstream of the BFS, there is a 6 mm hole that delivers a predetonation charge radially outward for ignition. The outer body of the RDC is constructed from a 20 mm thick fused quartz cylinder to for optical access. The optical outer body

can be replaced by an instrumented outer body constructed from stainless steel to monitor RDC operation. The mean annulus diameter is 125 mm, length from the BFS is 90 mm and the channel gap is 10.7 mm, similar to other computational and experimental RDC investigations [11,24,26].

With the instrumented outer body installed, pressure data are collected at 2 kHz using GE UNIK 5000 pressure transducers at multiple locations in the combustion chamber as well as in the fuel and oxidizer manifolds. Slow response thermocouples are mounted at multiple locations to track the heat load during the 1 second operation. Air flow and hydrogen flow are metered using sonic venturis. The test sequence is automated using the National Instruments LabVIEW VI. The test duration is set to 1 second for all test cases. The predetonator is fed with hydrogen and oxygen and is initiated by a sparkplug. The RDC reaches steady state operation 40 ms after chamber ignition and diagnostic data collection begins at 100 ms after ignition. Additional information on the RDC geometry and operation are presented in a previous work [16].

2.2.2 Diagnostics

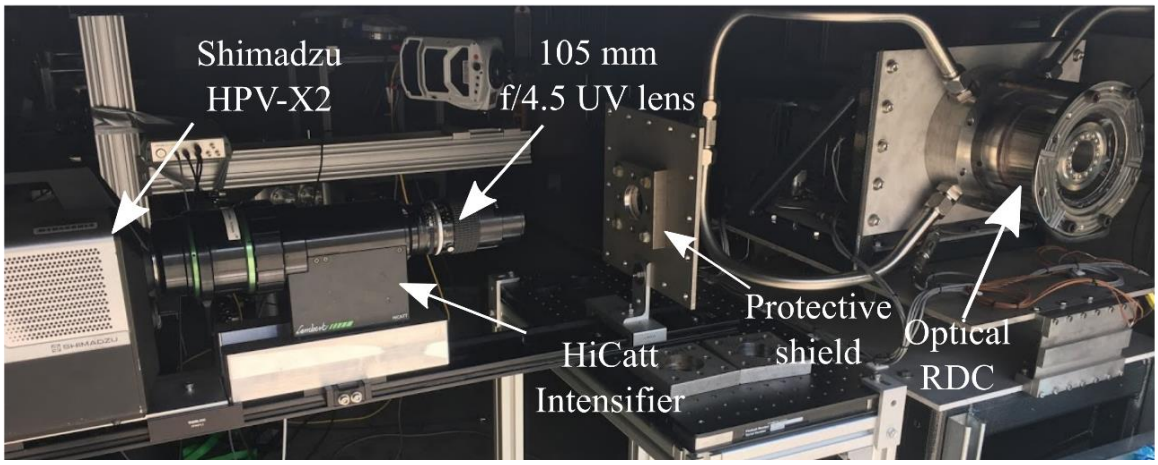

Figure 2.2: Diagnostics Setup for capturing kHz and MHz rate images.

To capture the detonation evolution, CMOS cameras and two-stage intensifier are used to capture broadband chemiluminescence in the RDC with a 105 mm f/4.5 UV lens. For repetition rates up to 100 kHz, a Phantom v2012 is coupled to a HiCatt intensifier. For higher repetition rates, the HiCatt Intensifier is coupled to the Shimadzu HPV-X2 camera, as shown in Figure 2.2Figure 2.4. The Shimadzu camera can capture images at repetition rates up to 10 MHz at full frame (250 x 400 pixels), while the intensifier is limited to 1 MHz. A protective steel barrier is used to protect

the camera system in case of quartz failure. At all test conditions, the intensifier gate is set to 200 ns in order to prevent blurring effects from detonation wave motion during the exposure. During this exposure it is estimated that the detonation wave would have moved less than 0.5 mm.

2.2.3 Test conditions

In this work, the RDC is operated at a global equivalence ratio of 1.0 with varying mass fluxes. The oxidizer mass flux of the RDC is varied from 350 kg/m^2/s to 750 kg/m^2/s which corresponds to an oxidizer flow rate of ~ 0.22 kg/s and 0.44 kg/s, respectively. The baseline condition is established at G=750 kg/m^2/s and a global equivalence ratio of 1.0.

2.3 Results

2.3.1 Mixing inhomogeneity in reactant flow field

To understand the qualitative mixing characteristics of the injection system, radial contour slices of the local equivalence ratio are presented in. These slices are located 12^o and 13.8^o azimuthally ahead of the detonation wave centered on a fuel injector site (Figure 3a) and in-between two fuel injector sites (Figure 3b), respectively. A contour plot of Mach number is shown in Figure 3c centered on the fuel injector site.

The reactant flow field can be qualitatively divided into two zones (Figure 3a). Zone I, located from the BFS to ~25 mm axially downstream, contains very fast-moving fluid that is mostly unmixed, and fills a radial fill of 4–5 mm from the outer diameter of the annulus. Zone II, located from ~25 mm to ~50 mm downstream of the BFS, has slower and relatively well-mixed reactants that fill the entire 10.7 mm radial depth of the annulus. The fast-expanding jet in Zone 1 interacts with the shear layer from the previous product gas in the recirculation zone formed behind the BFS (Figure 3a). Zone II is characterized by reactants at lower Mach numbers. This is the result of the transient refill process and recovery of the injectors directly after the passing of the detonation wave. The high static pressure after the detonation wave instantaneously induces low injection velocity for the fuel and the air injectors. The static pressure in the combustor slowly decreases due to product gas expansion through the exit and the annulus, allowing injector recovery. This periodic unsteady interaction leads to cycle-to-cycle variations in the reactant refill process and affects to the propagation of the detonation wave, as will be discussed further below.

The lower velocity in Zone II also provides a longer axial residence time for mixing the reactants, resulting in local equivalence ratios of ~0.8 – 2.0. The small region of fuel-rich equivalence ratio observed in Zone II is potentially due to variation in the recovery time of the fuel and air streams after the passage of the detonation wave. The implications of this stratified fuel-air mixture on the structure of the detonation wave are discussed below.

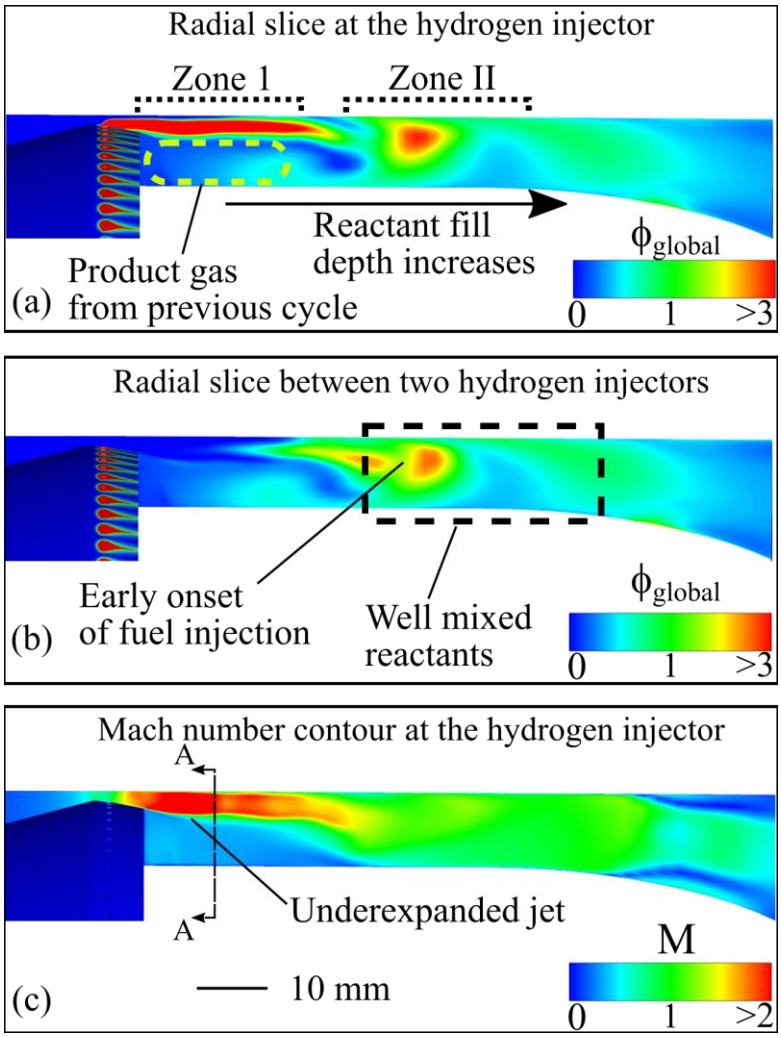

Figure 2.3: Radial-axial slice of the reactant jet ~10 ^{o} azimuthally ahead of the detonation wave. (a) Local equivalence ratio centered on a fuel injector and (b) local equivalence ratio in-between two injectors. (c) Mach number contour centered on a fuel injector

2.3.2 Axial variations in detonation structure:

For non-premixed systems, the fuel and air streams entering the RDC from the injection system require a certain mixing length downstream of the backwards facing step (BFS) to form a well-mixed flow. A sketch of the hydrogen mass fraction for the baseline condition (G = 750 kg/m^2/s, ϕ = 1.0) is depicted in (a) of a preliminary three-dimensional URANS simulation in which the fuel slots and air plenum are separately modeled. The URANS simulation images present depict the temperature and concentration present at the outer wall of the RDC Region A encompasses the mixing region and we observe the presence of fuel stratification in the tangential direction, with alternating zones of fuel-rich and fuel-lean regions which allow the detonation wave to propagate. This fuel stratification (and subsequently equivalence ratio stratification) is caused by the discrete fuel injectors. Fuel stratification is minimized further axially downstream, as the fuel and air mix (region B). Thus, a monotonic increase in mixing takes place in the axial direction. The mixing length increases with increasing mass flux. In addition, the high-speed underexpanded reactant jet entering the system has a lower static pressure near the BFS (region A). Axially downstream, the shear layer interactions slow the reactant momentum, leading to an increased static pressure zone (region B).

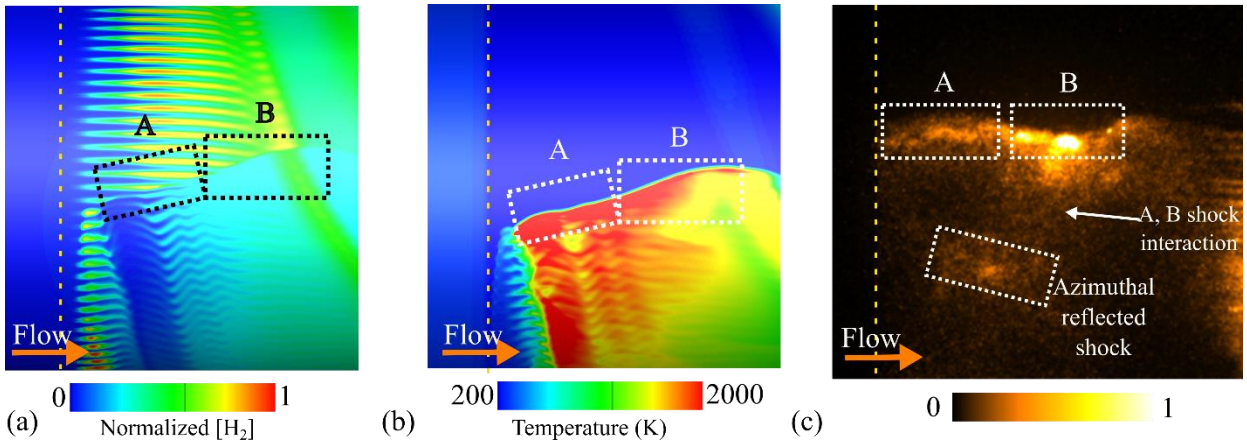

Figure 2.4 Preliminary URANS simulation results showing normalized hydrogen mass fraction (a) and temperature (b). Instantaneous image of detonation structure formed shows axial variations in intensity of the detonations wave.

Thus, two different zones of reactants are present ahead of the detonation wave. Region A contains low static pressure reactants which are relatively unmixed, while region B has high static pressure and relatively well mixed reactants. This leads to a detonation wave formation with an axial

variation in detonation strength, as shown in Figure 2.4 (c). Region A in Figure 2.4 (c) shows a relatively weaker detonation wave marked by low luminosity. However, region B is characterized by a stronger detonation wave, marked by high luminosity as opposed to region A.

This axial variation in detonation strength leads to complex combustion product gas interaction. The shear layer between the product gas of the strong zone and weak zone, which have higher and lower static pressure respectively, leads to an oblique shock system formation at this interface as marked in Figure 2.4 (c). These mixing and aerodynamic features are exacerbated with increasing mass flux. It is noted however, that the average detonation wave velocity is the same for Region A and B. This suggests a strong coupling between the stronger and weaker zones of the detonation wave despite the variations in local equivalence ratio and static pressure which influence the wave propagation speed.

Another key observation is the chemiluminescence in the azimuthal reflected shock behind region A. For annular gaps over 10 mm, an azimuthal shock system is formed behind the detonation wave due to the curvature of the channel gap, as predicted by various numerical simulations [24,26,30]. Evidence of this azimuthal shock reflection is absent in region B but clearly observed by marked chemiluminescence in region A as shown in Figure 2.4 (c). It is suggested that due to the un-mixedness in region A, pockets of unburned fuel and air pass the detonation wave. These pockets of unburned vitiated fuel and air are compressed in the azimuthal shock system which causes an increase in static pressure and temperature and provide a zone for shock induced supersonic combustion. In region B, however, due to the well mixed reactants present ahead of the detonation wave, the detonation wave consumes all the available reactants. Hence there is no chemiluminescence present in the azimuthal shock system trailing region B. Thus, a combination of isochoric heat release from freely propagating detonation and ‘shock-induced’ detonation exists for this geometry. And the quantification of these phenomena is vital to understand all underlying loss mechanisms and eventual pressure gain of the system.

2.3.3 Radial variations in detonation structure

The head on view of the detonation wave also shows a variation in chemiluminescence the radial direction in region A and B. Figure 2.5(a) plots the phase averaged chemiluminescence obtained when the detonation wave passes through the head on section view providing information on radial structure of the detonation wave (baseline condition). Figure 2.5(b) illustrates the distribution of

hydrogen concentration from a premixed URANS simulation system at the baseline condition. Near the BFS, in region A, the reactant fill depth is on the order of 4-6 mm, while in region B, the reactant depth fills the entire channel gap of 10.7 mm.

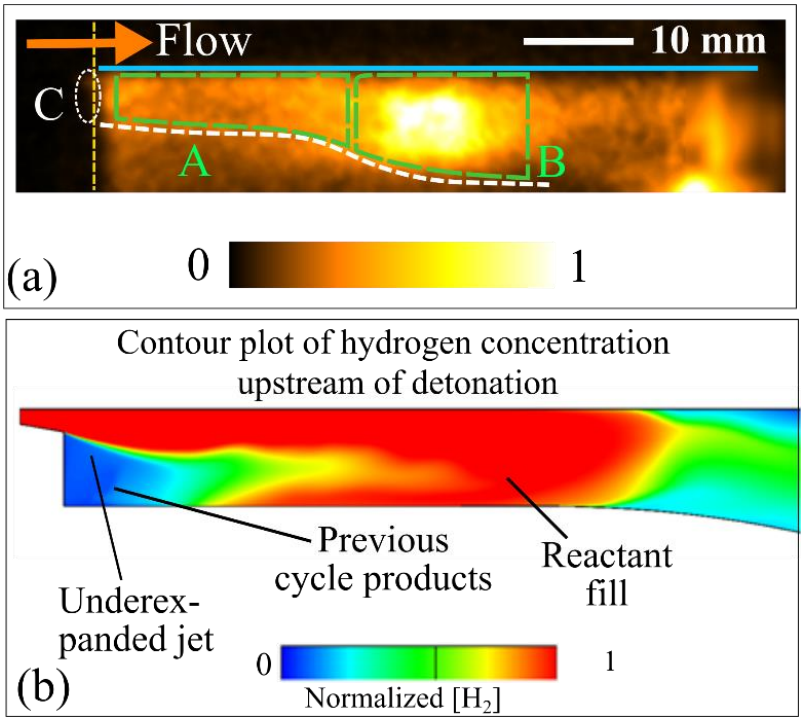

Figure 2.5: Radial flow structure formed in non-premixed systems.

Thus, the detonation wave in region A has relatively lower three-dimensional effects as opposed to the wave in region B. The products of region A can expand azimuthally, as well as axially. Chemiluminescence evidence of combustion product back-flow is faint and minimal, as observed in the zone marked C in Figure 2.5 (a) (yellow line locating the BFS). Hence, for non-premixed RDCs operating at high mass flux, there is a relatively low combustion product backflow compared to the lower mass-flux case. However, lower temperature products (< 1500 K) that do not produce any chemiluminescence can still stop injection of reactants and mix with the fresh incoming reactants. Further investigation is required to quantify this coupling behavior of the injection plenum and combustion product backflow.

2.3.4 Mass flux variation effects

Three different mass fluxes were investigated to study the interaction of the detonation wave with the injection system. The global equivalence ratio was maintained at $\phi = 1.0$ for all the three cases. Phase averaged images from 100 kHz imaging of intensified broadband chemiluminescence for mass flux of G = 350 kg/m^2/s, 450 kg/m^2/s and 750 kg/m^2/s are presented in Figure 2.6Figure 2.6. The images used for phase averaging were required to have at least 95 % of cross correlation overlap with each other. The intensifier gate for each image was set to 200 ns to minimize blurring due to wave motion during exposure period. The BFS is marked with a dashed line. Two notable and distinguishing features are observed.

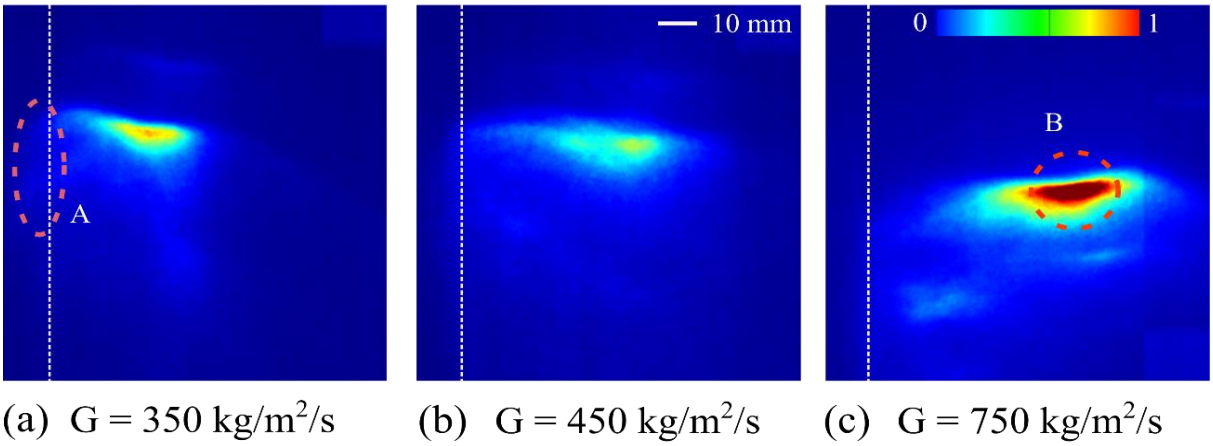

Figure 2.6: Phase averaged chemiluminescence images of detonation structure for three different mass fluxes at global equivalence ratio of 1.

The first feature is the backflow upstream of the BFS. For the low mass flux case, hot product back flow is observed (label A, Figure 2.6(a)). At the intermediate mass flux case, there is visible chemiluminescence upstream of the BFS while the high mass flux case has the lowest chemiluminescence observed suggesting low hot product back flow. At lower mass fluxes, lower injection pressure and early onset of mixing owing to low momentum injection causes the detonation wave to be stationed close to the BFS. This case also exhibits a relatively invariant detonation field in the axial direction. In contrast, the detonation wave in the high mass flux case displays axial variations in detonation strength due to fuel stratification and high-momentum axial flow.

The second notable feature is the azimuthal and transverse variation in the detonation structure. In Figure 2.6 (c), a widening of the transverse feature is clearly observed. The brightest portion of the detonation wave exhibits transverse motion which manifests as a large lobe (label B, Figure 2.6) in the phase averaged image. This variation is attributed to the injection coupling with the detonation wave. This behavior is absent at lower mass fluxes due to shorter response time of the product gas from the detonation front interacting with the injection system. Longitudinal coupling modes have been proposed as explanations for phenomena observed using pressure transducers in previous studies [15]. This mode coupling plays an important role in injection manifold dynamics and consequentially affect the stability and efficiency of detonation waves.

2.3.5 Detonation structure evolution using MHz rate imaging.

The propagation of detonation wave at the baseline condition using 1 MHz rate imaging is shown in Figure 2.7. The time between each shot is 1 μs while the exposure of each frame is 100 ns, much shorter than the previous cases. The FOV is 83 mm x 83 mm and image transformation was not performed to 'unwrap' the cylinder. At the start of the image sequence, we can see a tall detonation structure with a bright zone near the well mixed zone. As the detonation wave propagates through the channel, relevant structures appear, as described in the previous section, with a weak detonation zone near the BFS and a strong detonation zone downstream. Between t = 15μs and t= 24 μs, we observe the stronger detonation zone propagate upstream towards the BFS. This transverse oscillatory behavior is attributed to the variation in refill height between cycles. We also observe the azimuthal shock system (t =26μs), which is located near the BFS due to vitiated burning of unburned reactants in the shock system, as described in section (i). A shock interaction is also observed between the products of strong detonation zone, the azimuthal shock system, and the weak detonation zone (marked at t = 33 μs). At t = 30 μs, the initial injection recovery marked by the absence chemiluminescence near the BFS appears, however, further interactions from the strong detonation zone influence the injection process in a periodic fashion after initial injection recovery. This interaction leads to the variation in refill height which in turn leads to longitudinal oscillation coupling between t = 15 μs and t = 24 μs. Thus, MHz rate imaging provides a detailed understanding of the flow features involved in non-premixed RDC, and the interaction of detonation and injection system.

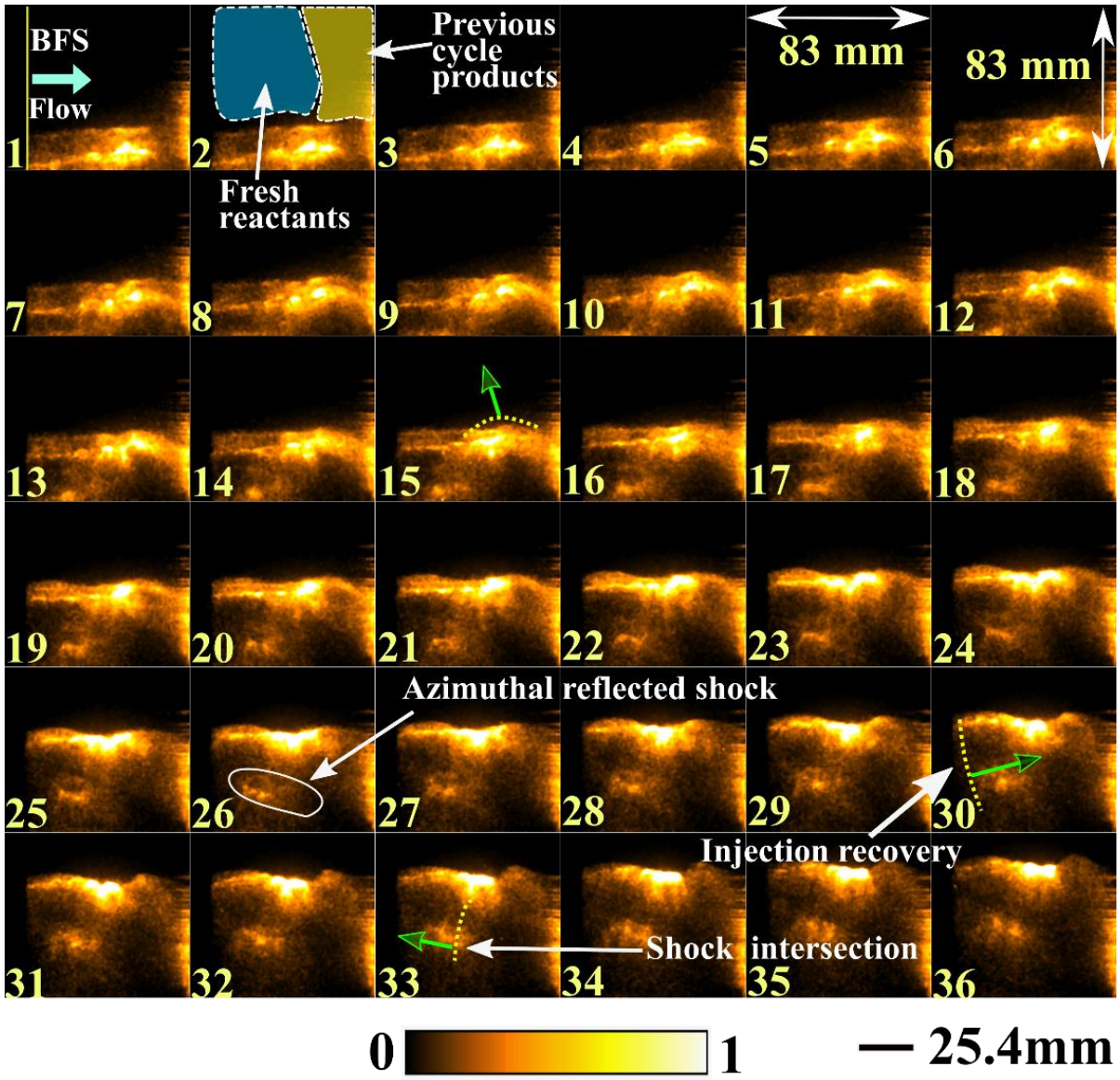

Figure 2.7: MHz rate broadband chemiluminescence images of detonation wave propagation at baseline condition.

2.4 Conclusions

An optically accessible RDC is used to study the structure of detonation wave and their interactions with the injection plenum in non-premixed systems. At high mass fluxes, the non-premixed detonation waves have an axially variant detonation strength which is attributed to (a) fuel stratification and poor mixing near the injection plane and better mixing further downstream, (b) low static pressure near the injection plane caused by high momentum flow and high static pressure

further downstream due to shear layer interactions and (c) a radial fill depth increase with axial length due to sudden expansion from the injection plane to the combustion channel. The aforementioned effects cause a weakly propagating detonation wave near the injection plane with a stronger detonation zone downstream. A first account of visualization of an azimuthal shock system was presented. Chemiluminescence in the shock system was attributed to the vitiated unburned reactants combusting in the shock system. The detonation injection coupling varies dramatically by varying the oxidizer mass flux. Two observations are made (a) Mass flux is inversely proportional to the amount of product back flow into the injection system (ii) Longitudinal mode coupling with the injection is proportional to the oxidizer mass flux in axial flow RDCs. MHz rate imaging provided a global understanding of detonation wave propagation and their interactions with the injection system.

3. MHZ-RATE OH PLANAR LASER-INDUCED FLUORESCENCE IMAGING IN A ROTATING DETONATION COMBUSTOR

MHz-rate hydroxyl radical planar laser-induced fluorescence (OH-PLIF) was demonstrated in a hydrogen/air rotating detonation combustor (RDC) for the first time. A custom injection-seeded optical parametric oscillator (OPO) pumped by the 355-nm output of a high-energy burst-mode laser produced narrowband pulses near 284 nm for OH excitation. The system generated sequences of more than 150 ultraviolet pulses with 400 μJ/pulse at 1 MHz and 150 μJ/pulse at 2 MHz. The order of magnitude improvement in the repetition rate over prior OH PLIF measurements and in the number of pulses over previous MHz burst-mode OPOs enables spatiotemporal analysis of complex detonation combustion dynamics.

3.1 Introduction

Over the last half century, planar laser-induced fluorescence (PLIF) has been widely used for the measurement of flow structure [41], species concentration [42], temperature [43], and velocity [44] in non-reacting and reacting flows. PLIF has several advantages over other flow-structure diagnostic techniques such as Rayleigh scattering and Schlieren imaging, because of its high spatial resolution, the minimum impact of laser scattering from the model surface, and a high fluorescence yield of key combusting species. This enables measurement of minor species that play a critical role in chemical-kinetics mechanisms for combustion and detonation, such as OH, CH, CH2O, NO, CN, H, and O [41]. A typical PLIF experiment requires only a single laser sheet and can be extended to three-dimensional imaging via volume illumination [45]. The addition of PLIF tracer molecules can also be used for mixture-fraction imaging [46] and studies of supersonic and hypersonic boundary layers [47]. Almost all the aforementioned species share a common spectroscopic feature: their spectral transitions from the ground-electronic state to the first few excited states lie in the ultraviolet (UV) wavelength range. This means that an excitation laser tuned to the UV wavelength via dye lasers or optical parametric oscillators (OPOs) is required. Previous state-of-the-art OH PLIF measurements at rates of 50–100 kHz were performed initially using a burst-mode OPO [48,49] and later up to 50 kHz using diode-pump solid state (DPSS) lasers pumping a dye laser [50]. This allowed temporally correlated, spatially resolved temperature

measurements in turbulent subsonic flows with moderate Reynolds (Re) numbers. However, this measurement speed is insufficient for investigating highly turbulent and transient flow dynamics, such as combustion in detonating or hypersonic flows. The rotating detonation engine is an advanced propulsion concept in which detonation waves propagate through premixed or non-premixed reactants in an annulus at typical velocities greater than 1500 m/s. Recent MHz-rate chemiluminescence imaging in a rotating detonation combustor (RDC) revealed highly dynamic flow phenomena that belied a complex non-uniform detonation-wave structure which could not be resolved by the line-of-sight averaged nature of the measurements [51]. The advent of ultrahigh-speed burst-mode laser technology, which can generate approximately 100 times more pulse energy at high repetition rates as compared to continuously pulsed lasers (e.g., DPSS), provides a potential pathway for spatiotemporally resolved measurements of the detonation-wave structure using PLIF at measurement speeds of 100 kHz–1 MHz [46–49]. A solid-state OPO and harmonic frequency conversion can then be used to generate narrowband UV output for excitation of combustion radicals at repetition rates that would otherwise induce photobleaching and thermal degradation in other tunable sources such as dye lasers [52,53] . Prior demonstration of a burst-mode OPO for MHz NO PLIF in a nonreacting boundary layer within a NASA Mach-10 wind tunnel by current authors was limited to a sequence of 10 pulses over a 10 μs measurement window [47]. In addition to lacking the measurement duration to track fast transient combustion events such as detonations and flame instabilities in novel propulsion systems (e.g., typical single RDC cycle ~245 μs), this approach required high levels of NO seeding as a tracer species. Prior to the current work, PLIF imaging of native combustion intermediates, such as the hydroxyl radical (OH), in RDC flow fields has been limited to 10 Hz [54].

This paper describes an order-of-magnitude advancement in the duration of MHz-rate PLIF sequences of more than 150 images using a custom-designed, narrowband tunable burst-mode OPO coupled with an intensified ultrahigh-speed CMOS camera. Per pulse energies are also higher (400 μJ/pulse at 1 MHz and 150 μJ/pulse at 2 MHz) and enable sensitive detection of native OH radicals in highly transient combustion environments. This is demonstrated for measurements in an optically accessible RDC with detonation wave speeds exceeding 1500 m/s.

3.2 Experimental setup

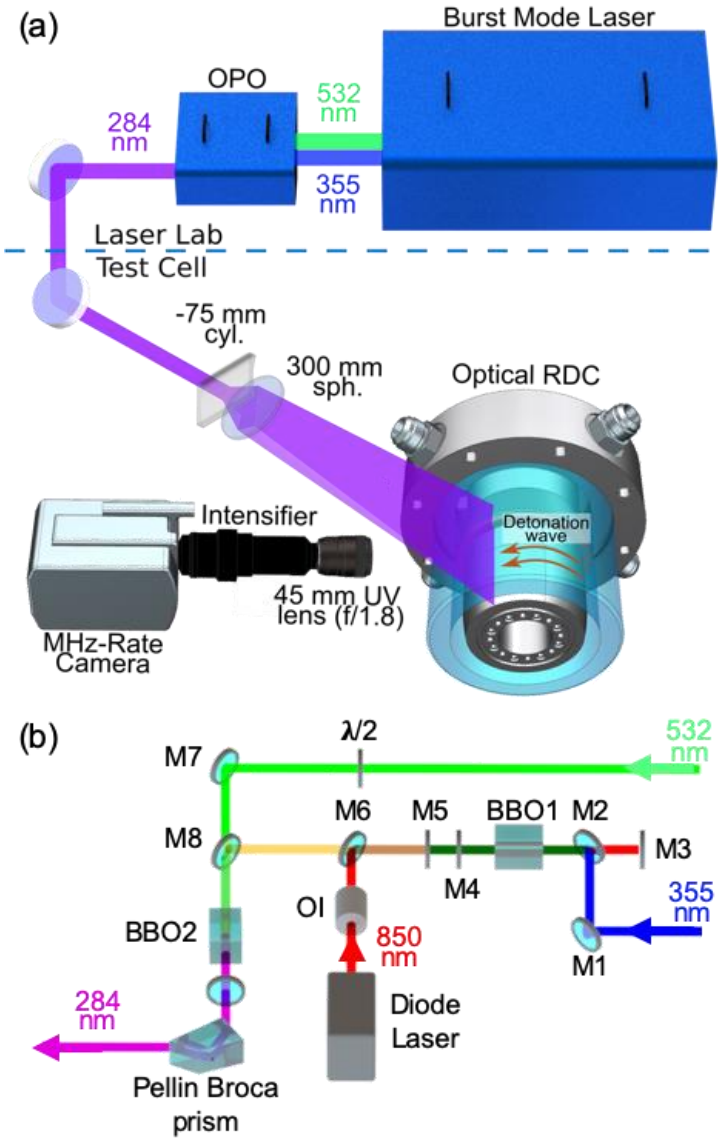

Figure 3.1: (a) Major components of the setup and their arrangement in the laser laboratory and the test cell. OPO - optical parametric oscillator; RDC – rotating detonation combustor. (b) OPO layout. M3 and M4 − OPO cavity mirrors, M2 − OPO pumping mirror, M5 − OPO pump double-pass pump mirror, $\lambda/2$ − half waveplate, BBO1 – OPO BBO crystal 32° cut, BBO2 – BBO mixing crystal 43° cut, OI − optical isolator.

The experimental setup for performing MHz-rate OH-PLIF measurements in the RDC is shown in Figure 3.1, including the burst-mode laser, OPO, high-speed camera, intensifier, and RDC layout in (a), as well as a detailed schematic of the OPO in (b). The fundamental beam from the high-energy MHz-rate burst-mode laser (Spectral Energies, QuasiModo) [55] was frequency tripled to

produce pulses of approximately 40 mJ/pulse and 5 ns at 355 nm with a laser linewidth of less than 300 MHz at this wavelength. The burst-mode laser also generated a second-harmonic 532-nm output of ~20 mJ/pulse for use in sum-frequency mixing (SFM) with the output of the OPO down to 284 nm. The OPO wavelength was tuned to excite the $Q_1(9)$ transition in the (1, 0) band of the OH $A^2\Sigma - X^2\Pi$ system. To increase the efficiency of the OPO conversion process at 1 MHz, the size of the 355-nm pump beam was reduced from 8 mm to 6 mm using a telescope. At 2 MHz, the conversion efficiency and stability were maintained by reducing the pulsewidth to 2.6 ns. The OPO consisted of one Type-I beta-barium-borate (BBO) crystal that was cut at an angle of 32° to the optical axis. The length of the crystal was 12 mm, with an 8×8 mm^2 cross-section. The crystal surface was AR coated to reduce scattering loss at the pump and OPO signal/idler wavelengths. The cavity employed a broadband high reflector and a 20%-reflective output coupler for signal and idler generation in the wavelength ranges of 600–620 nm and 820–870 nm, respectively. Thus, both the signal and idler beams were amplified in the linear cavity. A retroreflector for the pump beam was placed after the output coupler for OPO gain in both the directions of signal and idler propagation.

To increase the OPO output efficiency at low pump energies, the total cavity length was limited to ~4 cm. A narrow-linewidth, single-frequency, external-cavity diode laser (Sacher, Lion) was used to injection seed the cavity through an optical isolator at the idler wavelength of ~850 nm. After the OPO cavity, the output OPO signal beam was sum-frequency mixed with the residual 532-nm beam from the burst-mode laser in a 10-mm-long BBO crystal (θ=43°).

The generated 284-nm beam propagated ~20 m from the laser lab to the optical RDC. The beam was formed into a ~80-mm-long light sheet using a spherical (f = 300 mm) and cylindrical (f = -75 mm) lens pair entering normal to the quartz cylinder and at an angle of 45° with the camera. Because of the curvature of the 0.83” thick quartz window, the object plane was adjusted to be in-line with the camera axis. The PLIF spatial domain enabled tracking of OH upstream of the injection system to near the RDC exit plane. The resultant fluorescence was imaged at 1–2 MHz using a Shimadzu HPV-X2 camera equipped with a high-speed image intensifier (Lambert Instruments, HiCatt 25) and a 45-mm f/1.8-UV camera lens (Sodern, UV-Cerco). A 320 +/- 20-nm band pass filter (Semrock, FF02-320/40-50) was used to help spectrally separate the OH-PLIF signal from broadband flame emission and laser scattering. The intensifier gate was set to a 40-ns exposure time to further minimize broadband flame emission and prevent motion blur (< 2 pixel)

from ultrafast motion of the detonation wave. The Shimadzu camera can capture a total of 256 interlaced images of 400 x 250 pixels at framing rates of up to 10 MHz, which allowed recording of an entire detonation cycle (~245 μs) at 1 MHz. The PLIF image resolution was ~300 μm/pixel. Image acquisition of detonation waves were started 500 ms after the start of RDC operation, well after the detonation waves reached stable limit-cycle behavior within each 1 s test.

The RDC rig in the current experiment used ambient temperature air and hydrogen fuel. The air was injected from a circumferential slot located on the outer diameter (Figure 3.1(b)). The hydrogen fuel was injected as a jet in crossflow into this air stream using 100 discrete orifices. The detonation waves were initiated in the annulus ($Ø_{mean}$ = 125 mm) using a predetonator blast at the beginning of the test. Once initiated, the detonation wave propagated in the azimuthal direction around the annulus (see Fig. 3c), with a mean tangential velocity of ~1540 m/s and a cycle frequency of 4081 Hz, corresponding to a period of 245 μs. Additional details of the RDC geometry and its operation are presented in [16]. A global equivalence ratio of 1.0 was chosen with an air-injection mass flux of 750 kg/m^2/s. The outer body of the RDC was a transparent fused quartz cylinder, providing optical access to the annular injection system and combustion channel.

3.3 Results

3.3.1 OPO characteristics

The characteristic features of the MHz-rate burst-mode OPO laser output are shown in Fig. 2. The conversion efficiency of the OPO at 609 nm is plotted in Figure 3.2(a) as a function of pump energy. The data show that OPO conversion efficiency reaches ~11 % and ~3 % at 1 MHz and 2 MHz repetition rates, respectively. The lower conversion efficiency for the 2-MHz rate results from the low pump energy. To improve 2-MHz OPO conversion efficiency and stability, the pulse width is reduced from 5 ns to 2.6 ns, resulting in ~3.5% conversion efficiency. The temporal profiles of the burst-mode laser 532-nm pulse and OPO signal pulse, together with the relative time delay between them, are shown in Figure 3.2(b). The delay was optimized for maximum SFM. The pump (355 nm) temporal pulse profile is nearly the same as that of the mixing beam (532 nm). Typical burst profiles including individual pulse energies from the burst-mode laser, OPO, and SFM for a 150-μs burst duration at 1 MHz and 110 μs at 2 MHz are displayed in Fig. 2c and 2d, respectively. The burst duration was limited to ~150 μs because of the limited camera frame

recording provided by the Shimadzu camera and to avoid damage to the OPO optics due to the high total energy in the burst. Approximately 400 µJ/pulse (>150 pulses) and 150 µJ/pulse (>220 pulses) at 284 nm were generated for the 1 MHz and 2 MHz cases, respectively. The pulse-to-pulse standard deviations for 1-MHz and 2-MHz 284-nm pulse train across the burst (after reaching a plateau) are ~6.1 % and ~25 %, respectively. The observed high fluctuation in the 2-MHz OPO pulse train results from operating the OPO near the pump intensity threshold.

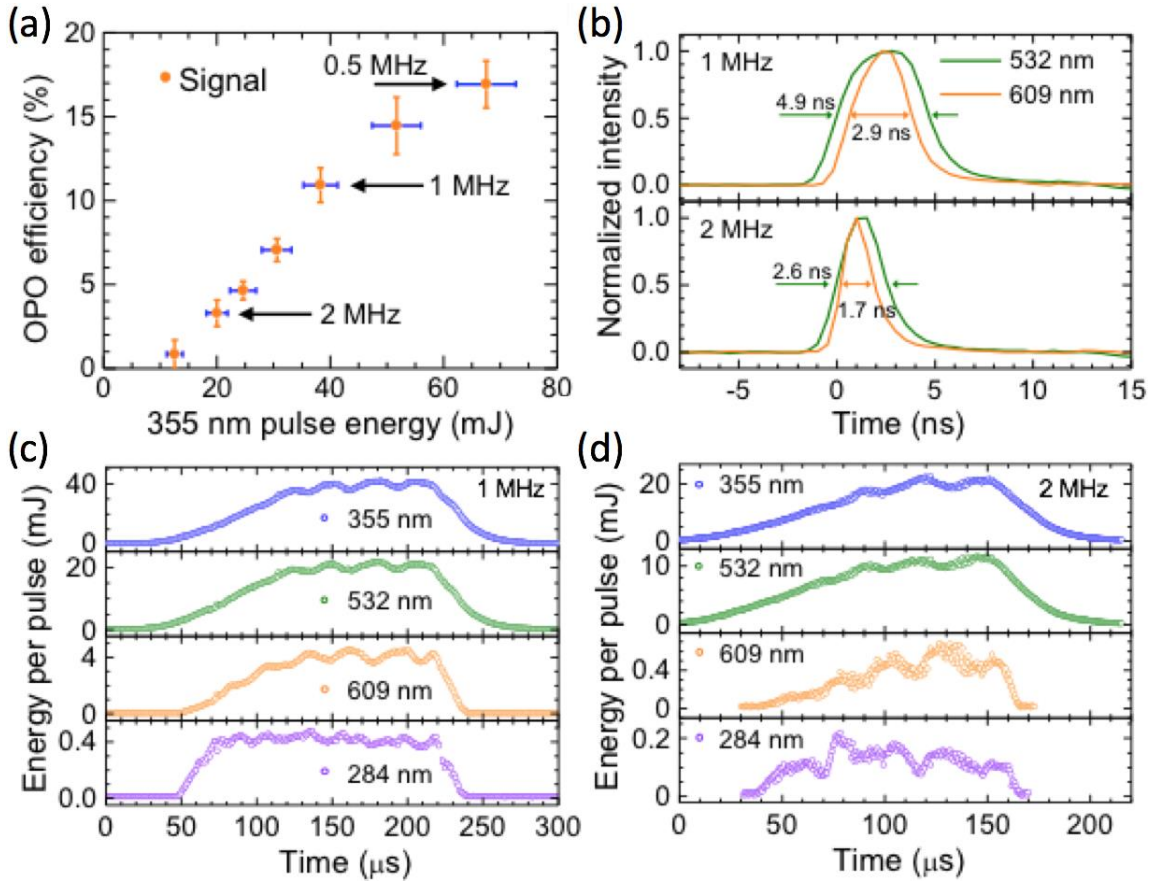

Figure 3.2: (a) OPO output conversion efficiency as a function of pump-pulse energy (5-ns pulse). (b) Temporal profile of OPO signal output and burst-mode 532-nm laser pulse at 1 MHz and 2 MHz. (c, d) Burst profile of the corresponding 1-MHz and 2-MHz outputs from burst-mode laser (355 nm, 532 nm), OPO (609 nm), and SFM (284 nm).

3.3.2 OH-PLIF in RDC annulus

The developed MHz OH-PLIF imaging system allows tracking of the flame reaction zone structure and combustion dynamics with to elucidate the physics and chemistry of the RDC. Figure 3.3 (a) and (b) show the PLIF interrogation region geometry in the RDC, and Figure 3.3(c) shows a

selected sequence of sixteen images (out of 150). The images were corrected for background and camera noise, image distortion, and laser beam profile nonuniformity.

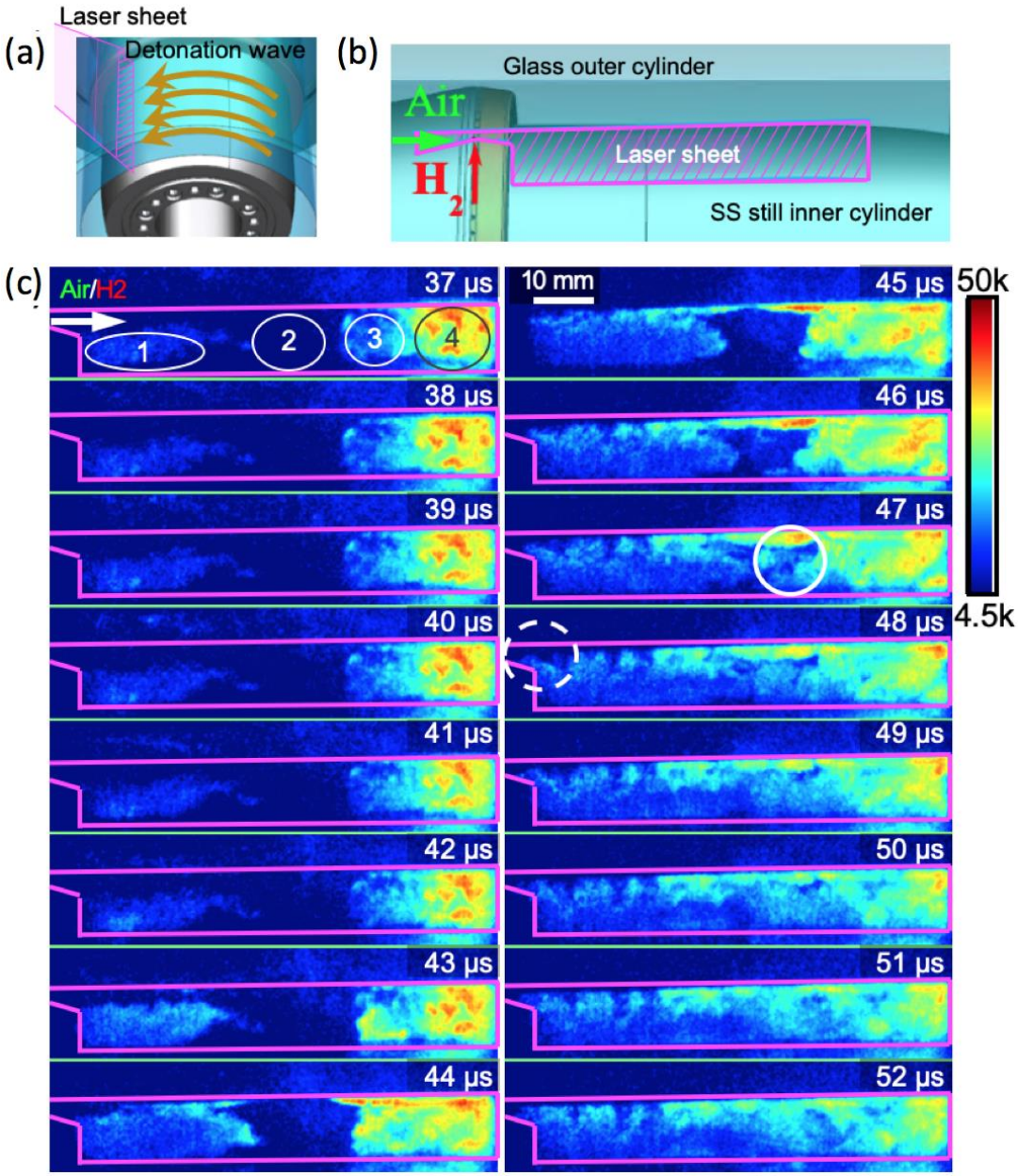

Figure 3.3: 1-MHz OH-PLIF imaging an RDC. (a) The laser sheet orientation relative to the propagating detonation wave. (b) A cross-section of the annular RDC that is normal to the detonation propagation direction, with major parts indicated. (c) Partial time-lapse image sequence showing the variation of RDC flame reaction zone structure. The color bar represents the relative OH signal in arbitrary units.

Across the time period shown in Figure 3.3 (c), the flow field evolution can be separated into three primary phases. The first phase captures air-fuel mixture refilling the combustor channel (37–42 μs). As the flow enters the channel, Region 1 (see the first frame of Figure 3.3 (c) for the indicated regions) identifies a recirculation zone created by the sudden flow expansion from the geometric step and is filled with combustion products from the previous cycle (i.e., OH) [16,51]. The observed OH signal magnitude in the Region 1 is low as the freshly injected air and fuel are entrained into the recirculation zone. Region 2 is an area devoid of OH and signifies the unreacted air-fuel mixture, which arrives from the inlet stream above Region 1. Regions 3 and 4 identify deflagration and combustion products that are advancing towards the combustor exit. The large differences in the observed OH signals and gradient levels suggests that Region 3 is subject to lower of deflagration along the interface of Region 2 (fresh air and fuel) with the much hotter combustion products from the previous detonation cycle (Region 4).

The second phase is the passage of the detonation wave, rapidly consuming the reactants and producing OH (43–46 μs). At 43 μs, Regions 1 and 3 show a sudden increase in OH signal in broad spatial regions, marking the arrival of the detonation-wave combustion products. The early arrival of the combustion wave in the recirculation zone of Region 1 and the end of the refill zone in Region 3 can be attributed to the presence of hot combustion products that increase temperature thereby increasing the speed of sound. Hence, the detonation-wave structures in Regions 1 and 3 propagate ahead and consume the partially mixed reactants and leads the remaining detonation wave front in Region 2, which shows combustion products by 46 μs.

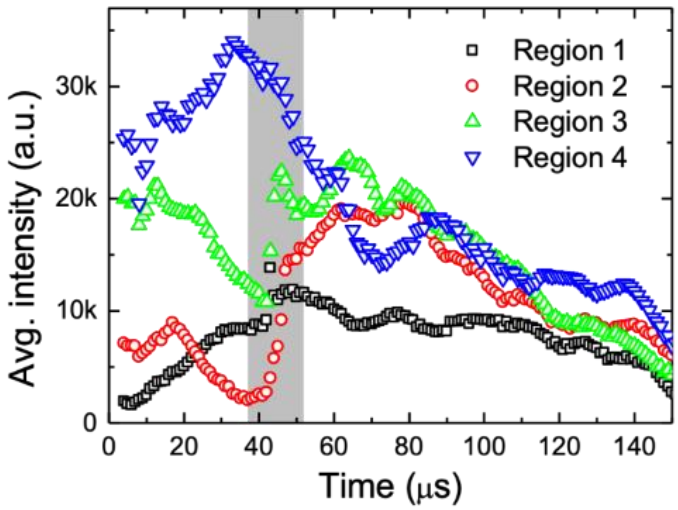

Figure 3.4: Temporal evolution of integrated OH intensity in the four regions shown in Fig. 3c. The gray rectangle indicates the time window shown in Figure 3.3 (37–52 μs).

The third phase shown in Figure 3.3 (c) describes the flow field immediately after the passage of the detonation wave (47–52 μs). At 47 μs, islands devoid of OH (e.g., within the white circle) are observed indicating unburned pockets of air and fuel. As time progresses, these pockets progressively shrink and are converted to OH, showing the existence of a highly three-dimensional detonation wave. Additionally, beginning near 48 μs there is OH upstream of the step (dotted circle) coinciding with the passage of the detonation wave. This indicates that a small fraction of the combustion products is forced into the injection system to mix with fresh reactants, due to the high pressures behind the detonation wave momentarily reversing the injection pressure gradient and stopping the inflow of reactants.

Figure 3.4 shows the integrated OH intensity time profiles of the four regions shown in Figure 3.3 (c). The RDC flame structure is associated with a large dynamic range of time scales. Region 1 shows the first rise in OH intensity in the first phase (37–42 μs), with Region 2 appearing next at (43–46 μs). While Region 3 has a similar rate of increase in OH signal as Region 2, its initial low intensity appears as a delayed arrival until after Region 2. All three regions display large intensity gradients due to the detonation wave passing through the PLIF plane, capturing the detonation propagation and primary fuel consumption behavior in a time window of about 15 μs for Region 1 and about 5 μs for Regions 2 and 3. Conversely, on a sub-millisecond time scale (1–40 μs and 50–140 μs), the RDC prepares a fresh fuel-air mixture for the subsequent detonation passage. Together with these events are changes that occur over a wide range of timescales. For example, Region 2 displays a sharp decrease in OH at 20–40 μs, indicating rapid dilution of the recirculation zone OH with fresh fuel and air, thereby enabling strong combustion at this location when the detonation wave passes through it.

Compared to recent chemiluminescence imaging of RDC diagnostics [11,12], the demonstrated MHz-rate OH-PLIF can visualize and track the spatiotemporal evolution of the recirculation region and combustion products (e.g., Regions 1–4), which cannot be resolved by line-of-sight averaged techniques such as chemiluminescence imaging. Of particular note is the initial propagation of the detonation wave closer to the inner radius of the annulus (as evident by comparing images from 42-43 μs), followed by propagation with intense OH signals at the outer radius thereafter. Such detonation-wave dynamics and spatial structure can provide detailed insight on the under lying physics, as well as data for validation of high-fidelity numerical simulations.

3.4 Conclusions

This work shows the potential for MHz OH-PLIF imaging to enhance understanding of highly dynamic combustion phenomena at speeds exceeding 1500 m/s. The measurement speed is ten times faster than previous OH-PLIF experiments in turbulence flames [49]. The proposed system generates more than fifteen times the number of pulses with higher per-pulse energies as compared to previous MHz-rate burst-mode OPOs [47]. The OPO conversion efficiency, pulse characteristics, burst profile in time, and frequency conversion to the UV are described for rates up to 2 MHz. OH-PLIF images presented here reveal cross-sections of the detonation-wave structure at a rate of 1 MHz, with a 2 MHz sequence also provided (see Visualization 2). A key limitation of the current imaging technology is the phosphor decay time of 0.5–1 μs for typical high-speed camera intensifiers, which can lead to residual signals from one frame to the next. Increased measurement speeds above 1 MHz are viable using the current burst-mode OPO system with improved high-speed intensifiers to preserve sensitivity and image quality.

4. ON THE NATURE AND ORIGIN OF TRAILING DETONATION WAVES WITHIN ANNULAR COMBUSTION CHANNELS REVEALED BY SIMULTANEOUS MHZ-RATE OH-PLIF/CHEMILUMINESCENCE AND NUMERICAL SIMULATIONS

The coupled effects of fuel-oxidizer mixture preparation and complex detonation wave structure are investigated within a hydrogen-air rotating detonation combustor (RDC) using 1 MHz broadband chemiluminescence imaging, 1 MHz hydroxyl radical planar-laser induced fluorescence (OH-PLIF), and three-dimensional reactive unsteady Reynolds averaged Navier-Stokes (URANS) simulations. The combination of highly spatio-temporally resolved optical diagnostics and numerical study enabled detailed observation and interpretation of the in-situ combustion dynamics and their sensitivity to the reactant inflow conditions. Air mass flow rate was varied from 0.22 kg/s to 0.9 kg/s at near stoichiometric conditions and resulted in varying residence times and fuel stratification ahead of the detonation wave, leading to the occurrence of (i) weak detonation zones close to the injection plane and strong detonation zones further downstream and (ii) combustion of unburned reactants in the azimuthal shocks trailing the weak detonation wave. The unburned reactants that pass the leading detonation wave, eventually mix and combust at the trailing azimuthal shock system as a trailing shock-induced detonation, resulting in additional isochoric heat release in the wake of the weak-detonation zone. The axial length of the azimuthal reflected shock combustion is dependent on the unburned reactants available in the wake of the leading detonation, a quantity that monotonically decreases with increasing axial distance from the injection plane due to increased mixing of fuel and air. The combined use of MHz-rate imaging within the combustor passage and numerical simulations was instrumental in corroborating the source and effects of the azimuthal reflected shock combustion in the injection near-field that would otherwise be difficult to discern from single-shot or time-averaged imaging. These coupled phenomena impact the local detonation wave structure, combustion intensity distribution, and local flow properties without significantly altering the overall wave propagation velocity, lending insight into the mechanisms and design features that can impact combustion mode and efficiency in non-premixed rotating detonation engines.

4.1 Introduction

Rotating detonation engines are of significant interest for their potential to achieve pressure-gain combustion in continuous flow devices and to increase thermodynamic efficiency over conventional constant pressure combustion devices with similar fuel-oxidizer combinations [4,27]. The last two decades have seen extensive research and development of these systems from laboratory-scale engines to practical applications [2,4,7,56]. However, achieving the ideal pressure gain in a non-premixed rotating detonation combustor (RDC) requires a detailed understanding of the complex effects of the reactant mixing field and the detonation wave structure within annular combustion channels.

To understand the dynamics of detonation waves propagating through a continuous inflow of reactants, linear channels have been used as an analogue to annular RDCs with direct optical access to the mixing and combustion zones [19,21,35]. These studies allow observation of key features such as the reactant refill height, the oblique shock and triple point locations, and the instantaneous structure of the detonation wave. Linear channels, however, do not replicate the physics involved in the interaction of the detonation wave with curved surfaces. An alternative to the linear channel is a "racetrack" or obround-shaped geometry [17,28,57], in which curved detonation channels lead into straight sections with ready optical access. Recently, Chacon et al. [54] performed 10 Hz hydroxyl radial planar-laser induced fluorescence (OH-PLIF) measurements and showed that the detonation-wave surface interactions in the curved sections of an obround RDC were not preserved in the linear sections where the PLIF measurements were performed. In high-speed wall-pressure measurements performed by Wen et al. [39] in a hydrogen-air obround detonation combustor, a second weak pressure spike was observed in the curved section which was absent in the linear section. Although the authors alluded to injection recovery as the source of the trailing pressure spike, injection recovery occurs in both the linear and curved sections, indicating that this may be a feature of the detonation wave dynamics that differs between curved and straight channels. Pressure measurements using two transducers azimuthally spaced 45^{o} apart and located at the same axial location downstream in a fully annular RDC also support the existence of trailing pressure waves in curved detonation channels [58]. Comprehensive understanding of the sources of non-ideal detonation-wave structure in RDCs, therefore, requires detailed interrogation of the spatio-temporal distribution in representative annular geometries that

have ample access to optical diagnostics and/or are amenable to three-dimensional numerical simulations.

Several studies have been conducted with optically accessible RDCs for characterization of the detonation structure in annular channels [11,16,29,59]. Rankin et al. performed instantaneous high-speed chemiluminescence and infrared imaging in an optical non-premixed H_2-air RDC with radial-air/axial-fuel injection to enable observation of the instantaneous and phase-averaged detonation wave structure [11]. Fugger et al. improved the image repetition rate to 1 MHz for the same RDC and showed a highly non-uniform time-resolved curved detonation-front propagation [60]. Athmanathan et al. used 1 MHz broadband chemiluminescence and unsteady Reynolds averaged Navier-Stokes (URANS) simulations in a non-premixed H_2-air RDC with radial fuel/axial air injection and showed significant axial variations in the detonation wave structure within the reactant fill zone [16,51]. Recent OH* chemiluminescence measurements by Matsuoka et al. showed a luminous wave trailing the leading detonation front for test conditions with low injection pressure drop [61], further highlighting the significant spatial inhomogeneities that can result from the complex flow-shock-combustion dynamics and the need to improve understanding of the underlying physics.

A common feature that requires further investigation in these RDCs with various injection schemes is how the reactant filling process and fuel-oxidizer mixing interact with the shock system in the development and propagation of detonation waves within an annular geometry. To lend further insight into the complex spatiotemporal dynamics, Hsu et al. demonstrated spatio-temporally resolved MHz OH-PLIF measurements in the same optically accessible non-premixed RDC as used in the current work [62], revealing significant inhomogeneities due to unburned reactants and mixing of reactants with hot combustion products. Near the injection region, the detonation wave travels through stratified regions of highly heterogenous fuel and air mixture with small amounts of partial premixing [63–65], leading to a highly non-uniform and distorted detonation wave structure [63,66]. Due to unmixedness, a fraction of the reactants can pass through the detonation wave without combusting, which lowers the thermodynamic performance [67]. Other loss mechanisms that degrade the isochoric heat release process include deflagration due to contact between fresh reactants with high-temperature products [68–70], product expansion following the detonation wave that can alter the injection blockage and recovery pressure, and reactant refill dynamics pertaining to the combustor geometry and stiffness of the injection system.

While high-speed imaging within an optically accessible RDC has provided some indications of the salient physics, there are relatively few studies directly comparing spatio-temporally resolved diagnostics and numerical simulations of the three-dimensional (3D) geometry, which are critical to reveal the coupled interactions between the detonation wave and near-field reactant mixing in annular configurations. This work focuses on developing a detailed analysis and understanding of the complex spatio-temporal evolution of the reactant flow field and detonation wave structure within an annular RDC by combining MHz-rate chemiluminescence, MHz-rate OH PLIF, and 3D reacting URANS simulations. The work is accomplished using an RDC designed for full optical access spanning from the air plenum to the exit plane [13]. The analyses provide a comprehensive look at non-ideal shock-flow interactions, revealing new details such as the role of unmixedness and azimuthal shock structure on the nature and origin of trailing detonation waves within annular combustion channels.

4.2 Experimental Setup

4.2.1 Experimental apparatus

A schematic cross-section of the optically accessible RDC is shown in Figure 4.1 (a), with a ~20 mm thick quartz outer body having an inner diameter of 136 mm and serving as the outer wall of a combustor channel with a 10.7 mm width. High-pressure air enters from a plenum through an annular converging-diverging section with a throat gap of 1.42 mm. Fuel is injected radially through 100 equally spaced slots in a jet-in-crossflow arrangement slightly downstream of the air injection throat. The fuel slots are milled with a 0.6 mm diameter end mill to a depth of 0.4 mm and are located at an area ratio (ε) of 1.16 relative to the area at the throat. The flow channel expands up to $\varepsilon = 1.81$, leading into the combustor channel ($\varepsilon = 7$) through a backward facing step (BFS). The air and fuel injector stiffness, based on the mean pressures, is defined as $\frac{\overline{P}_{plenum} - \overline{P}_{chamber}}{\overline{P}_{chamber}}$ and is ~ 2.2 for the current fuel injector configuration. The hydrogen and air mass flows are metered using choked sonic nozzles. The dry air flow rate is varied from 0.21 kg/s to 0.9 kg/s to reach air throat mass fluxes of G_{air} = 350 kg/m^2/s to 1500 kg/m^2/s, respectively. Hydrogen can be metered to reach a global equivalence ratio (ϕ_{global}) up to 2.0. The uncertainty in gaseous propellant mass flow rate is computed to be ~2%. Pressure transducers (UNIK 5000) and thermocouples are used

for monitoring the pressure and wall temperature at 2 kHz with an uncertainty of ±1 psia and 0.1 K, respectively.

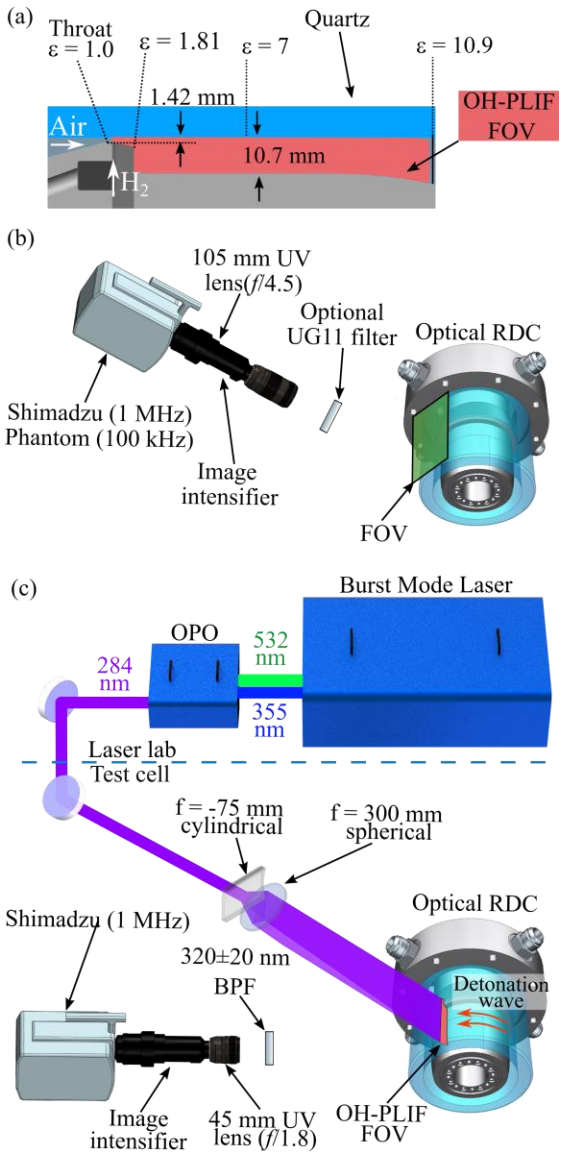

Figure 4.1: (a) Radial-axial cross-section of flow path, (b) side-view arrangement for chemiluminescence imaging, and (c) experimental setup for MHz OH PLIF. The OH-PLIF system images the radial-axial plane shown in (a), which is orthogonal to the azimuthal-axial viewing direction of the chemiluminescence plane shown in (b).

The experimental diagnostics are shown in Figure 4.1 (b) and (c). High-speed broadband chemiluminescence is employed at 100 kHz and 1 MHz repetition rates, with the former capturing multiple cycles for phase-averaged measurements and the latter capturing the detonation wave

passage in time. The imaging system shown in Figure 4.1(b) utilizes two different high-speed cameras depending on the framing rate, including a Shimadzu HPV-X2 camera capable of up to 256 sequential frames with 250×400 pixels at 10 MHz and a Vision Research Phantom v2012 camera capable of up to 1×10^6 frames with 300×300 pixels at 100 kHz. The high-speed cameras are coupled to an image intensifier (Lambert Instruments, HiCatt 25), capable of operating at speeds of 1 MHz with exposure times as short as 40 ns. A 105 mm $f/4.5$ camera lens with a transmission spectrum ranging from UV to visible wavelengths is used with the imaging system. This optical setup allows for imaging of broadband chemiluminescence with a spectral bandwidth of 280–800 nm, including OH* chemiluminescence (280 – 320 nm), emission from radicals in hydrogen-air combustion (320–500 nm), and visible to near-infrared emission from water vapor (600 nm – 10 μm) [32]. The OH* chemiluminescence emission intensity is an order of magnitude higher than the other flame emission regimes, as detailed in Ref. [32]. The intensifier time gate is set to 100 ns to reduce motion blur, giving a detonation wave displacement of less than 1 pixel during exposure. The camera is focused on the RDC annulus to visualize the wave traveling through a circumferential range of nearly 180º, with a field of view (FOV) axially extending from ~10 mm upstream of the air-injection throat to the exit plane of the flow channel.

MHz-rate OH PLIF, shown in Figure 4.1 (c), is collected simultaneously with chemiluminescence from Figure 4.1 (b) to capture the radial-axial and axial-azimuthal structures of the detonation wave, respectively. The experimental setup used for the OH PLIF measurement is described in the prior work by Hsu et al [62] and is summarized here for convenience. An Nd-YAG burst-mode laser (Quasimodo, Spectral Energies, LLC) pumps a custom built OPO (Spectral Energies, LLC) to produce a 4 ns wide, 284 nm excitation laser pulse at 1 MHz repetition rate to excite the $Q_1(9)$ transition of OH [62,71]. The pulse-train produce ~200 pulses at this repetition rate with ~400 μJ/pulse. This laser-pulse is transmitted to the RDC test cell from a remote laser lab using UV-coated mirrors, and sheet-forming optics are used to form a ~0.5 mm thick × 100 mm wide laser sheet to visualize the radial-axial structure of the detonation wave during passage. The sheet enters normal to the quartz cylinder and at an angle of 45◦ with the camera. Because of the curvature of the 20.75 mm thick quartz window, the object plane was adjusted to be in line with the camera axis. The PLIF spatial domain provides a field of view extending from the fuel-injection site upstream of the BFS to the exit plane of the RDC, as shown in the Figure 4.1 (c) (FOV shown in red). A 320 +/- 20-nm band pass filter (Semrock, FF02-320/40-50) was used to

help spectrally separate the OH-PLIF signal from broadband flame emission and laser scattering. The resultant fluorescence is captured by a Shimadzu HPV-X2 camera coupled to an image intensifier (HiCatt 25) with a time-gate of 40 ns to preferentially capture the OH-PLIF and reject OH* chemiluminescence from the detonation front. In addition to the OH-PLIF camera, another Shimadzu HPV-X2 camera was coupled to an image intensifier (LaVision IRO) with the camera-axis positioned parallel to the laser-sheet entering the RDC. The OH* chemiluminescence camera (FOV shown in green) uses a 100 ns gate to capture the axial-azimuthal detonation structure during wave passage through the PLIF plane. Both the PLIF and chemiluminescence cameras were synchronized with the MHz laser system and were remotely triggered by the RDC auto-sequence system at ~300 ms after initiation of detonation (several hundred wave passages after a steady detonation has been achieved).

4.2.2 Experimental procedure and conditions

The RDC test is remotely operated with automated valve and camera-trigger timing controlled by a 2 kHz data acquisition and control system. At the start of the test, air and hydrogen flow through the RDC for ~0.5 seconds to prime the RDC with reactants. A H_2/O_2 predetonator charge enters radially outward into the primed combustion chamber at an axial location ~25 mm from the fuel injection site. This charge initiates detonation waves that reach limit cycle behavior within ~40 ms based on visualization of the end-view of the RDC and the imaging system was triggered ~400 ms after RDC ignition. Each RDC test lasts for ~1 s after initiation, at the end of which the fuel valve is shut off and the fuel lines are purged with nitrogen. The Shimadzu camera is used to collect 256 frames at 1 MHz while the Phantom camera captures 10,000 frames at 100 kHz. Images from the Shimadzu camera are used to visualize a single cycle of the detonation wave while the Phantom camera is used to capture ~400 detonation cycles occurring over 100 ms. This large image sequence dataset provides a statistically significant number of images to obtain the phase-averaged detonation structure at different operating conditions.

The operating conditions used in this study are tabulated in Table 1. The RDC is operated at four different mass fluxes at a mean global equivalence ratio of ~1.07 with a coefficient of variation of ~2%. Because of the relatively small coefficient of variation in the global-equivalence ratio, the dominant parametric change across each case is assumed to be the change in the air-mass flux. Case 2 is considered the baseline condition for this study, where computational modelling was

performed for comparison with the experimental results from broadband chemiluminescence and OH PLIF. Chemiluminescence imaging was performed at 100 kHz for all four cases and at 1 MHz for Cases 1 and 2. The high mass fluxes present in Cases 3 and 4 posed challenges associated with potential cracking of the quartz window due to high chamber pressures and heat flux loads. Hence MHz-rate experiments were limited to Cases 1 and 2 to avoid potential damage to imaging equipment.

Table 1: Operating conditions of the RDC. Case 2 is considered to be the baseline condition.

Case	G_{air}(kg/m^2/s)	$\dot{m}_{air}$(kg/s)	$\dot{m}_{hydrogen}$(kg/s)	ϕ_{global}
1	350	0.21	0.007	1.10
2*	750	0.45	0.014	1.05
3	1125	0.68	0.021	1.07
4	1500	0.91	0.029	1.06

4.3 Numerical model

4.3.1 Model introduction and parameters

To assist in the interpretation of the imaging results, a complementary 3D URANS non-premixed simulations are performed. The URANS equations were solved with CFD++ developed by Metacomp [72]. The solver performance was evaluated and qualified for compressible flow characterization in non-reacting supersonic environments [73]. For the reacting flow case of RDCs, a one-step chemistry model was implemented based on the reaction mechanism used by Frolov et al. [74]. Grid and time-step independence studies were performed on the reacting flow-solver in a two-dimensional detonation tube [34]. With a time-discretization of 0.1 μs and the use of one-step reaction model, the solver predicted a wave speed within 2% of the Chapman-Jouguet (C-J) condition. The numerical domain of the combustor, shown in Figure 4.2 (a), consisted of the air plenum, air injection throat, 100 fuel injection slots, and the combustion region downstream of the BFS. A structured grid (using ICEM CFD) with boundary layer mesh refinement was implemented with a total of ~48.5 million cells. The maximum non-dimensional wall distance, y+, was 14 within the detonation front on the outer diameter of the annulus, while y+ on the inner diameter of the annulus was below 1 to resolve at least one point in the laminar sublayer. The simulations were

initially started on a coarse grid without resolving the boundary layer (slip walls), and mesh refinements were applied after initial computation on a coarser grid for about 30 cycles. For the boundary-layer refined mesh, adiabatic non-slip walls were applied. The numerical boundary conditions were supplied from experimentally derived pressure measurements for test Case 2 (Table 1) for G_{air} = 750 kg/m^2/s and Φ_{global} = 1.0. A total pressure and total temperature of 5 bar and 290 K were imposed in the air plenum while a total pressure at the fuel injection ports was

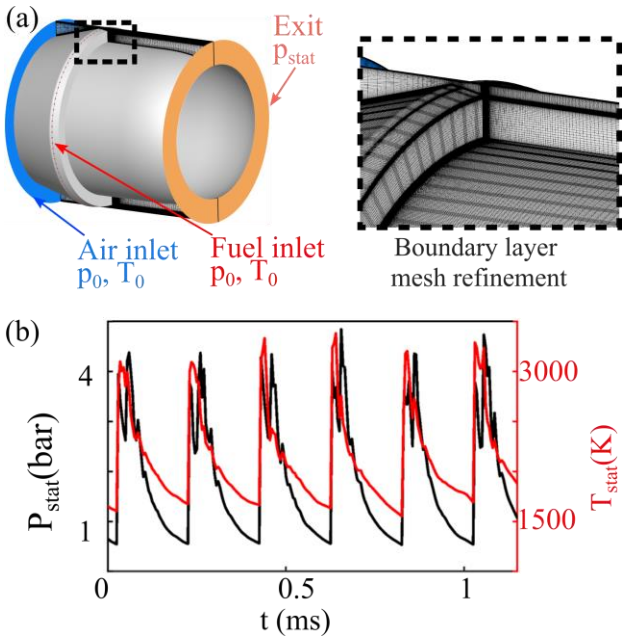

Figure 4.2: (a) Computational domain and mesh refinement, and (b) pressure and temperature trace 1 mm downstream of the backward facing step (BFS).

5.35 bar with a mixed supersonic/subsonic boundary condition at the outlet where the outlet static pressure was set to 1 bar. The mass flow of the reactants converged to a steady state value of 0.02 kg/s for hydrogen and 0.62 kg/s for air. At steady state, the numerical model reached Φ_{global} = 1.1. The CPU time to achieve one detonation cycle was approximately 48 hours on 120 high-performance computing (HPC) cores, and around 30 cycles were run on the fine mesh. Figure 4.2 (b) shows a pressure and temperature trace sampled each 5 μs at a radial location r = 0.059 m near the inner end wall for the last six detonation cycles at an axial location of 1 mm downstream of the BFS. The temperature near the inner wall shows that this region is filled with exhaust gases expelled by the detonation wave and never quite reaches inlet air-fuel mixture inlet temperatures,

as depicted on Figure 4.2 (b), where temperature always remains above ~1600 K. The static pressure downstream of the recompression wave due to the detonation wave passage is ~4.8 bar.

In addition to the grid and time step independence trade-off studies performed for the solver, a commonly used parameter to compare simulation results with experiments is the percent deviation of detonation cycle frequency with the experimental counterpart. Prior work by Lietz *et al.* used a large eddy simulation (LES) model on a hexahedral grid with 90 million cells for a rotating detonation rocket engine (RDRE) and approached to within 8% of the experimental cycle frequency [65]. Sato et al. used a 28 million unstructured mesh in a non-premixed RDC and approached within 15% of the experimental cycle frequency at the same fuel-air combination in a comparable geometry [66]. In this work, the predicted RDC cycle frequency is within 7% of the experimental counterpart (4.3 kHz), with more detailed comparisons to the optical diagnostics discussed in the results to follow.

4.4 Results and discussion

The results are organized into three sections. The first section describes the observed detonation wave structure and the propagation physics from 100 kHz and 1 MHz broadband chemiluminescence imaging at various mass fluxes. These results establish the persistence of leading and trailing combustion waves, as well as their general spatial characteristics in the axial-azimuthal view. The second section explores the 3D physical processes that drive the detonation and wake physics by combining results from (i) simultaneous MHz-rate OH* chemiluminescence and OH-PLIF imaging and (ii) URANS simulations. These results identify the origins and nature of the trailing combustion wave as being associated with incomplete combustion of the stratified reactants and shock-induced detonation in the near field. Having confirmed the ability of the URANS simulations to capture the effects of reactant stratification on the detonation wave dynamics, the third section further explores the underlying compressible flow physics that affect reactant stratification in non-premixed RDCs and implications for achieving isochoric combustion in practical propulsion and power systems.

4.4.1 Non-premixed detonation-wave structure and propagating physics

Time-resolved MHz rate imaging studies

In this section, MHz broadband chemiluminescence images at Case 2 (baseline condition) and 1 corresponding to G_{air} = 750 kg/m^2/s and G_{air} = 350 kg/m^2/s respectively, at nearly stoichiometric global equivalence ratio, are analyzed. The images presented are cropped to view ~ 84 mm x 84 mm field-of-view (FOV) with the axial and azimuthal direction oriented along the horizontal and vertical direction. The FOV extends from the fuel-injection plane up to ~10 mm upstream of the exit plane. Spatial-transformation to map the azimuthal co-ordinate to a planar-field was not performed since such transformations significantly increased image blur in the vertical direction, which reduced the spatial-resolution. However, the camera aperture was reduced to have a large depth of field to capture the wave-passage around azimuthal angle in the FOV. The yellow-line at 1 μs in Figure 4.3 (a) and (b), marks the BFS location at both test conditions and the timestamp is located for each image.

For the baseline condition shown in Figure 4.3 (a), the instantaneous image shows a complex detonation wave front that is curved along the axial direction with a convex-concave-convex structure with respect to the direction of propagation (Label A). The concave feature is located ~ 30 mm from the injection plane and is observed to form as a result of the intersection of the convex features in the injection nearfield and farfield. Through the entire image sequence, local variations in intensity can be observed at the leading front, however, the curvature and shape are maintained. These details on the local-variations through the use of time-resolved imaging provides spatial-detail that is typically absent in phase-averaged imaging studies. The curvature effect is attributed to the local temperature field ahead of the detonation wave and will be explored in Section 0. Qualitatively, based on the luminosity, the detonation structure can be demarcated into Zones I and II (7μs and 8 μs), with the former zone located in the injection nearfield and the latter zone in the injection farfield. Zone I is observed to have much lower and more spatially diffuse detonation luminosity than Zone II. Ahead of the detonation, due to Zone I's vicinity to the injection plane, the axially injected reactants can be expected to be relatively unmixed and fast-moving. The injector stiffness of ~2.2 for this test condition combined with the converging-diverging injector scheme is expected to sustain supersonic axial injection of fuel and air ahead of the detonation wave, resulting in local static quantities in Zone I to be lower than Zone II. In Zone II, due to the longer residence time of the reactants and the drop in momentum (from various loss

mechanisms, as will be explored in detail), the reactants are expected to be relatively well-mixed and have higher static quantities. Thus, the higher luminosity levels observed in the Zone II compared to Zone I are attributed to the relative increased air and fuel mixedness and increase in reactant static quantities in Zone II. While spatial variations exist in the reactant mixedness in the axial direction, the leading edge of the combustion wave in the two zones travel at a mean speed of approximately 82% of the Chapman-Jouget (CJ) speed, indicating this structure is a detonation wave. A detonation wave speed lower than CJ is to be expected from prior work in non-premixed systems [11,29]. As the wave progresses azimuthally, the stronger detonation wave zone begins translating axially which is dependent on the refill height and local mixing efficiency of reactants present ahead of the detonation.

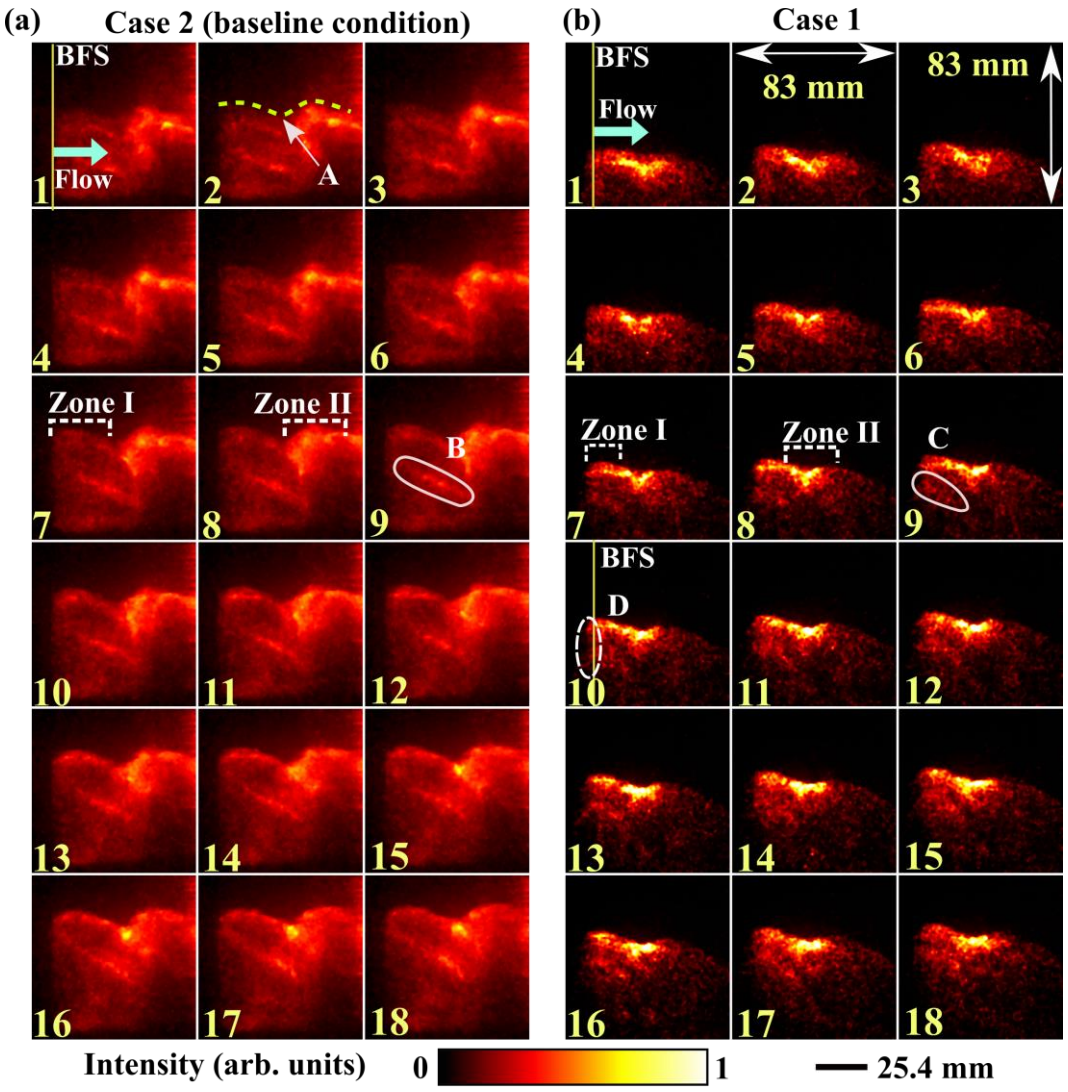

Figure 4.3: 1 MHz broadband chemiluminescence image sequence of detonation wave propagation for (a) test Case 2 at the baseline condition and (b) test Case 1. Sequential numbering corresponds to 1 μs time step. Zones I and II have poorly mixed and well-mixed reactants, respectively. The azimuthal shock induced combustion is observed at 9 μs for both Cases 2 and 1 shown as B and C.

In RDCs, due to the curvature of the annulus, the leading detonation wave forms an azimuthal reflected shock system to turn the burned gas in the wake of the detonation wave. For a ~ 10 mm channel gap, hydrogen-air fuel-oxidizer combination and mean radius of ~ 100 mm, numerical and experimental studies have shown the existence of these trailing azimuthal shock systems in RDCs [24,26]. In this RDC, azimuthal shocks are expected to trail the leading wave in both Zone I and II. Although the azimuthal shock system is present for both Zones I and II, a

trailing luminous wave is observed in Zone I where the reactants are expected to be poorly mixed, with no such trailing luminosity in Zone II where the reactants are expected to be well-mixed. The time-resolved imaging also shows that the separation between the leading and the trailing wave remains a constant through the entire cycle, indicating an inherent coupling between them. While the intensifier exposure was set to 100 ns to preferentially capture the heat-release occurring at the leading detonation front, the presence of a luminous trailing shock system in Zone I suggests the presence of combustion occurring at the trailing azimuthal reflected shock. As will be discussed in more detail in the following section, the formation of the azimuthal reflected shock combustion (ARSC) wave in Zone I is consistent with the interaction of the unburned reactants in the wake of the leading detonation front with the reflected shock train.

In the lower-mass flux case (Case I), the detonation structure is observed to have features very similar to the baseline case. At the lower mass flux, the detonation has an axially smaller convex-concave-convex structure, and the wave can be divided into Zone I and II as well. A corollary explanation on differences in luminosity observed due to unmixedness in Case 1 can be made from the baseline condition. The length of Zones I and II are relatively shorter than Case 2 due to anticipated lower axial velocity in the channel. The azimuthal reflected shock combustion (Label C in Figure 4.3) is observed to trail Zone I of the primary wave at a relatively smaller angular separation and length than Case 1, effects also attributed to lower wave-speed. At 10 μs, hot product backflow into the injection system can be observed, marked by chemiluminescence upstream of the BFS (label D in Figure 4.3 (b)), which was not observed for the higher mass flux Case 1.

Phase-averaged detonation structure

The use of time-resolved MHz-rate imaging, enables the identification of several key features of detonation propagation in non-premixed RDCs. These include wave curvature of the leading front, partitioning of Zone I and Zone II in the axial direction with Zone I having a weaker luminosity compared to Zone II and finally an azimuthal reflected shock combustion (ARSC) feature trailing the main detonation wave in Zone I, the injection nearfiled. In this section, images from 100 kHz broadband chemiluminescence are phase-averaged and the aforementioned wave features are identified in the phase-averaged images at all four test conditions. In adition to identifying the flow-features, this study also provides a contrast between the time-resolved images and phase-

averaged images, where the latter is commonly used in studying detonation wave structures. Without the use of time-resolved imaging, understanding the propagation physics becomes a challenge due to significant drop in spatial gradients and temporal information. However, post idenfitication of key features and studying their temporal response using MHz rate imaging, provides a better foundation to study the detonation structure and propagation physics using phase-averaged images.

For each test condition, the phase-averaged images are produced by averaging ~100 images from the 10,000 image stack at each condition. The ~100 images met a cross-correlation criterion, which ensures the visual similarity between the images, details of which are described in the appendix section. The flame luminosity increases transitioning from Case 1 through 4 and the image intensifier gains were appropriately lowered to minimize overexposure of the imaging system. The phase-averaged images for all four test cases are shown in Figure 4.4.

The first observation from the phase averaged images show that the leading front of the detonation wave, exhibits a convex-concave-convex feature at all four test conditions, which was attributed in the previous section to the local temperature field ahead of the leading front. While time-resolved imaging showed that local spatial variations in intensity does exist at the leading front within a single cycle, the axiallly dependent wave curvature is maintained. This shape-retainment over multiple cycles suggests that, once the RDC has reached limit cycle behavior, the periodic refill process produces a consistent ensemble temperature field ahead of the detonation wave.

The scond observation is the shows that the leading front can be qualitatively birfurcated into two zones viz. Zone I – corresponding to the injection nearfield and Zone II corresponding to the injection farfield. As previously discussed, Zone I has weaker luminosity due to relatively fast-moving and poorly mixed reactants ahead of the detonation wave and Zone II has stronger luminosity due to relativley slow-moving and well-mixed reactants ahead of the detonationw wave.

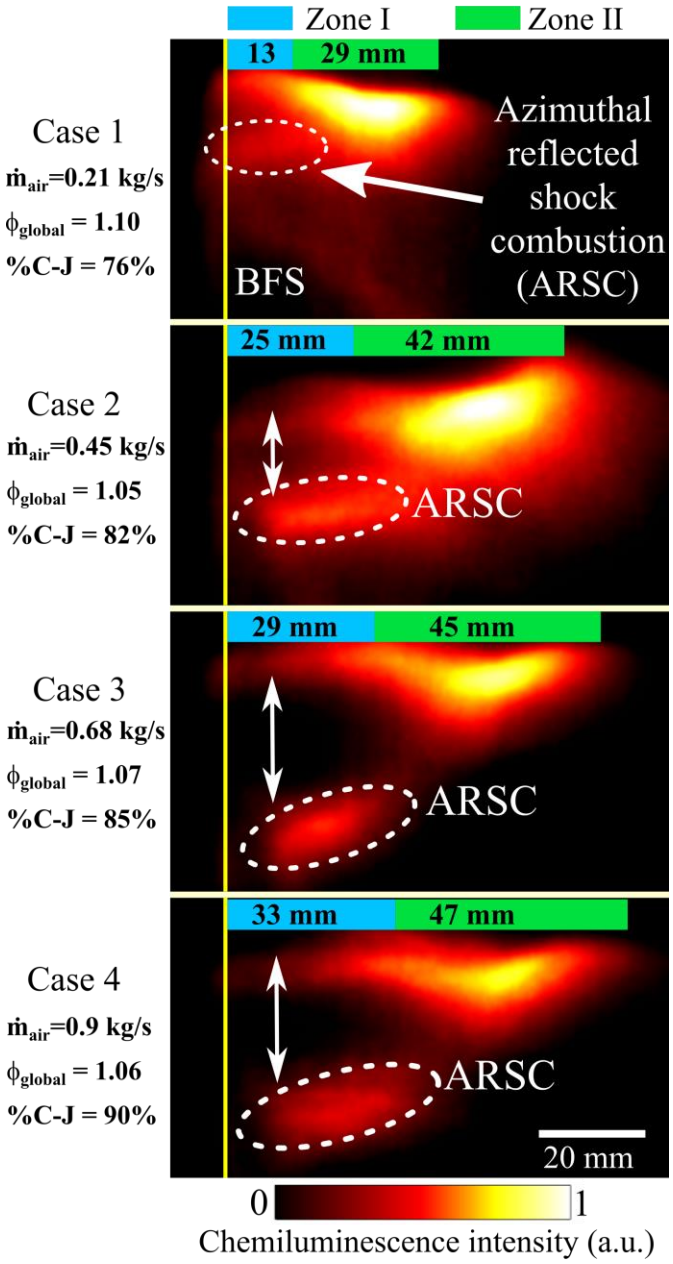

Figure 4.4: Phase averaged images of detonation wave at the four different mass flux cases investigated in this study. All four cases show the presence of axial variation in detonation structure corresponding with weak luminosity in Zone I and strong luminosity in Zone II due to variations in mixture stratification and flow static quantities. Presence of azimuthal reflected shock combustion in the injection nearfield due to curved surface effects and unmixedness – indicating dual heat-release zone in non-premixed RDCs.

With the increasing mass-flux a non-linear monotonic increase in wave height as well as the length of Zone I and Zone II is observed. A doubling of mass flux from Case 1 to Case 2 increases the

wave height from ~41 mm to ~ 67 mm, a ~16 mm increase. However the doubling of mass flux from Case 2 to Case 4 only results in wave height increase from ~67 mm to 80 mm, a ~13 mm increase. This indicates that the observed increase in wave-height starts to plateau with increase in mass flux from Case 1 to Case 4, suggesting a plateauing behavior in the reactant axial penetration depth. This drop in reactant penetration depth is likely due to the drop in axial momentum due to momentum loss mechanisms (shear layer interactions, axial shock formation), reasons which will be explored in detail through the use of URANS simulations in Section 4.4.3 and 4.4.4.

The third observation is the increase in the wavespeed with increasing mass-flux. At the mean equivalence ratio of ~ 1.07, for premixed hydrogen-air at ambient conditions, the Chapman-Jouguet velocity is computed to be 1984 m/s based on equilibrium calcualtions performed using NASA CEA [75]. The %C-J velocity increases from 76 % for the lower mass flux case and reaches up to 90% C-J for the highest-mass flux case. This increase in wave speed, reaching near C-J velocity, indicates that heat-release occuring at the detonation front is close to an ideal detonation wave with increasing mass-flux..

The fourth discerning feature observed at all four test conditions, is the presence of an azimuthal reflected shock combustion (ARSC) feature that is observed to trail the leading deotnation wave in the wake of Zone I. The chemiluminescence intensity in in Zone I and ARSC were binned to understand the relative strength of the leading detonation front and the trailing combustion zone. The chemiluminescence intensity of the Zone I is observed to be ~ 0.95 ±0.15 times the intensity of ARSC. This relatively close intensity between Zone I and ARSC susggest that the trailing wake-combustion plays a signficant role in the overall heat-release occuring in non-premixed RDCs. With increasing mass flux, the length of Zone I and correspondingly the length of the ARSC feature increases. The ARSC's axial length increase, is observed to depend on the length of Zone I, both of which are inherently coupled with the mixing field ahead fo the detonation wave. This observation also suggests that the unmixed zone length monotonically increases and eventually plateus with increasing mass flux, giving rise to an axial length increase in the ARSC feature. Additionally, the azimuthal separation distance between the Zone I and ARSC also shows an increase between Case 1 and 2 and starts to plateu between Cases 2,3 and 4, a behavior very similar to the wave height. This increase in azimuthal separation is observed as a result of the increasing wave-speed which, which in turn imparts a larger burned-gas velocity on the wake of the leading front.

4.4.2 Azimuthal shock system in non-premixed RDCs

Chemiluminescence comparison with URANS wave structure

The presence of azimuthal reflected shock combustion indicates that the detonation wave, although expected to have heat release occur in the leading front, appears to have a secondary trailing combustion wave called the ARSC feature. In this section, combined use of URANS simulations, broadband chemiluminescence and OH-PLIF will be used to explore the detonation structure in the radial-azimuth and radial-axial plane, formation of ARSC, the differences in the trailing azimuthal shock system between Zone I and II at the baseline condition Case 1. Figure 4.5 (a) and (b) shows the instantaneous path-averaged broadband chemiluminescence image and total temperature iso-contours (at 2400 K) in the computational domain visualized geometrically at a 1:1 scale, where the detonation wave is located at a similar azimuth. The 2400 K gas total temperature for isocontour display was selected to visualize the spatial location of chemiluminescence emanating from heat-release and high-temperature product gas, which is preferentially captured by the short time gates of the imaging system. While the instantaneous broadband chemiluminescence is radially averaged, the URANS simulation provides insights into the radial structure of the detonation wave.

Qualitatively, the URANS simulation captures the three main observations in the instantaneous images viz. (a) The wave front is curved in a convex-concave-convex structure along the axial length (b) Zone bifurcation into Zone I and II can be performed in the URANS isocontours where Zone I is observed to have lesser spatial-density of high temperature product gas in URANS – which corresponds to lower luminosity observed in Zone I in the chemiluminescence image while Zone II has a greater spatial density of high-temperature gas which corresponds to higher luminosity observed in Zone II in the chemiluminescence image (c) There is a high temperature gas zone trailing the leading detonation wave in Zone I and is azimuthally separated by lower temperature gas– which corresponds to the ARSC feature that is azimuthally separated from the detonation front in Zone I. Although the local detonation wave shape differs, the CFD is able to capture the global physics of interest and can be used in conjunction with the experimental evidence to further investigate the physics driving three aforementioned physics.

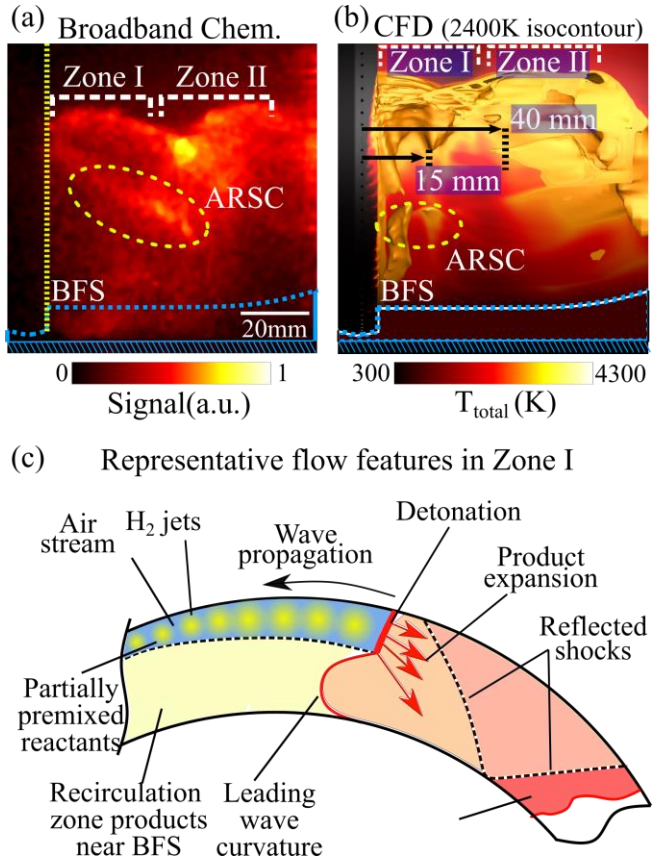

Figure 4.5: (a) Instantaneous broadband chemiluminescence image showing the presence of azimuthal reflected-shock combustion (ARSC) in the wake of Zone I (b) Computational image of 2400 K total-temperature isocontours scaled 1:1 with the chemiluminescence image, also shows the ARSC zone present in the wake of Zone I (c) Schematic representation of the origin of ARSC present in Zone I

To understand the details of the ARSC feature, a schematic representation across the detonation wave in the radial azimuthal plane in Zone I presented in Figure 4.5 (c). In the injection nearfield, due to the injection of hydrogen through discrete fuel injector holes, the reactant gas is expected to have discrete fuel jet streams surrounded by air emanating from the air-injection slot. While shear-layer induced mixing will occur around the fuel-jet, causing partial premixing of reactants, the core of the jet is expected to have pure hydrogen and the area in-between the jets is expected to have pure air in the injection nearfield. Additionally, the radial penetration of reactants in the near the injector is also much smaller in Zone I due to the location of injection system location near the outer radius. This results in the presence of a shear layer between the incoming cold reactants and the product gas trapped in the recirculation zone downstream of the BFS. Due to this

stark difference in temperature, the speed of sound in the injection nearfield has a large gradient in the radial direction with a cold-to-hot gradient existing from the outer radius to the inner radius. Hence, the higher speed of sound in the BFS causes the detonation wave to have a convex leading front as shown in the schematic, occurring primarily from shock induced heating with relatively minimal heat release – due to the expected absence of reactants in the trapped hot-gas. The detonation wave, as shown, passes through the partially premixed reactants in the injection nearfield and causes an azimuthal shock system in its wake due to curvature of the channel in the azimuth. A complex composition of product gas and unburned-vitiated reactants will then expand through the curvature and form wake-shock structures to turn the burned gas. This wake shock structure, is expected to increase the local temperature, increase mixing, and reduce the ignition delay of the unburned reactants that has passed the leading detonation wave. Eventually, these unburned vitiated reactants combust at the shock front trailing the detonation wave giving rise to the ARSC feature. However, the ARSC heat release occurring at the shock front, due to its thin and concentrated heat release zone, appears to be visually similar to a standing-detonation wave trailing the freely propagating leading detonation wave.

Radial-azimuthal wave structure from URANS results

The schematic representation helps conceptualize the formation of ARSC. Since the URANS results also capture this trailing combustion front in Zone I and a lack of such feature in Zone II, two radial-azimuthal contour plots of temperature, pressure and radial velocity (v_{radial}) are extracted from the URANS simulation at ~ 15 mm from the fuel injection plane in Zone I and ~40 mm from the injection plane in Zone II as shown in Figure 4.6 (a) and (b) respectively. These radial slices are extracted to provide finer details on the trailing combustion.

In Zone I, ahead of the detonation wave, a clear temperature gradient along the radial direction is observed (as shown in the detail in Figure 4.6(a)). The low temperature zone (< 300 K) near the outer radius corresponds to the reactant fill depth and the relatively high temperature zone (~ 800 K), radially below the fresh reactants, indicates the presence of hot combustion products from the previous cycle trapped near the BFS. Hence the approaching detonation front is observed to have a convex curvature in the leading edge, due to the higher sonic velocity near the BFS. The leading detonation front is also observed to produce ‘tongues’ in the reactant field indicating combustion of the shear-layer mixed reactants around the hydrogen jet core. The

pressure plots contours show a high-pressure rise across the detonating front near the outer-radius compared to the inner radius, suggesting an overdriven detonation near the outer radius as evidenced in previous studies [76].

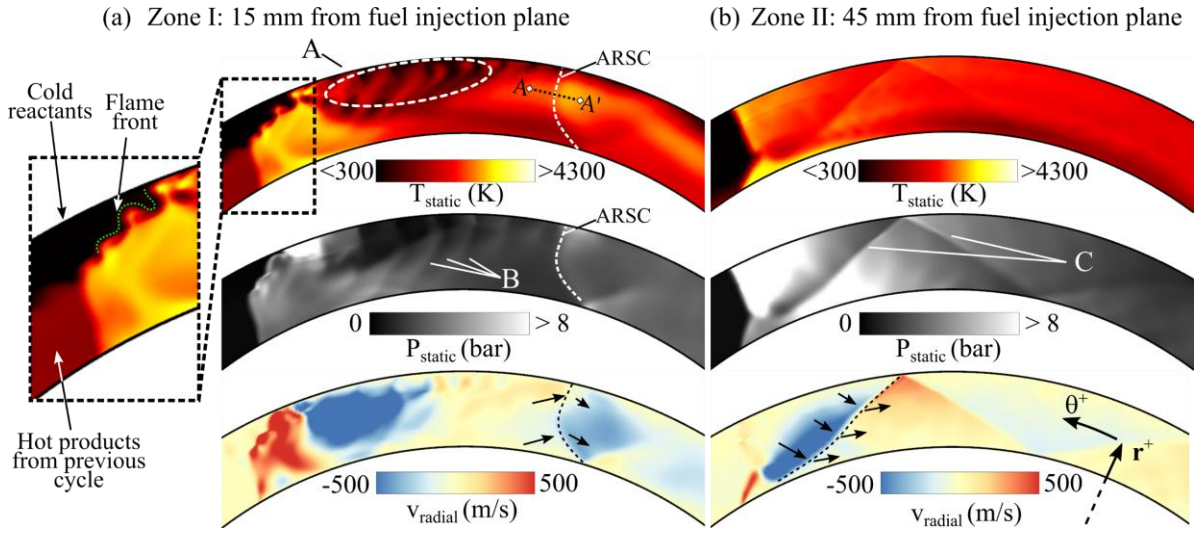

Figure 4.6: URANS radial-azimuthal contours of pressure contours showing the detonation wave details in at two axial locations in Zone I (a) and Zone II (b). A – Unburned reactants that pass the primary detonation wave, B – shock formation due to interaction of detonation product gas and cold hydrogen jets, C – product gas flow-path relative to the leading detonation front D – Azimuthal shocks that help turn the product gas in the annular channel. A-A' is selected across the ARSC zone for further analysis.

Finally, the radial velocity shows the flow turning occurring at these different shock fronts. The complex-product gas, behind the detonation wave, shows evidence of cold zone near the outer-wall (Annotation A in Figure 4.6(a)). Additionally, multiple expansion waves are formed due to the interaction of product gas with the cold reactant jets, as annotated in the pressure plot (Annotation B in Figure 4.6(a)). After this complex interaction, the vitiated unburned reactants combust at the azimuthal reflected shock system – marked ARSC in Figure 4.6(a). The rapid change in radial velocity and increase in pressure indicates the presence of a shock at this location, while a marked increase in total temperature from 2600 K to 3100 K indicates the presence of combustion. Line profiles across the ARSC zone (marked A-A' Figure 4.6 (a)) of total pressure, total temperature and azimuthal velocity (along the θ direction) is shown in Figure 4.7. The spatial separation of the shock front to the combustion zone is less than 2 mm indicating the wave is fully pressure coupled and is detonative in nature [77]. Additionally, a rise in total pressure (~ 2 times)

is observed across this ARSC detonation front – which accelerates the vitiated reactant gas from ~ 400 m/s to ~ 900 m/s. Thus, an increase in total pressure, total temperature, azimuthal acceleration, and extremely small induction length (< 2mm) resulting in close coupling of the shock and combustion wave allows the classification of ARSC as a shock-induced detonation wave. Hence, the pressure gain in Zone I is bifurcated into a leading freely propagating detonation wave and a trailing shock-induced detonation wave. Experimental evidence from simultaneous time-resolved OH* chemiluminescence and OH-PLIF also indicates that ARSC is indeed a shock-induced detonation and will be explored in the following section.

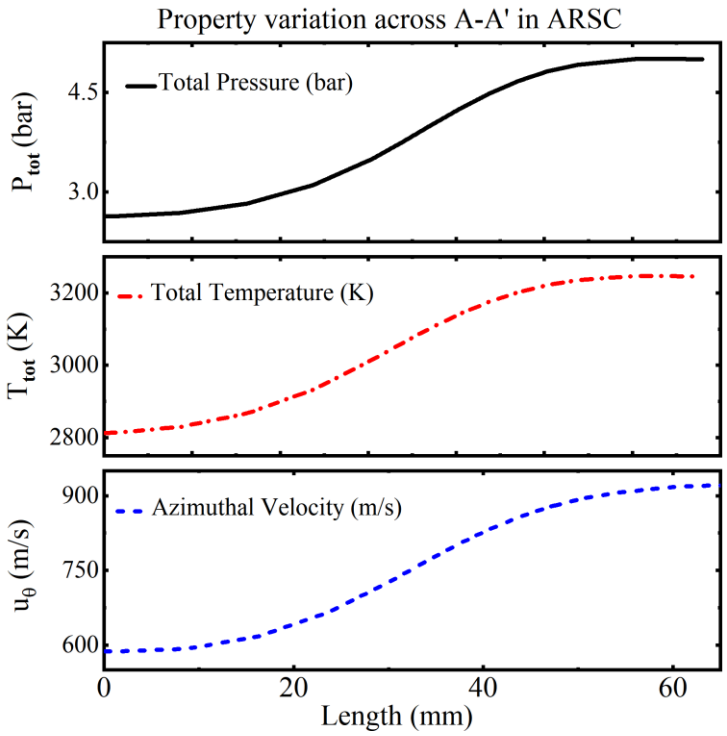

Figure 4.7: Profile of total pressure, total temperature and azimuthal velocity across A-A' in Figure 4.6 (a) from URANS simulations show that the ARSC zone is detonative in nature with heat-release, total pressure rise and rapid acceleration of downstream product gas.

In Zone II, the reactant refill occupies the entire radial depth of the channel. Additionally, due to sufficient displacement from the injection nearfield, the reactant is expected to be well mixed, which results in the observed steep detonation aligned with the radial direction. Behind the leading detonation wave, a trailing azimuthal shock structure is observed as shown by the pressure gradient and the radial velocity gradient in the azimuthal direction. This trailing oblique shock system formation is primarily to (annotation D, Figure 4.6(b)) to assist in flow turning of the

product gas, similar to Zone I, with no observable heat release at the azimuthal reflected shocks, both in the experiments as well as the numerical simulations. This suggests that the reactants are sufficiently well-mixed to be consumed at the leading detonation front with insufficient unburned reactants pass the leading front, resulting in a trailing shock induced detonation wave in the wake of Zone II.

Simultaneous MHz chemiluminescence and OH-PLIF and URANS simulation

To further corroborate the hypothesis of the injection nearfield shock induced combustion, results from simultaneous MHz OH* chemiluminescence/MHz OH-PLIF are compared with the simulations. The OH-PLIF was performed in a radial-axial plane at a given azimuth location for the baseline condition of Case 2, with a camera-exposure of 40 ns to minimize broadband chemiluminescence. Additional details of the experimental setup are provided in Ref. [62]. The detonation wave azimuth positions marked in Figure 4.8 (a) correspond to the notional time at which the corresponding OH-PLIF images in Figure 4.8 (b) were sampled. Similarly, the azimuthal positions marked in Figure 4.8 (c) were the corresponding locations at which the radial-axial temperatures slices were extracted (Figure 4.8 (d)). Scaling of 1:1 was maintained between the experimental OH-PLIF images and numerical temperature contours. The detonation propagation speed in the experiments is ~1640 m/s and in the CFD, it is ~1800 m/s. This difference in wave propagation speed leads to variations in the azimuthal angular separation as discussed in section 0.

At 1 µs, prior to the wave-arrival, Figure 4.8 (b) shows the presence of OH radicals in Zone I near the BFS, close to the inner diameter and after Zone II near the exhaust. The absence of OH signal in the central portion of the channel corresponds to the cold fresh reactants in the combustor channel, as indicated by the bounded region shown in the Figure 4.8 (b). The axial boundary formed between the reactants and the hydroxyl radical near the exhaust shows the assumed reactant height at that instant. The hydroxyl radical near the BFS in Zone I and near the exhaust indicates the presence local high static temperatures – similar to the model prediction as shown in Figure 4.8 (d) at 1 µs. Although the fresh incoming reactants are in contact with the high-temperature product gases, there is no observed contact surface deflagration from the OH-PLIF as well as the temperature field, due to local ignition delay times being an order of magnitude higher than the detonation cycle time.

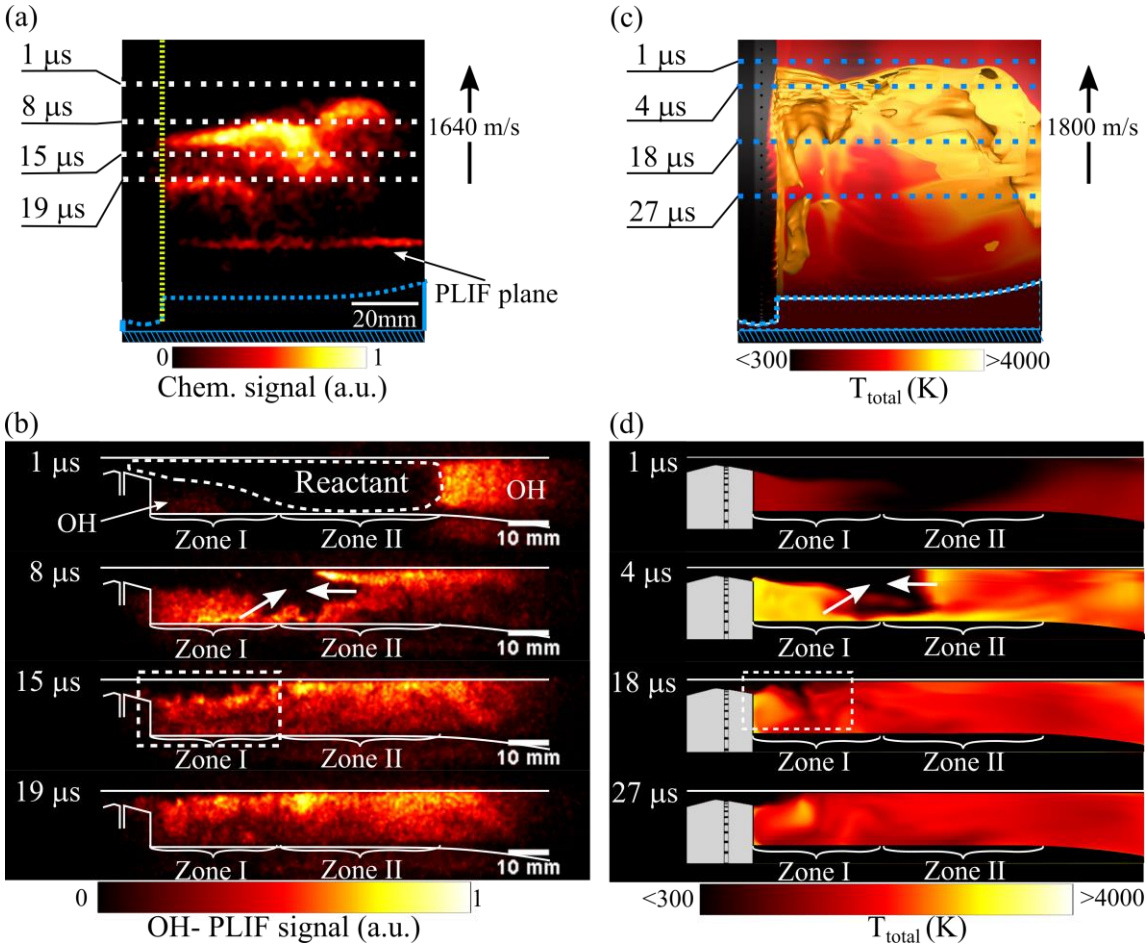

Figure 4.8: Radial-axial OH-PLIF performed at Case 2 test condition. (a) Instantaneous broadband chemiluminescence of detonation wave, showing the approximate azimuthal position of the PLIF plane. (b) Spatial distribution of OH-PLIF signal a during the detonation wave passage event (c) CFD model showing the azimuthal location at which temperature profiles were extracted (d) Spatial distribution of temperature at various azimuthal positions

At 8 µs, the OH-PLIF captures the spatial distribution of OH during the wave passage through the PLIF plane. The arrows marked at 8 µs shows the progression of combustion, as the wave passes through the PLIF plane. In Zone I, the OH signal is observed to propagate axially downstream and radially outward while in Zone II, the OH signal is observed to propagate axially upstream, consuming the reactants present in the mid-axial location. At 4 µs in the numerical model, a similar spatial distribution and progression of the high temperature fronts is observed in Zone I and II, suggesting a good agreement between the experiments and numerical model.

At ~15 µs (Figure 4.8(b)), after the leading detonation wave passage, the entire channel is observed to be filled with OH, except for the injection nearfield in Zone I where a pocket of

unmixed reactants, corresponding to the lack of high-temperature OH radical signal near the outer radius, is observed. The numerical temperature distribution also shows the presence of a cold zone in the injection nearfield at ~18 μs, suggesting that the leading front does not combust the unmixed cold reactants in the injection nearfield in Zone I. This unburned cold-gas pocket, in the radial-azimuthal plane is denoted (Annotation A) in Figure 4.6(a).

After the leading front passes the PLIF plane, the injection nearfield unburned reactants mix and eventually combust at the trailing azimuthal shock system. This event is marked by the observation of OH signal at 19 μs, where previously at 15 μs, there was an absence of OH-signal. Similarly, in the numerical temperature contour, a sharp rise in temperature is observed at 27 μs (Figure 4.8(d)) in the injection nearfield, which was previously (18μs, Figure 4.8(d)) filled with cold reactants in Zone I. Thus, the presence of an Azimuthal Reflected Shock Combustion (ARSC) system trailing the leading detonation wave suggests that the mixture stratified reactant fields present in non-premixed RDCs leads to dual heat release zone that is azimuthally spaced.

To support the argument that the trailing wake is indeed a detonation wave, a closer look is taken at the simultaneous chemiluminescence and PLIF images. The unburned reactants present in the wake of the detonation wave in Zone I is consumed by production of OH near the outer wall within two frames (from 17 μs to 18 μs). This time difference of 1 μs correspond to an azimuthal spread of the trailing wave to be ~ 1.6 mm (1640 m/s × 1 μs), which is much smaller than commonly observed deflagrative wave front. Additionally, 2 MHz OH-PLIF from a prior experiment at the baseline condition, indicates that the unburned reactants are consumed by ARSC within 2 frames (500 ns × 2 × 1640 m/s) providing further evidence of the ARSC flame-front to span an azimuth distance of ~ 1.6 mm [62,71]. Hence the ARSC feature is a quasi-isochoric detonation front.

In conclusion, there are several experimental and numerical observations that provides aid in establishing the ARSC feature as a shock induced detonation wave. The experimental evidences include (1) The OH* chemiluminescence in Zone I and ARSC is on the same order of magnitude at all four test conditions suggesting the heat-release to be concentrated at both combustion fronts (2) The OH-PLIF results show that length of the reaction zone is small (<2mm) suggesting an inherent shock coupling with the azimuthal shock system (3) The heat-release and the corresponding chemiluminescence is concentrated within a 2 mm and the luminosity is comparable to the leading detonation wave suggesting that the trailing wave must be a detonation wave. The

numerical simulations also show that across ARSC feature, the total temperature, total pressure and azimuthal velocity all increase indicating a pressure-gain combustion event. The numerical simulations also indicate that the shock and the heat-release coupling is less than 2 mm, which are all characteristic of a detonation mode of combustion [77]. These conclusions indicate that non-premixed RDC can have both types of detonation waves – freely propagating and steady-flow and further thermodynamic analysis is required to estimate the loss in the expected pressure gain from ideal conditions of purely freely propagating detonations.

4.4.3 Detonation wave characterization using URANS

Prior sections indicate that mixing and reactant stratification plays an important role in the propagation physics of non-premixed RDCs. In this section results from the URANS simulations are used to interpret the reactant field ahead of the detonation wave to provide additional insights on the mixing evolution and local static properties ahead of the reactants. The simulation's qualitative agreement with OH-PLIF and OH* chemiluminescence provides confidence in exploring the underlying physics that develop the complex detonation structure in non-premixed systems. The first section details effect of wave-height plateauing with increasing mass flux while the second section details the effect of mixing, on the axial detonation structure and trailing azimuthal shock system.

An iso-view of local equivalence ratio contours ahead of the detonation at five different axial planes is shown in Figure 4.9 (a). The five axial planes are spaced 10 mm apart with the first plane located 10 mm axially downstream of the fuel-injection holes. Two radial-axial planes are sliced between 5 hydrogen-fuel injector sites, have an azimuthal separation 18°. The radial-axial plane closer to the approaching detonation wave is azimuthally ~ 4° ahead of the detonation wave and shows the local equivalence ratio contour, while the other radial-axial plane (~18° ahead) shows the Mach number contours. Statistical analysis on the mixing efficiency is performed at each radial-azimuthal plane spanning between the five fuel injector holes spaced 18° apart. Probability density function (PDF) of the local equivalence sampled ahead of the detonation wave at all five axial locations are shown in Figure 4.9 (b). Appropriate weighting function is applied to each numerical cell, prior to PDF determination, to minimize biasing effects from varying grid size. To account for detonability limits, a threshold of value of 0.3 and 3 was set for the lower and upper limits of the equivalence ratio, respectively. The detonation cell sizes corresponding to the

threshold values were an order of magnitude higher than the combustor channel width, thus minimizing the feasibility of sustaining stable detonations at that local equivalence ratio in this geometry [78,79].

Wave height dependence on mass flux

The phase averagfed images from Figure 4.4 shows indicates that the observed increase in wave-height starts to plateau with increase in mass flux from Case 1 to Case 4, suggesting a plateauing behavior in the reactant axial penetration depth. To understand the underlying cause for this effect focus is provided on the momentum characteristics of the reactants entering the RDC through the use of Mach number contours shown in Figure 4.9 (a). The Mach number contour shown in Figure 4.9 (a) is located ~ 22° ahead of the detonation wave and have very similar spatial profile to the Mach number contour ahead of the detonation wave allowing the assumption of reactant jet to be fully developed.

The flow exhibits a half-symmetric underexpanded supersonic jet with the air stream reaching supersonic speeds downstream of the throat and the combined air and hydrogen stream downstream of the injector continuing to inject at supersonic conditions into the chamber. The Mach number contours also shows the presence of multiple axial-shock structures indicated as steep gradient in the Mach number along the axial direction. Moving along the axial direction, at ~ 30 mm from the injection plane, the flow's axial velocity reduces due to expected momentum loss mechanisms, including axial shocks, wall boundary and shear layer interactions of the reactant jet with the product gas present in the chamber. This Mach number profile indicates that injection nearfield has lower static quantities compared to the farfield.

The high-speed reactants, ahead of the detonation wave, can be interpreted as an analogous supersonic free jet entering the expanding annular channel. Prior experiments on supersonic free jets have shown that the centerline velocity decay constant remains the same for Reynolds numbers varying by two orders of magnitude (~$1x10^5$ to ~$1x10^7$) [36,37]. Consequently, the penetration depth of the supersonic/subsonic jet plateaus even when the jet mass-flux increases. In this RDC, between Cases 2,3 and 4, the Reynolds number of the supersonic reactant jet is estimated (from URANS and momentum balance) to vary between 1 x 10^6 and 6 x 10^6 which falls within the Reynolds number bounds of the aforementioned experimental results. Thus, transitioning from

Case 2,3 and 4, the reactant penetration depth and the wave height stabilizes albeit with increasing axial momentum.

4.4.4 Reactant mixing field influence on pressure gain combustion.

Reactant mixing field.

The primary phenomena that lead to partial premixing is the turbulence induced shear-layer between the hydrogen jet and the airstream, leading to local equivalence ratio between 0.5 and 2 in the periphery of the hydrogen jet core as shown in the contour plot of local equivalence ratio. This shear-layer mixing is enhanced by secondary mechanism of axial shocks present in the reactant jet flow path. This shock system slows the axial momentum and enables diffusive mixing of hydrogen jet both radially and azimuthally. Transitioning from the 10 mm plane to the 20 mm plane, the probability of upper and lower threshold of equivalence ratio viz. < 0.3 and >3, drops from 85% to 68% and from 9% to 6% respectively; indicating the presence of partial premixing. This partial premixing is enhanced further while transitioning from 20 mm to 30 mm plane, with further drop in the probabilities of the upper and lower threshold equivalence ratio to 60% and 4% respectively. Although the core of either the fuel or air jet cannot support combustion, the partially premixed reactants sandwiched between the jets provide local reactant sites can support the propagation of a combustion wave.

Transitioning from the 30 mm plane to the 40 mm plane, the reactant mixing improves significantly, as the PDF shape transitions from a bimodal distribution weighted at the equivalence ratio extremities to a uniform spread through the entire range of equivalence ratios that support stable detonation wave (Figure 4.9 (b)).

This step increase in mixing can be attributed to the drop in local Mach numbers from supersonic to subsonic state which increases the residence time, promoting diffusive mixing of the reactants. Additionally, the slower reactant jet also expands radially, filling the entire channel width, providing further volume for turbulent and diffusive mixing. The ϕ contour plots also show the rapid increase in mixing between the 30 mm and the 40 mm plane with the reactants fully

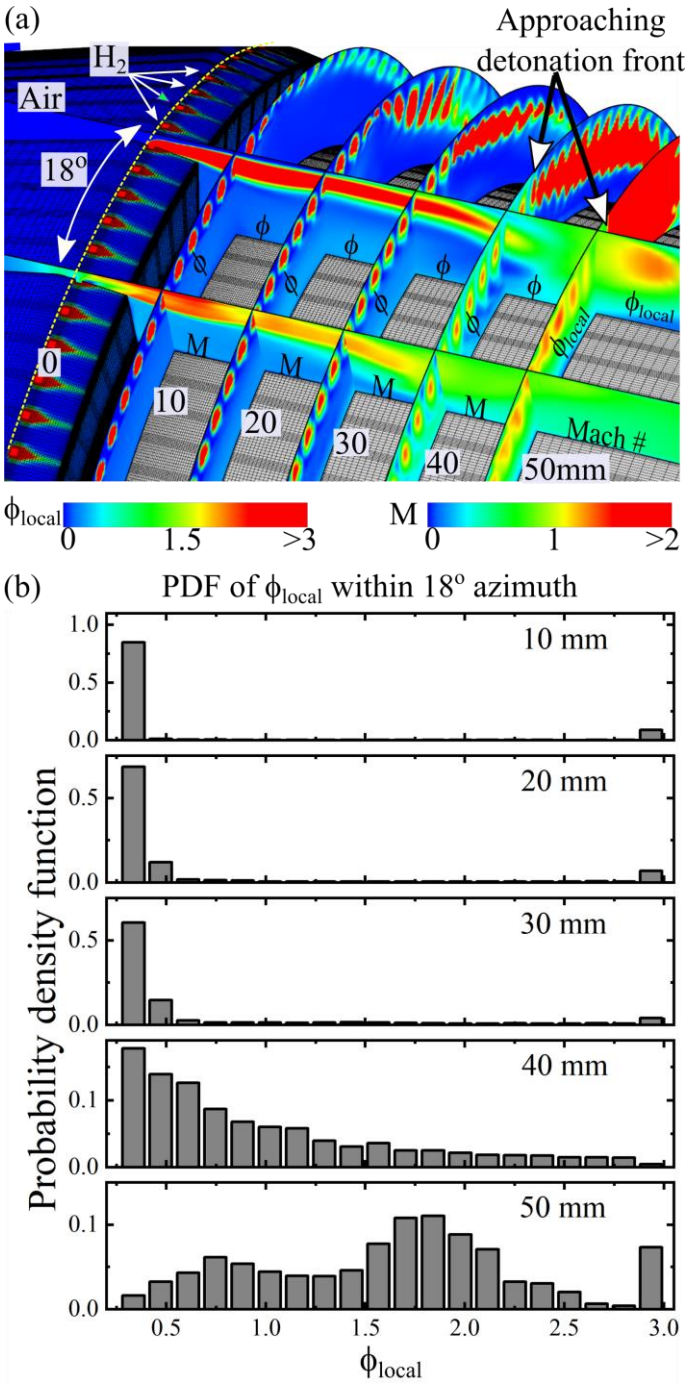

Figure 4.9: Evolution of mixing characteristics from the injection site (a) Radial/azimuthal equivalence ratio contours at five, equally spaced, axial locations ahead of the detonation wave. Two radial axial slices are taken, 15° apart azimuthally, showing the local equivalence ratio and the Mach number at the hydrogen site. Statistical analysis is performed between these two planes separated. (b) Normalized weighted distribution of local equivalence ratio showing the transition from an unmixed (bimodal) distribution to a well-mixed distribution with increasing axial separation from BFS.

occupying the entire channel width of the combustor. At the 50 mm location, the PDF shows the convolution of two gaussian distributions with peaks centered at 0.75 and 1.75. Although the order of magnitude of probabilities in entire range of stable detonable equivalence ratio is similar, the globally fuel rich test condition weights the distribution towards the fuel rich peak.

This stark difference in the mixing efficiency provides confidence in the zone-bifurcations performed in the previous section. The two zones are (1) Zone I, located from the injector to ~30 mm axially downstream, contains mostly unmixed, very fast-moving fluid with low static quantities and is limited to a radial fill of 4–5 mm from the outer diameter of the annulus (2) Zone II, located from ~30 mm to ~65 mm downstream of the BFS, contains relatively well-mixed reactants, slow- moving fluid with higher static quantities, that fill the entire 10.7 mm radial depth of the annulus. Additionally, the leading freely propagating detonation wave passes through the unmixed reactants in the injection nearfield through consumption of partial premixed reactants, and sufficient unburned reactants are accelerated azimuthally, where shock induced detonation trailing the leading wave (ARSC) consumes these unburned reactants.

Influence of mixture stratification on pressure gain performance

The implication of such zone bifurcations is extremely important in designing non-premixed RDCs. The formation of shock induced detonations in the wake indicate that, for non-premixed RDCs, although complete combustion of reactants does not occur in the leading freely propagating detonation wave, a trailing shock induced detonation provides an avenue for the vitiated unburned reactants to burn in an isochoric fashion. While this isochoric vitiated heat release is desirable from a thermodynamic standpoint, where the injected reactants aren't expelled out without combusting, there is a performance loss from theoretical pressure gain that is expected from detonative combustion.

For a nearly stoichiometric, well mixed hydrogen-air quiescent reactant, the total pressure ratio across the detonation is expected to be ~ 15. In Zone I, from the URANS simulation results, the pressure ratio across the leading front is only ~ 4.5. Whereas in Zone II, the pressure ratio across the detonation is ~ 12. The pressure ratio of 1.8 in ARSC is lower than the leading front, due to the reactant having an azimuthal approach velocity induced by the leading detonation in Zone I, which is a departure from freely propagating C-J detonations. Combining the 1.8 pressure ratio across the trailing ARSC, the total pressure ratio across the Zone I detonation amounts to ~

8.1, while in Zone II the total pressure gain is ~ 12. Albeit having a relatively simple reaction mechanism, the model highlights a stark difference in the pressure gain which is influenced by the mixing field and warrants further exploration of the thermodynamic loss associated with a shock-induced detonation. While this study provides experimental evidence of freely propagating and shock-induced detonations, further quantitative evaluations must be necessarily addressed to understand the practical of overall pressure gain that can be expected from RDCs.

4.5 Conclusion

MHz rate broadband chemiluminescence, simultaneous OH* and OH-PLIF imaging with complementary URANS simulation was performed for studying the highly dynamic detonation structure formed in non-premixed hydrogen-air rotating detonation combustors. The time-resolved measurements highlight the complicated shock and flame front interactions that occur in the detonation structure in non-premixed RDCs. The detonation structure has varying properties along the axial length of the combustor forming weaker portions of the detonation near the injection zone (Zone I) and stronger portions of the detonation wave downstream (Zone II) caused by fuel stratification. This axial variation in the two zones scales in the stream-wise direction with increasing mass flux. The detonation front curvature is dictated by local temperature ahead of the detonation wave, leading to a convex-concave-convex shape due to high temperature zones present near the BFS and at the exhaust. In the injection nearfield in Zone I, although the local equivalence ratio of reactants far exceeds the detonability limits, the detonation wave is observed to propagate. This detonation front propagation is supported through combustion of partially premixed reactants present in the shear layer of the fuel and air streams. In Zone II, the reactants are observed to be well mixed ahead of the detonation wave primarily span the equivalence ratio space within detonability limits. This leads to a detonation front in Zone II to have a higher luminosity compared to Zone I.

In addition to the axial detonation structure variation, a variety of shock interactions are observed in the wake of these detonation waves because of the annular geometry of the RDC. The injection nearfield, Zone I has a leading freely propagating detonation front followed by a trailing shock-induced detonation front called ARSC. In the injection farfield however, due to the relatively better mixed reactant field ahead of the detonation wave, the leading freely-propagating detonation front consumes the reactants and no-wake detonation structures are observed. The

length of the ARSC zone proportionally increase with the axial reactant unmixedness and static quantities. This ARSC system suggests a combination of freely propagating detonation and shock-induced detonations are present in non-premixed RDCs in the injection nearfield, which deviates from theoretical pressure gain expected from quasi-isochoric heat release occurring in detonations.

5. TRANSVERSE WAVES AND CELLULAR PROPAGATION IN NON-PREMIXED RDCS

5.1 Introduction

Rotating detonation engines are desirable for their ability to sustain pressure gain combustion in continuous flow devices, which promises to increase thermodynamic efficiency with the same fuel-oxidizer combinations as conventional constant pressure combustion devices [4,27]. The last two decades have seen extensive research and development of these systems from laboratory-scale engines to practical applications [2,4,13,14,29,35,59,80,81]. However, achieving theoretical pressure gain remains a challenge due to the trade-off between mixing efficiency and pressure recovery leading to incomplete combustion and non-ideal flow losses, respectively. A way into understanding these loss mechanisms involves focused study on the detonation reaction front produced by non-ideal stratified fuel/oxidizer mixture.

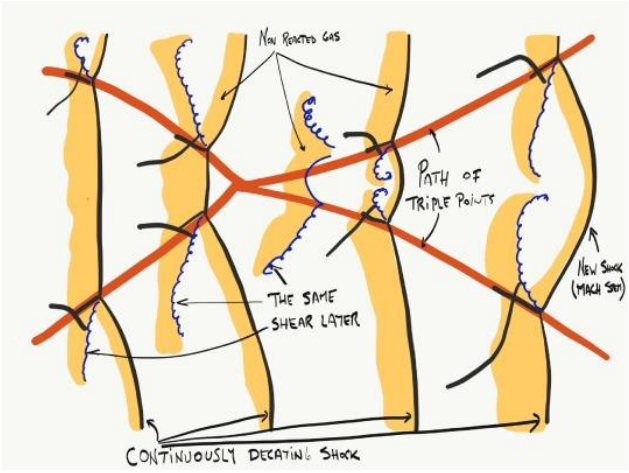

Figure 5.1: Formation of cellular structure in detonations propagating in a premixed straight channel [82]

One such metric is the cell-size of detonation waves and their sensitivity to the mixture composition and thermodynamic state. The cellar pattern is produced by the trajectory of the triple-point, a highly three-dimensional structure consisting of an intense heat release zone. The triple point is formed at the intersection of the Mach stem, incident shock and transverse-wave. The incident shock and Mach stem are aligned perpendicular to the direction of propagation with alternating incident shock and Mach stem sections while the transverse wave is oriented along the

direction of propagation. The intersection points of these systems, alternatively move towards and away from each other in direction perpendicular to wave propagation, leading to the trajectory formation of cellular pattern, as shown by Radulescu [82] in Figure 5.1. These cell sizes are captured on a soot foil from detonations propagating in a linear detonation channel lined with a soot-foil and primed with premixed fuel and oxidizer combination at various pressures and temperatures (initial condition). The large density gradients and thermal load at the triple-point locations leave a streak mark along the soot foil during the propagation. These soot foils are recovered at the end of the test and are assessed to provide a cell-size for the reactant composition, pressure, and temperature.

Such measurements provide valuable information on the cell size of a reactive mixture at various conditions and can be used only for well mixed premixtures and is typically a single-shot experiment. In the case of an RDC however, there are two significant challenges posed in using soot-foil to measure the detonation cell size (i) The continuous propagation of detonations will interact multiple times with the soot foil which will completely remove any soot trace from the first detonation cycle (ii) The cell sizes produced will be dependent on local stratification, thereby producing different cell sizes across the detonation channel. An alternative approach is to use an open-shutter camera or a high repetition rate framing camera. The former approach will be a challenging due to minimal control of the light entering the camera chip, which can either damage the camera sensor due to overexposure, or not have sufficient luminosity from chemiluminescence to have good SNR to track the cellular structure. The latter approach, with the advancement of high-repetition rate camera and intensifier technology, can be used to provide information on the detonation cell size in non-premixed RDCs.

To address the aforementioned challenge, and to understand the cellular propagation of detonations in RDCs, a MHz rate chemiluminescence system comprising of a high-speed camera capable of framing up to 10 MHz and a high-speed intensifier capable of repetition rates of up to 2 MHz was used to study the detonation propagation in a non-premixed optically accessible hydrogen-air RDC [60,83]. To accomplish the visualization two different approaches were entailed (i) Maximum intensity projection (ii) Sum-of-correlation particle image velocimetry. These two techniques reveal a non-uniform cellular propagation physics in stratified fuel air mixtures in non-premixed RDCs.

5.2 Experimental Setup

Figure 5.2 (a) displays a schematic of the optically accessible RDC, with the quartz outer body having an inner diameter of 136 mm. High pressure air enters from a plenum through a converging-diverging section with a throat gap of 1.45 mm. Fuel is injected radially through 100 equally spaced slots in the diverging section (10^o expansion angle) downstream of the throat normal to the air stream. The fuel slots are milled with a 0.4 mm diameter to a depth of 0.6 mm and are located at an area ratio $\varepsilon = 1.16$. The flow channel expands through a backward facing step (BFS) from an expansion section at $\varepsilon = 1.8$ leading into the combustor channel ($\varepsilon = 7$). Additional details of this geometry are provided in prior work [51] and the supplemental material attached. The hydrogen and air mass flows are metered using choked sonic nozzles. The dry air flow rate is set to 0.22 kg/s and 0.45 kg/s to reach a throat mass flux of G_{air} = 350 kg/m^2/s (Case 2) or 750 kg/m^2/s (Case 1), respectively, at a global equivalence ratio, Φ_{global}, of 1.05. The uncertainty in mass flow rate is computed to be ~2 %. Pressure transducers (UNIK 5000) and thermocouples were used for monitoring the pressure and temperature in the air and fuel manifolds with an uncertainty of ±1 psia and 0.1 K, respectively.

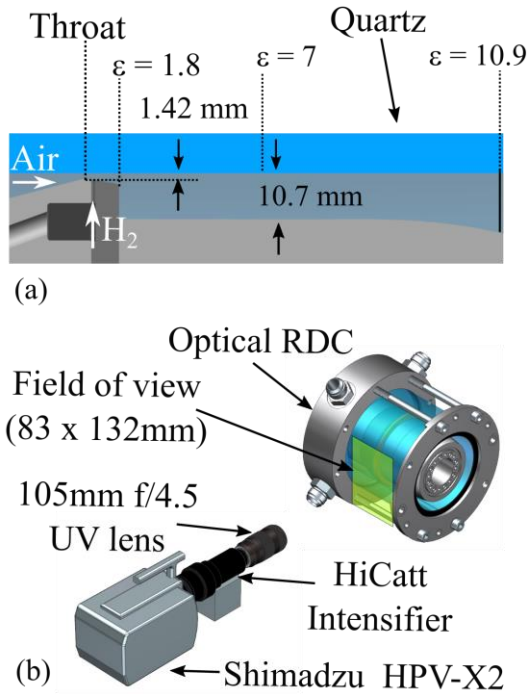

Figure 5.2: (a) Cross-section view of flow path and (b) and experimental arrangement.

The imaging system arrangement is shown in Figure 5.2 (b). The imaging system utilizes a Shimadzu HPV-X2 camera capable of capturing images at speeds up to 10 MHz at a full resolution of 250 x 400 pixels with a maximum of 256 frames at any frame rate. The HPV-X2 camera is coupled to an image intensifier (Lambert Instruments, HiCatt 2), capable of operating at speeds of 1 MHz and an exposure time of 40 ns. A 105 mm, $f/4.5$ camera lens with a transmission spectrum ranging from UV to visible wavelengths is used with the imaging system. This optical setup allows for imaging of broadband chemiluminescence imaging, with a spectral bandwidth of 280–800 nm, including OH* (280 – 320 nm) , radicals in hydrogen-air combustion (320–500 nm), and the visible to near-infrared region of water vapor emission (600 nm – 10 μm) [32].

The camera is focused on the RDC annulus to visualize the wave traveling through a circumferential range of nearly 180º, with a field of view (FOV) starting 10 mm upstream of the air-injection throat. The images presented have been cropped to visualize a FOV of 83 mm x 83 mm. A smaller FOV of 35 mm x 55 mm, focused near the injection plane, is used for higher resolution imaging of the detonation near the BFS. The camera is triggered 400 ms after RDC ignition to capture the detonation wave propagation at steady state. The intensifier time gate is set to 100 ns to reduce motion blur, giving a detonation wave displacement of less than 1 pixel for the large FOV and ~2 px for the small FOV.

5.3 Results

The results are organized into two sections. The first section uses maximum intensity projection (MIP) to show the detonation wave structure in the macro-scale, involving a field of view across the entire length of the RDC. The second section uses MIP to track the detonation propagation in the injection nearfield and sum-of-correlations using PIV is used to visualize the detonation propagation and cellular patter formation in non-premixed RDCs.

5.3.1 Maximum intensity projection results

Macro cellular structure

The injection system plays a critical role in the location and structure of the detonation wave. Two consecutive cycles of detonation wave propagation for test cases 1 and 2 are obtained at 500 kHz with a 100 ns exposure time, presented in Figure 5.3, are the result of an ensemble sum of the

maximum intensity obtained for each frame during the wave propagation. This allows the notional view of an open shutter image of ~30 us. These images show the dynamic nature of the detonation wave over time and illustrate the coupled behavior of detonation position and injection system. At high air-mass flux, the stronger detonation zone is displaced further away from the BFS (green line). The injection recovery process initiated behind the weak detonation is affected when the products of the strong detonation travel axially upstream and reaches the BFS. This transverse wave reflects off of the BFS generating a suction effect on the injection system, eventually affecting the injection fill height causing a cyclic change in refill height, a memory effect from one detonation cycle to the next. Thus, a memory effect from the current azimuthal location of detonation wave affects the axial position and shape of the next detonation wave at the same azimuthal location for this relatively high axial speed non-premixed injection system. At lower air mass flux, the location of the detonation wave is unaffected by this cyclic behavior since the product gas interactions have a temporally short response time and reaches the BFS before the initial injection recovery begins. Additionally, the injection pressure is lower, resulting in lower injection speeds and a detonation wave location closer to the BFS. Hence, the injection recovery process is repeatable over multiple detonation cycles with minimal coupling to the detonation position. Overall, increasing air mass flux corresponds to an increased total pressure ratio over the injection and back plane and an increased wave coupling with the injection manifold. While the cell sizes in this region is on the order of ~24 – 25 mm, which is 2 times higher than the predicted hydrogen air detonation cell size for a global equivalence ratio of 1.0, the local equivalence ratio fluctuations along with the transverse wave propagation direction induced by ‘longitudinal’ produce cells of macro-scale.

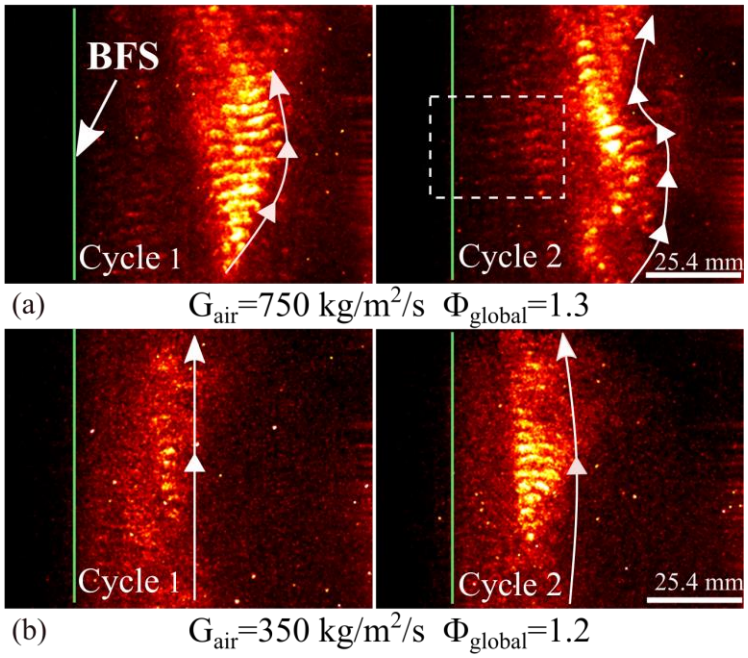

Figure 5.3: 500 kHz Ensemble sum of the maximum intensity of chemiluminescence of the detonation wave position and structure at different mass fluxes for two consecutive cycles of detonation wave travel.

Cellular propagation at the injection nearfield.

We proposed and experimentally showed that the detonation wave structure along the channel axial length is strongly influenced by the mixing field, which itself is radially and axially stratified in Section 3. Closer to the injector, the equivalence ratios are far from stoichiometric with fuel rich regions near the fuel jet trajectory and fuel lean regions in the BFS recirculation zone. Axially downstream, the mixture approaches a more homogeneous stoichiometric fuel-air mixture where chemiluminescence imaging shows a more robust combustion wave front. Propagating detonation waves of non-premixed reactants have a distorted cellular propagation due to decoupling of the combustion-shock complex from associated heat loss [64,84] from the combustion wave. Recent measurements show a nonuniform and complex cellular pattern in a non-premixed RDE [60]. Cell size information in RDEs is important because it is a useful engineering parameter for RDE scaling, and it is also useful for providing insight into the flow field and combustion dynamics.

To visualize the cellular propagation of detonations in this non-premixed RDC, higher resolution spatial imaging using 1 MHz broadband chemiluminescence imaging near Zone 1 was performed for Case 1. First, a non-linear spatial filter was applied to minimize the background

noise. An optical cellular image was created by producing an image of the maximum intensity from each pixels time history, shown in Figure 7. This highlights the motions of the highest intensity portions of the propagating detonation wave front and is one of the first experimental confirmations of cellular structure in non-premixed RDCs.

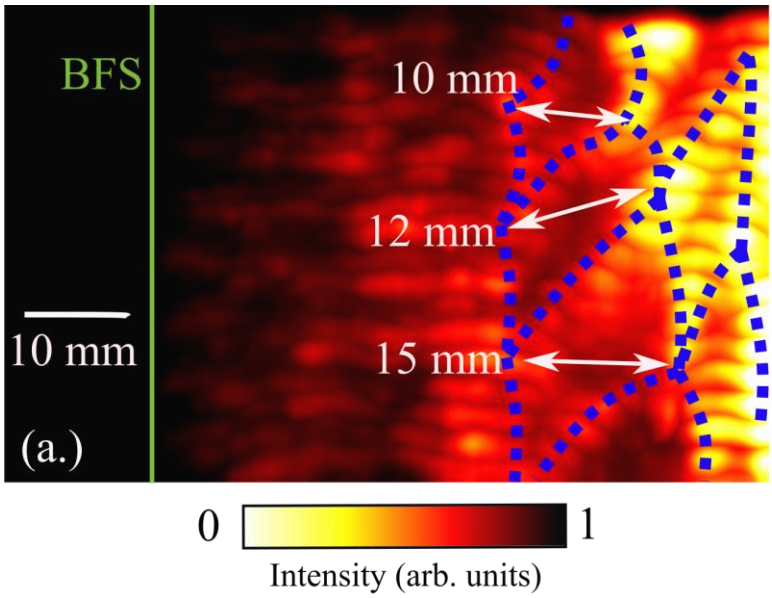

Figure 5.4: Dotted blue lines showing the cellular propagation of detonation waves observed in non-premixed RDCs.

Clearer cellular structure is observed in Figure 5.4 axially downstream of the injection face approaching Zone II where the well mixed reactants allow enable combustion wave to propagate more robustly. Near the injection face, however, due to poor mixing, the propagation is not as well defined, and the combustion displays lower luminosity and is more spatially distributed. This supports the theory that a certain mixing length is required in order to sustain robust detonation wave propagation in the RDC. Also, considering the cell sizes obtained by measuring the cellular pattern widths, the cellular sizes vary primarily between 10–15 mm, which is close to the ideal 8 mm size for a stoichiometric premixed hydrogen-air detonation at 300 K and 1 atm in a linear channel [79]. Differences can be attributed to the mixing and fuel stratification, curvature, and shock structure interactions specific to the geometry and operating conditions of the RDC [32].

5.3.2 Sum of correlation PIV

Propagating detonation waves of non-premixed RDCs have a distorted cellular propagation of the leading detonation front [64,84]. Soot foil measurements to determine the cell size are typically performed on thin detonation channels with premixed fuel and oxidizer [85]. A larger channel gap leads to the cellular pattern expanding transverse to the direction of propagation, allowing for a three-dimensional cellular structure propagation. In this non-premixed RDC, the weak detonation wave close to the BFS has a fill depth of ~3–5 mm. Hence, the detonation wave tends to behave like a canonical detonation wave observed in linear detonation channels. To visualize the cell structure in non-premixed RDCs, the FOV marked in cycle 2 of the G = 750 kg/m^2/s test case (Figure 5.3) was selected, and 1 MHz broadband chemiluminescence imaging, for test case 1, was performed. With a non-linear spatial filter, the chemiluminescence noise was minimized. Figure 5.5 Figure 5.5(a) shows the resultant ensemble maximum intensity sum. The motion of the chemiluminescence was tracked with a commercial PIV code (LaVision DaVIS 10), and an

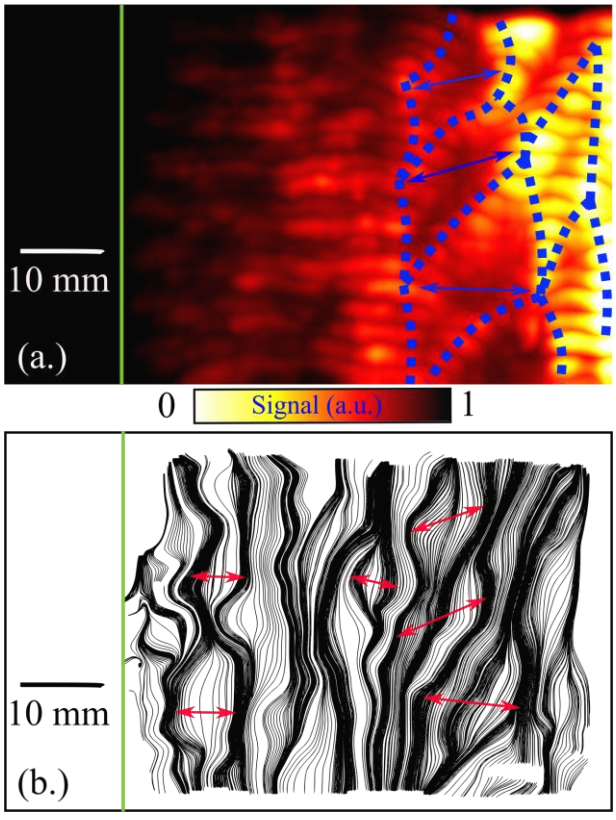

Figure 5.5: Cellular structure of detonation waves observed in non-premixed rotating detonations. From PIV sum of correlation results

ensemble correlation analysis was performed to obtain the motion of chemiluminescence over time [86]. The transverse motion of the chemiluminescence shows experimental observations of cellular structure in RDCs, with the areas inside the boundary of the cell widths marked in Figure 5.5 (b) showing relatively lower chemiluminescence (Figure 5.5 (a)) as opposed to the boundary. This suggests the high luminosity locations mark the triple point locations along the propagating detonation wave. The cell size is obtained by measuring the width of the nodes of transverse motion and is found to be on the order of 7 – 12 mm. The mean cell size of 9.5 mm is close to the experimental soot foil cell size measurement of 8 mm for a stoichiometric hydrogen-air detonation at 300 K and 1 atm [79]. However, differences in the mixing and fuel stratification together with additional shock structures caused by the coupling of the outlet plane and injection system are possible reasons for variations in the cellular structure, in comparison to premixed canonical detonations.

5.4 Conclusions

The combined use of a new imaging system and optically accessible hydrogen-air RDC, Cellular structures in non-premixed RDCs are visualized. The fuel stratification in non-premixed system gives rise to cellular formations in macro as well as micro scale, having cell widths twice as much as experimental evidence from prior work suggests. The macro scale cellular propagation is influenced by the longitudinal mode changes, while the microscale cellular structures are inherently coupled to the wave propagation physics. With increasing axial distance from the injection plane, the fuel air mixing efficiency improves giving rise to a monotonic increase in the cellular size from the injection nearfield.

6. DETONATION STRUCTURE INVESTIGATIONS IN STRAIGHT AND EXPANDING ANNULAR COMBUSTORS

Rotating detonation engine (RDE) have periodic transient interactions of the fuel/oxidizer injector with the propagating detonation waves in the annulus. Understanding this interaction plays a critical role in the ability to realize pressure gain from practical RDEs. In this work, the wave response, and dynamic characteristics of two unique injectors are explore in an optically accessible jet in supersonic crossflow injection based H_2-Air RDC. In the first configuration, the injector passage terminates at a backward facing step (BFS) leading into the combustion chamber while in the second configuration, downstream of the fuel injectors, has a gradually expanding 10° ramp. This geometric ramp design eliminates the presence of a large recirculation zone downstream of the injection system, which can minimize shear layer induced pressure losses in the BFS design. Combining the use of MHz rate OH* chemiluminescence, MHz rate OH-PLIF and URANS simulations, this work highlights the primary differences in the wave shape, the dynamic response of the detonation wave and the influence of injector geometry on the recovery process of the detonation wave.

6.1 Introduction

Rotating detonation combustors, in which a rotating shock is continuously burning the reactants, can theoretically lead to increased gas turbine cycle efficiencies from operating in a valveless constant volume combustion. Over the past decade, substantial research has been performed to understand the flow physics within rotating detonation combustors over a wide range of operating conditions for premixed as well as non-premixed systems, both numerically and experimentally. The detonation wave moves at velocities on the order of ~1500–1700 m/s, with an impulse change in the scalar quantities across the detonation wave front. In addition to having large wave speeds, high velocities, and complex interactions with the wall confinement lead to shock train formation in the wake of the RDC as well as shock induced combustion in non-premixed systems. Detonation waves interact and influence the injection system as well, leading to cycle-to-cycle variability in the wave behavior.

The Turbine Integrated High Pressure Optical RDC (THOR) is constructed with axial air injection and radial hydrogen injection scheme with optical access extends from the air-plenum through the exit of the combustor. The primary reasons for building this test platform are (a) Design and develop diagnostic tools to study the physics of detonations in annular channels (b) Understand the driving physics involved in propagation of spinning detonation waves. Several seminal experimental works have been carried out in this effort. To aid the in understanding the experimental measurements, Unsteady Reynolds Averaged Navier-Stokes (URANS) simulation of the full 3D geometry of the RDC is modelled. The URANS simulation captures the mixing process and boundary layer effects of the geometry with near wall mesh refinement. Results from the URANS simulations are complemented with the experimental observation to improve the confidence on the measurements and the physics described in this work. In this work, two different injector configurations are studied with MHz rate OH* Chemiluminescence, MHz rate OH-planar laser induced fluorescence (OH-PLIF) and URANS simulations.

6.2 Experimental Setup

6.2.1 Brief description RDC geometry

A cross section of the flow path with backward facing step (BFS) and ramp inner body is shown in Figure 6.1 (a) and (b) respectively. The outer diameter of the test section is 135 mm and the length of the combustion chamber section downstream of the backward-facing step (BFS) is ~90mm (Configuration 1). The combustor annular gap is 10.7 mm, comparable to other studies done for this class of RDC [24,26,30].

Air is delivered from a plenum and is choked through a through a converging diverging section at a throat gap of 1.45 mm. The diverging section has an expansion angle of 10 degrees. From the throat location, the channel is expanded at a constant rate until reaching an A/A* = 1.15 where hydrogen is injected through individual holes in a jet in cross flow arrangement. A 10 mm deep plenum pocket feeds 100 milled slots of diameter 0.4 mm and depth 0.6 mm formed between the copper fuel injection plate and the air-throat contraction body as shown in Figure 6.1. Following this flat section where fuel is injected, expansion is continued until an A/A* = 1.8 is achieved and the flow is subjected to a backward facing step leading into the combustor annular

gap of 10.7 mm. Downstream of the combustor section, the geometry is expanded further from A/A* = 7 to A/A* = 10 for downstream component integration, not a part of this work.

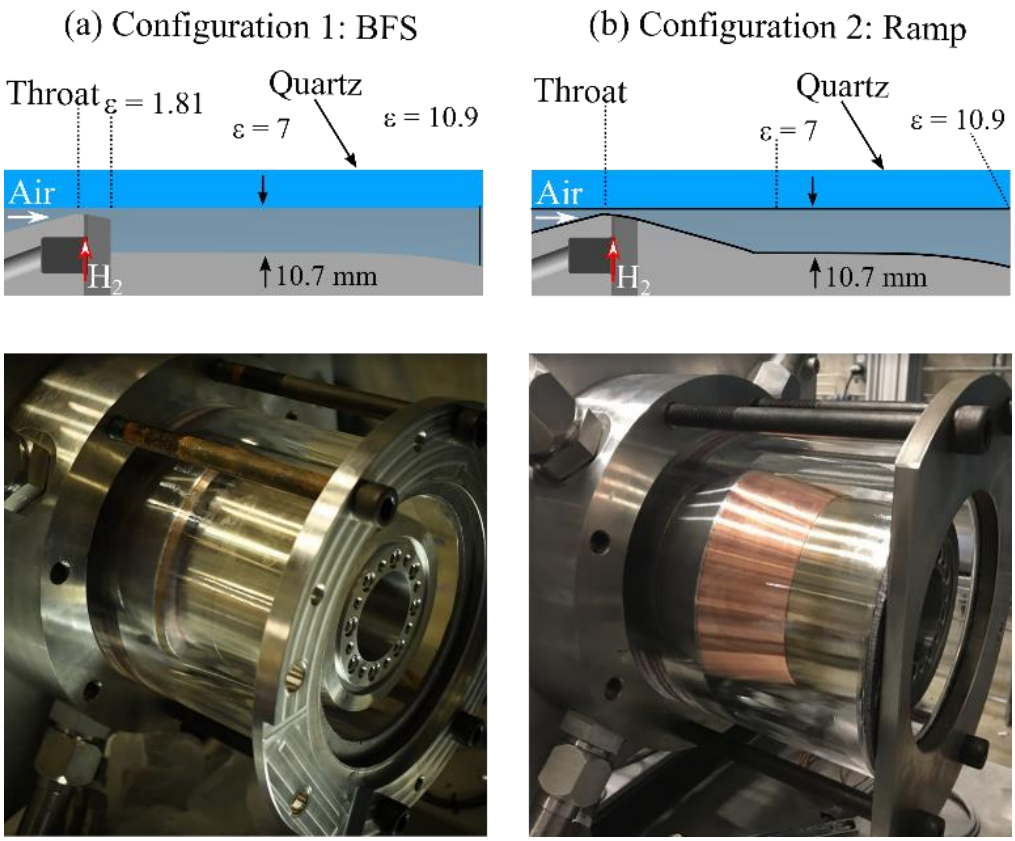

Figure 6.1: Cross section and image of the optical RDC for (a) BFS design and (b) Ramp Injector

For the case of the Ramp injector (Configuration 2), the cross section shows that the fuel ring is extended as a 10° ramp that leads into the combustor A/A* of 7. This configuration eliminates the recirculation zone that is present downstream of the BFS which prevents the trapping of product gas from the previous cycle in the BFS recirculation zone.

6.2.2 MHz OH-Chemiluminescence experimental setup

To capture the detonation evolution, CMOS cameras and two-stage intensifier are used to capture OH* chemiluminescence in the RDC with a 105 mm f/4.5 UV lens. For repetition rates up to 100 kHz, a Phantom v2012 is coupled to a HiCatt intensifier. For higher repetition rates, the HiCatt Intensifier is coupled to the Shimadzu HPV-X2 camera, as shown in Figure 6.2. The Shimadzu camera can capture images at repetition rates up to 10 MHz at full frame (250 x 400 pixels), while

the intensifier is limited to 1 MHz. A protective steel barrier is used to protect the camera system in case of quartz failure. At all test conditions, the intensifier gate is set to 200 ns in order to prevent blurring effects from detonation wave motion during the exposure. During this exposure it is estimated that the detonation wave would have moved less than 0.5 mm.

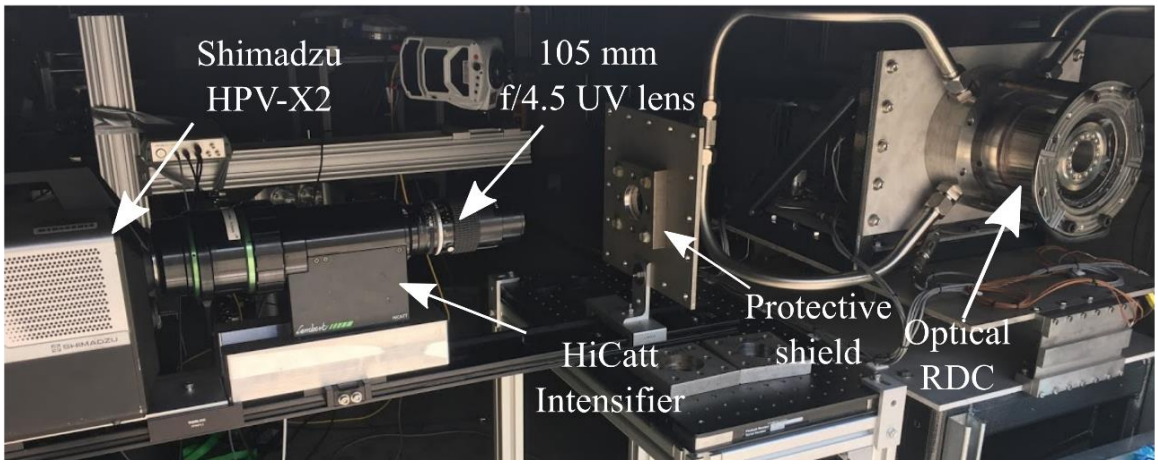

Figure 6.2: Diagnostics setup for capturing kHz and MHz rate images.

6.2.3 MHz OH-PLIF experimental setup

A detailed description of the MHz-rate OH-PLIF diagnostic setup can be found in Hsu, et al [62,71]. A brief outline is provided here. A schematic of the MHz-rate burst-mode OPO is shown in Fig. 2. The overall diagnostic arrangement consists of a burst-mode laser, optical parametric oscillator (OPO), high-speed camera, intensifier, and RDE. The fundamental beam from the burst-mode laser (Spectral Energies, QuasiModo) was frequency tripled to produce pulses of approximately 40 mJ and 5 ns at 355 nm. The burst-mode laser also generated the second-harmonic 532-nm output, ~20 mJ/pulse, for use in sum-frequency mixing (SFM) with the output of the OPO down to 284 nm. For 2 MHz operation, the conversion efficiency was improved by changing the pulse temporal profile from gaussian to square and reducing the laser pulse width to 2.6 ns. The OPO consisted of a Type-I beta-barium-borate (BBO) crystal that was cut at an angle of 32° to the optical axis. After the OPO cavity, the output OPO signal was sum-frequency mixed with the residual 532-nm beam from the burst-mode laser in a BBO crystal which produced ~400 μJ/pulse and ~ 200 μJ/pulse of narrow-linewidth 284 nm UV radiation at 1 MHz and 2 MHz repetition rate, respectively.

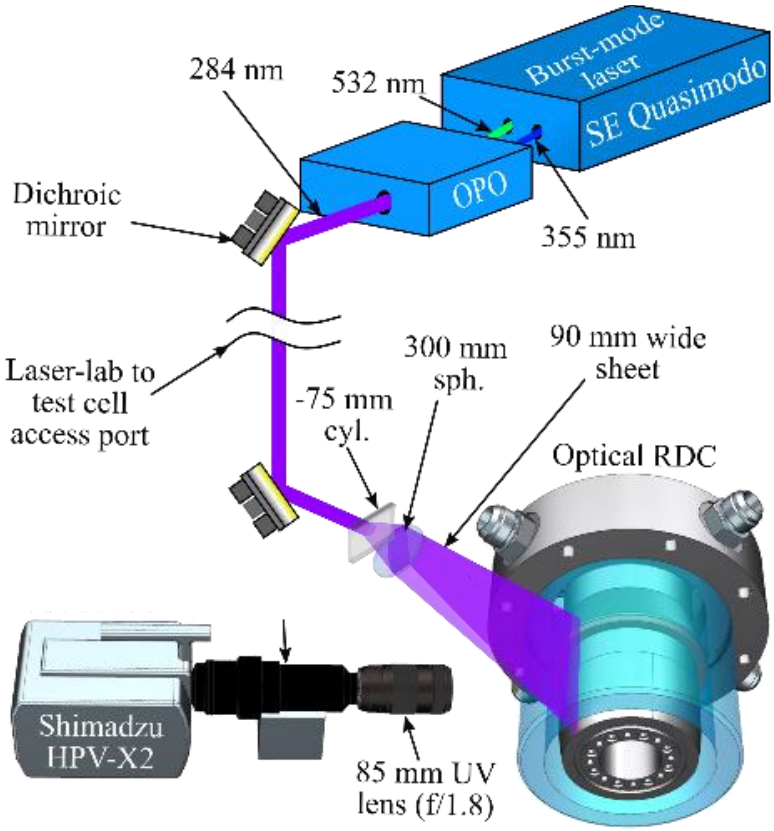

Figure 6.3: Diagnostics setup for capturing MHz OH-PLIF images.

6.2.4 URANS simulations

Unsteady Reynolds Averaged Navier Stokes were performed for the RDC using the CFD++ (Metacomp [72]) flow solver. The numerical domain is shown in Figure 6.4(a) which extends from the inlet plenum, to exhaust of the RDC. It consist of the air-inlet plenum, 100 discrete fuel injection holes, the air injection throat, BFS and the combustor annulus. A structured grid was constructed using ICEM to provide a total of ~ 48.5 x 10^6 cells with boundary layer mesh refinement (as shown in Figure 6.4).

The maximum non-dimensional distance, y+, was 14 and was within the detonation front on the out diameter of the annulus, while y+ on the inner diameter of the annulus was below 1. The 3D simulations were performed with a k-ω SST model to for improved simulation accuracy at the near-wall region and in free-shear layer flows. A single-step chemistry reaction was to simulate the hydrogen-air reactions, a method used in prior RDC simulations by Frolov et. al [74]. The numerical boundary conditions at the inlet plenum of air and fuel were supplied from static pressure measurements obtained for Case 1 from the experiments with a total pressure of 5 bar and

290K for the air inlet and 5.3 bar and 290 K for the hydrogen inlet. The exit boundary condition was set to 1 bar resulting in a mixed supersonic/subsonic boundary condition at the exhaust. The initial simulations were performed with a coarse grid for ~30 cycles and then boundary layer mesh refinements were imposed. Adiabatic non-slip wall conditions were applied for the wall boundaries.

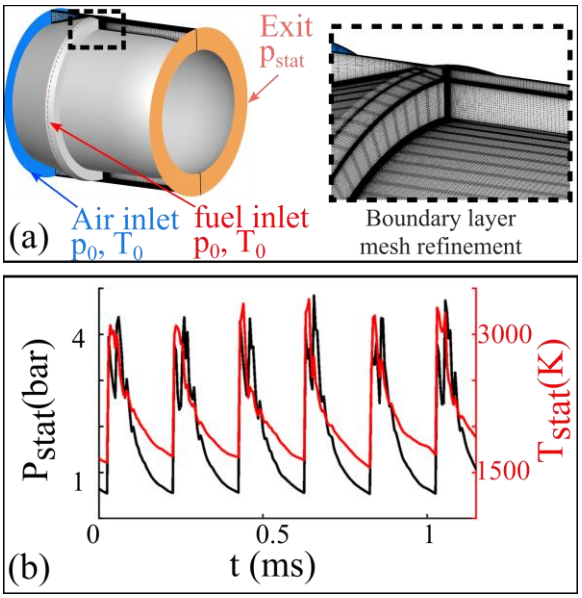

Figure 6.4: (a) Numerical domain of URANS simulation highlighting the boundary condition specified. A close vide of the boundary layer mesh refinement is shown in the inset – focused on the injection system. (b) Shows the pressure and temperature variation at a point 25 mm downstream of the BFS during the limit cycle behavior of the URANS simulation post detonation initiation.

The computational model was run on 120 high-performance computing (HPC) cores and the simulations results were from a snapshot ~30 cycles after reaching limit cycle on the fine boundary mesh. The pressure and temperature plot shown in Figure 6.4 (b) was sampled at a 5 μs time interval located ~1 mm downstream of the BFS and mid-annular radius of 5.9 mm. Additional details of the simulations are beyond the scope of this work. The RDC simulations converged to a steady state value of 0.02 kg/s for hydrogen and 0.62 kg/s for air with a global equivalence ratio of 1.1 and a detonation cycle frequency of 4.6 kHz.

6.3 Results

The preliminary results are organized into three sections with the first section highlighting the variations in the detonation wave structure in the axial-azimuthal planes from broadband

chemiluminescence (primarily OH*). The second section makes use of MHz rate OH-PLIF to understand the radial-axial detonation wave structure during the wave passage across the PLIF plane. Finally, the refill process is explored and differences between configuration 1 (BFS) and configuration 2 (ramp) are studied.

The baseline condition for this study has an air throat mass flux of G_{air} = 750 kg/m^2/s and a global equivalence ratio of 1.05. This baseline condition was used for both the experiments as well as the simulation. In addition to this condition, a lower mass flux case of G_{air} = 350 kg/m^2/s was studied using MHz OH PLIF to understand the effect of injector recovery and mass-flux for the two different injectors.

6.3.1 Broadband chemiluminescence at the baseline condition:

The broadband chemiluminescence (primarily OH* [32]) obtained at 1 MHz are shown in Figure 6.5 (a) and (b) for the two injector configuration. The first observation is that for the BFS case, the wave appears to be steep fronted with a thin reaction zone that is consuming the axially incoming reactants. Whereas in configuration 2, there appears to be a distributed reaction front with much less steep gradient features in the detonation structure.

In addition to the wave structure difference, the BFS appears to a have a single steep fronted trailing luminous shock. However, in the case of the ramp, there are multiple distributed waves trailing the wake of the leading detonation front. These complex wake physics are a results of azimuthal shock systems present in RDCs. [24,51,83] and will require addition investigation to understand the detonation wave structure dynamics.

Another key difference is the wave-speed. The BFS, for the same operating conditions, appears to have a faster wave speed achieving close to 80% C-J while the ramp appears to have a lower C-J value of 69% suggesting the ramp performance to be lower than ideal C-J detonation waves.

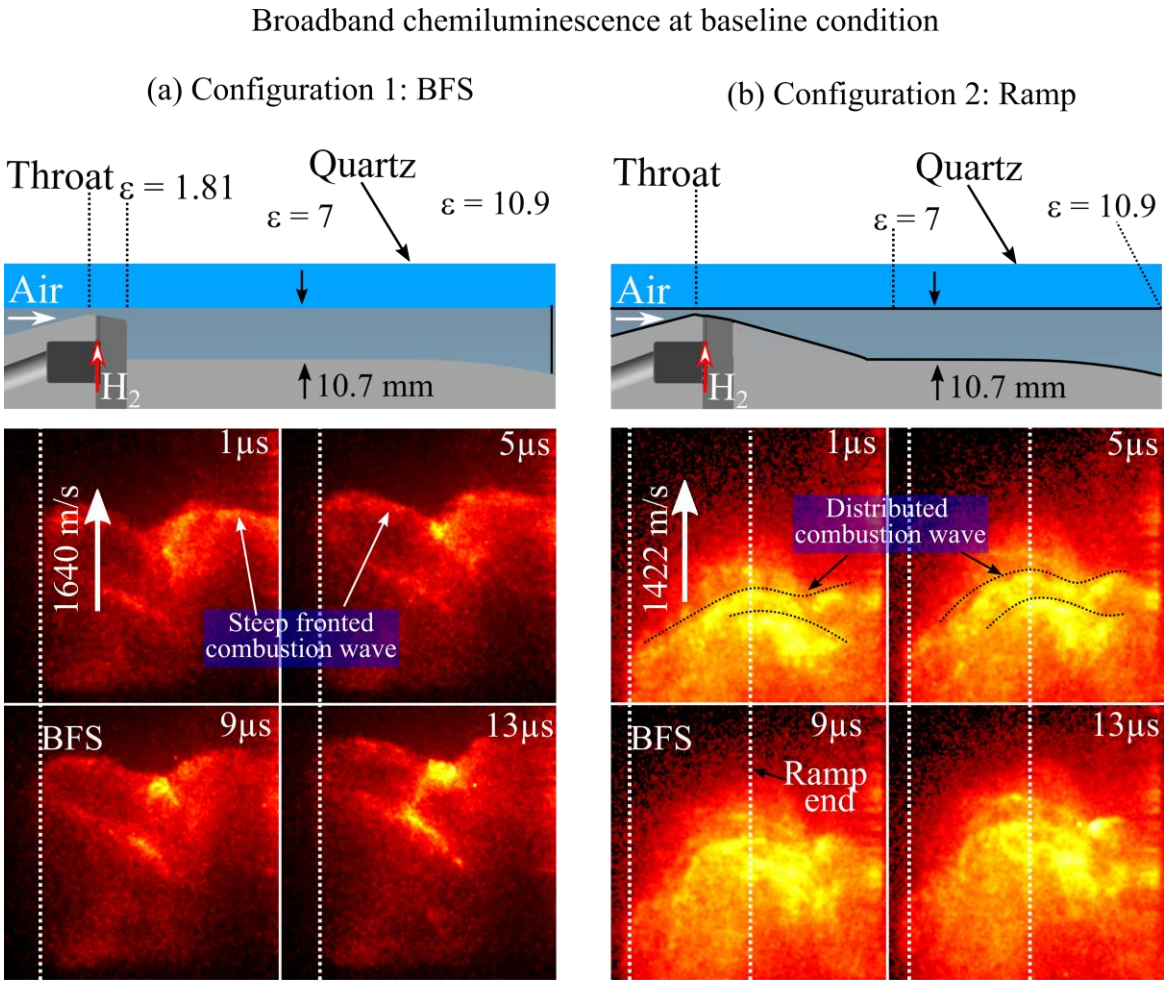

Figure 6.5: MHz rate broadband chemilumienscence. (a) The cross section of the BFS architechure is shown in the top while 4 selected sequential images are shown during the wave propagation. The wave is traveling at 1640 m/s fro the BFS case with the dotted line marking the BFS location. (b) The cross section of the ramp configuration is shown. The wave is traveling at 1422 m/s with the BFS location and th end of ramp location is shown as two dotted lines.

6.3.2 MHz rate OH PLIF

THOR test platform can be used for rapid iteration on injector optimization. The BFS in the initial design of the RDE provided a flat wall for axial pressure oscillations to sustain within the annulus. In addition, product gas from the previous cycle was trapped in the recirculation zone leading to pressure loss from shear layer interactions of incoming reactants. To minimize the total-pressure loss from this injector, a first optimization effort was done where the BFS was replaced with a slow expanding ramp at a ramp angle of 10°.

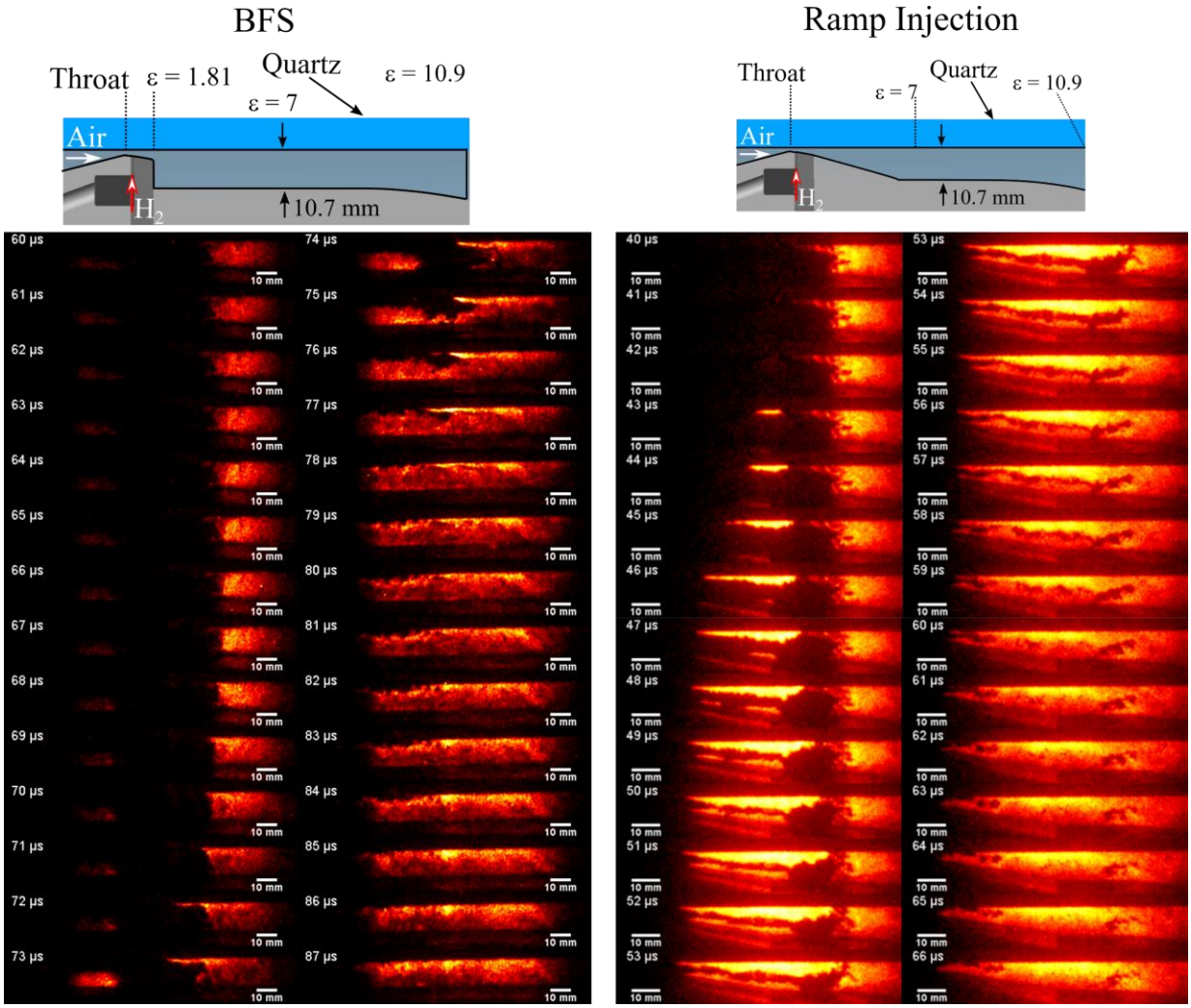

Figure 6.6: Radial axial MHz rate OH PLIF for the BFS vs the Ramp Design.

The detonation structure, compared to the BFS, is very different. For the BFS case, the detonation wave is observed to have a leading edge in the recirculation zone and the exhaust. However, for the ramp design, the detonation wave is observed to arrive at the center of the axial refill near the outer radius. For the BFS case, the detonation wave passage lasts only ~14 μs (72-86 μs) while the ramp design has a detonation wave passage occurring for ~20 μs (43-63 μs). The detonation wave for the ramp design has azimuthally distributed. However certain phenomenological similarities can be observed between the two cases. 1) The first increase in OH signal occurs in zones with OH signal from the previous cycle – due to increased speed of sound in these zones. 2.) The leading zones of the detonation travel on the outer wall.

6.3.3 Injector recovery

(a) BFS design

Figure 6.7 (a) and (b) shows the OH signal obtained near the injection system for the low air mass flux case of 350 kg/m2/s and 750 kg/m2/s respectively. A schematic representation of the injector boundary is drawn in Figure 6.7 (a) at 119 μs (Annotation A) and 47 μs for Figure 6.7 (b). For both the figures, the signal counts upstream of the BFS was multiplied 2 times while the signal downstream of the BFS was scaled 1/4th of the original signal. This intensity scaling provides the best contrast to observe the OH signal propagation upstream of the BFS.

For the low mass flux case (a), the detonation wave is observed to arrive at ~105 μs while the product gas propagation upstream of the BFS is observed for the first time at 115 μs. At this point, the OH signal propagates upstream until reaching the cold hydrogen jet marked by the absence of OH. This can be observed at 131μs in Figure 6.7 (a). The OH products are observed to propagate upstream beyond the air-injection throat, into the air-manifold. At this time, the pressure is observed to be sufficiently high to stop fuel and air flow. At ~141 μs the observed "dark patch" indicating the presence of unburned hydrogen, slowly advances towards the exhaust. Once the detonation product gas expands azimuthally and axially towards the exit, the pressure drops sufficiently in the combustion chamber to initiation injection of reactants. This can be observed from 141 μs to 163 μs (Annotation B).

However, for the higher mass flux case (Figure 6.7 (b)), the product gas propagation upstream is minimized. This is due to two reasons. (1) Assuming the pressure ratio across the detonation wave is constant, the fast axial injection velocity results in a lower pressure static pressure near the injection system, which results in low post detonation static pressure. (2) Ability of product gas to expand in the azimuthal direction.

(b) Ramp design

For both the mass fluxes (Figure 6.7 (c) and (d)), we observe very minimal product backflow into the injection system. Due to the fast-expanding jet and the geometric constraints, the product gas is observed to preferentially vent towards the exhaust rather than the injection system. On the onset, there also appears to be no evidence of deflagrative burning of the incoming reactants with the

product gas, since the products and the reactants have a clear boundary marked by a rapid change in the OH signal from the reactant side to the products side.

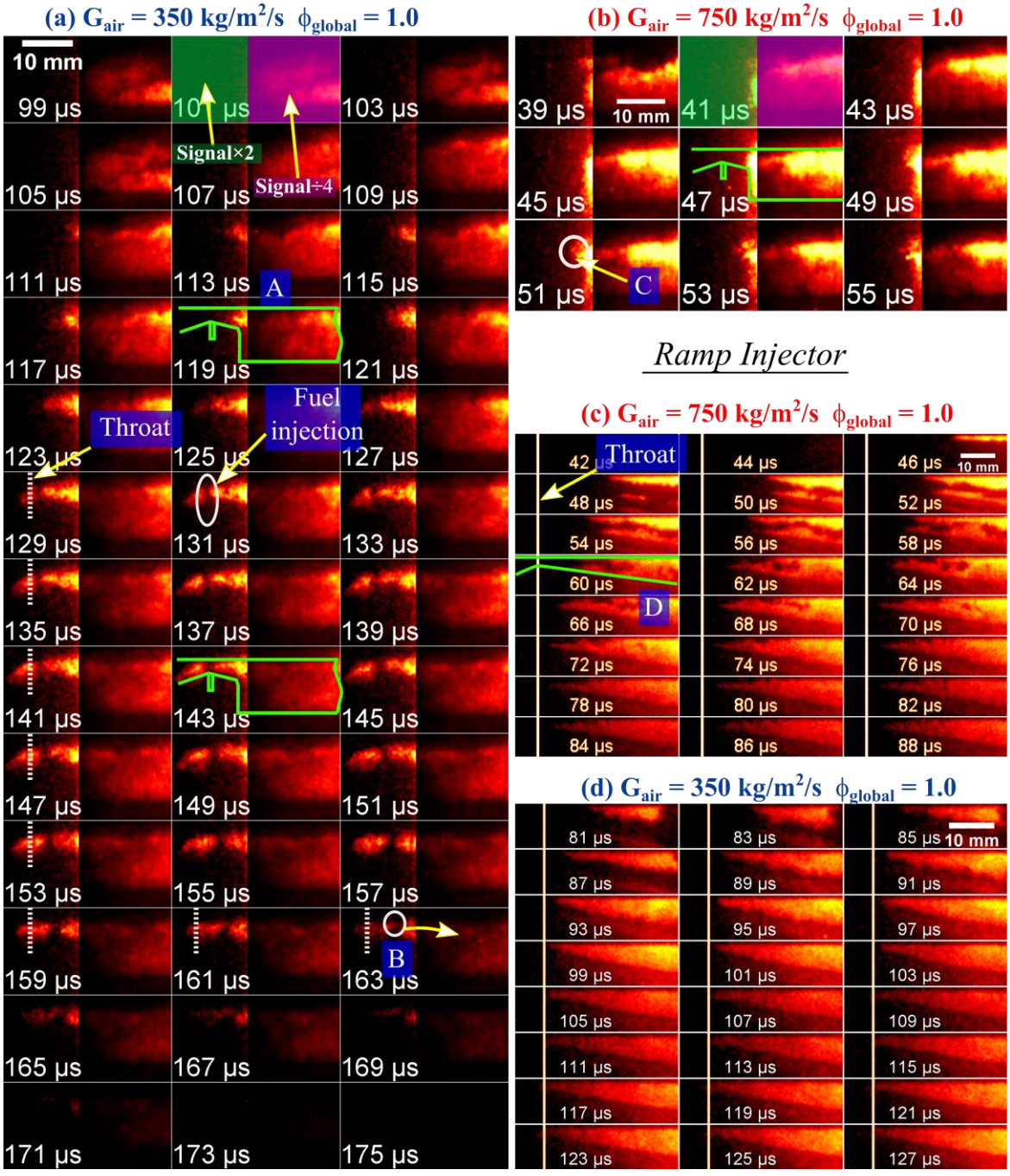

Figure 6.7: (a) and (b) shows the recovery process for the BFS at the low and high mass flux case. (c) and (d) shows ther injector recovery for the ramp at high and low mass flux case respectively.

6.4 Conclusions

An optically accessible jet in supersonic crossflow injection based H_2-Air RDC is studied for two different injection configurations. In the first configuration, the injector passage terminates at a backward facing step (BFS) leading into the combustion chamber while in the second configuration, downstream of the fuel injectors, has a gradually expanding 10° ramp. This geometric ramp design eliminates the presence of a large recirculation zone downstream of the injection system, which can minimize shear layer induced pressure losses in the BFS design. The OH* chemiluminescence reveals a sharp detonation leading front for the BFS design compared to the ramp injector. The unavailability of lateral relief distributes the combustion front into multiple shock induced detonation waves in the wake of the leading detonation front in the ramp. While in the case of BFS, the shock induced detonation zone is well defined and is trailing the leading detonation wave in the injection nearfield. Through the use of PLIF imaging, the BFS design is observed to trap hot-gas from the previous cycle in the BFS location. Combining the use of MHz rate OH* chemiluminescence, MHz rate OH-PLIF and URANS simulations, this work highlights the primary differences in the wave shape, the dynamic response of the detonation wave and the influence of injector geometry on the recovery process of the detonation wave.

7. FEMTOSECOND/PICOSECOND ROTATIONAL COHERENT ANTI-STOKES RAMAN SCATTERING THERMOMETRY IN THE EXHAUST OF A ROTATING DETONATION COMBUSTOR

Spatio-temporally resolved measurements of temperature using hybrid femtosecond/picosecond rotational coherent anti-Stokes Raman scattering (fs/ps RCARS) are evaluated for characterizing the highly dynamic exhaust flow of a non-premixed hydrogen-air rotating detonation combustor (RDC). The RCARS system utilizes a recently developed kHz-rate probe-pulse amplification system that enables high probe-pulse energies and sufficient sensitivity to track RDC exhaust gas temperatures during the short ~1.5 seconds run time with a precision of ~2%. Because of the potential for high spatial gradients in temperature and pressure in the RDC exhaust, estimation of bias errors due to spatial averaging in the 700-µm-long CARS probe volume is conducted by employing the results of a reactive three-dimensional unsteady Reynolds-averaged Navier-Stokes (URANS) model with a structured grid of 48.5 million cells. This results in a potential bias error of ~1.5% due to exhaust temperature gradients and underscores the need for high spatial resolution. The experimental and predicted exhaust temperature histograms show good correspondence with a statistically similar skew-normal distribution relevant to the flow's local dynamical features. By utilizing a high-speed camera synchronized with the CARS system, it was possible to compare the numerical simulation results with the measured exhaust temperature profile obtained from knowledge of the instantaneous detonation-wave azimuth position. Similar azimuthal spatial variations of ~300 K were observed in the experimental and computed temperatures, indicating a relatively well-mixed exhaust flow. The temperature pattern factors of 0.19 and 0.20 obtained from the experimental and numerical data respectively, are relatively close to isobaric combustors in modern gas turbine engines. These results illustrate the ability of the fs/ps RCARS and numerical modeling approaches to evaluate characteristics of the RDC exhaust flow for future development in propulsion and power generation systems.

7.1 Introduction

Continuous improvement in constant pressure combustion over the last few decades has boosted performance and minimized pollutant emissions of modern combustion devices. As improving thermodynamic efficiency requires higher operating temperatures and pressures, a possible

approach to further gains is in the conversion from isobaric to isochoric combustion [7,10]. A concept for isochoric operation that has received broad interest in the last two decades is rotating detonation combustion (RDC) [2,4,87–90]. Detonative combustion provides isochoric heat-release with an increase in the product gas total pressure, an increase in enthalpy, and a reduction in entropy compared to deflagrative isobaric combustion. The RDC concept has a compact flame with high combustion intensity, a simple lightweight construction, continuous valveless propellant consumption, an annular flow path, and the potential for retrofitting into current generation gas turbine engines [91].

A critical parameter to quantify the RDC performance and operating characteristics relevant to propulsion and turbine integration is the exhaust gas temperature. To date, thermometry in RDCs has been performed using intrusive thermocouple probes, thin film pyrometry, or non-intrusive laser absorption techniques. Commercially available thermocouple probes are robust and relatively simple to install and, therefore, have been widely used for temperature measurements in RDCs. Bykovskii and Theuerkauf used thermocouples to compute the axial heat release profile [92] and bulk heat release from RDCs [93]. They reported the calculated heat release in the axial direction to increase near the mixing zone and decrease further downstream [92], albeit with no information on the azimuthal variations. Naples *et al.* used conventional thermocouples to provide estimates of the combustor pattern factor for an RDC retrofitted in a T63 gas turbine engine while discounting the azimuthal variations as well [91]. Computational work from Liu *et al.* have shown that the mean Mach number and the amplitude of fluctuations in the azimuthal direction significantly affect the turbine performance. Hence, high-frequency experimental data is critical to evaluate the turbine efficiency [9,94]. Despite the ease of implementation, the instrument response time of micro-thermocouples (~10 ms) is an order of magnitude longer than that of a typical RDC wave cycle time (~250 μs), resulting in an inability to resolve temperature transients [95,96]. A slightly improved temporal resolution (~1.5 ms) can be achieved using thin film pyrometry. However, due to the filament's fragility, the survivability of the probe in harsh aerothermal environments poses a significant challenge [97].

A popular high-speed non-intrusive alternative to the use of thermocouples and thin-film temperature sensors is laser absorption spectroscopy (LAS). Several groups have performed LAS in air-breathing and rocket RDCs [12,98–100]. Limited spatial resolution due to the path-averaging

and temporal averaging of 300 ns to 10 µs can result in uncertainties in the measured temperature [25].

A well-established non-intrusive diagnostic for accurate temperature measurements is coherent anti-Stokes Raman scattering (CARS). CARS has been extensively used in harsh combustion environments for *in-situ* temperature and species measurements in high-pressure gas turbine and rocket combustors [41,101,110–113,102–109]. This technique offers excellent spatio-temporal resolution and generates a laser-like signal that can be routed far from the probe volume to minimize background noise, such as flame luminosity and laser scattering. In this four-wave mixing technique, vibrational or pure-rotational Raman-active molecular transitions of gas-phase target species are probed [41,114]. The pure rotational CARS (RCARS) approach is attractive for highly dynamic combustion processes due to its high sensitivity over a wide range of temperatures [115], large line spacing that increases the pressure threshold for collisional broadening [116], amenability to a simple two-beam configuration [117–119], and potential to probe simultaneous species with a single broadband laser source (N_2, O_2, CO, CO_2, etc.) [120,121].

Thus far, only a small number of experiments have deployed CARS for temperature measurements in detonating environments. The first reported work on detonation product gas thermometry was done by Grisch *et al.* using ns CARS to probe the N_2 molecule in the product gas of a lead-azide explosion. This ns CARS measurement could measure vibrational temperatures up to 2000 K with a spatial resolution of 4 mm [122]. Roy *et al.* used ps N_2 CARS to measure temperatures behind the shock of a laser-induced blast wave. Compared to the earlier ns work, Roy *et al.* increased the temperature range up to 3600 K with a precision of 5% and improved spatial and temporal resolution to 30 µm and ~130 ps, respectively [123]. However, the aforementioned techniques were limited to a repetition rate of 10 Hz.

Recently, Dedic *et al.* used hybrid fs/ps VCARS to measure the gas-phase temperature behind the detonation wave in a microscale detonation tube at 1 kHz [124], where non-equilibrium effects on rovibrational population were considered. Richardson *et al.* measured post-detonation fireball temperatures using hybrid fs/ps RCARS. However, to fulfil the requirement of high pulse energy in the ps probe for sensitive thermometry at post-detonation temperatures, a separate 20 Hz ps laser was used for the probe pulse [125]. This limits the measurement at relevant time scales for post-detonation environments. Moreover, the high cost of using two separate lasers and experimental complexities associated with the precise time synchronization of two fs- and ps-

lasers are challenges with this technique. On the other hand, the ps probe pulse for hybrid fs/ps RCARS can be extracted directly from the fs laser source using various spectral filters, such as a 4-*f* pulse shaper [126], a narrow bandpass filter [127], a Fabry-Perot etalon [128,129], or volume Bragg grating [130]. Unfortunately, these spectral filtering techniques significantly reduce the probe pulse energy (to tens of μJ), and residual sideband features in the ps-probe pulse's spectral and temporal profiles result in limited signal-to-noise ratio (SNR) and temperature dynamic range [127,129]. Alternatively, a second harmonic bandwidth compressor (SHBC) has been used to produce a ps probe pulse with ~1.1 mJ/pulse and was demonstrated for hybrid fs/ps RCARS temperature measurements up to 2400 K [131]. This approach's potential operational challenges are the introduction of phase conjugation, interferences in the SFG crystal, and difficulties in achieving opposite linear chirp between two pulses, which can lead to spectral wings and blue-shifted satellite pulses. These complexities necessitate careful filtering of the ps probe to avoid non-physical features in the RCARS spectra, detailed modelling of the laser pulse characteristics, and/or possibly limit early probing of the Raman coherence. Recently, kHz amplification of spectrally filtered fs pulses by a narrowband spectral amplifier has been demonstrated by the current authors to produce high-energy, nearly transform-limited, ps-probe pulses for hybrid fs/ps CARS with excellent SNR. This approach, used in the current work, enables robust spectral fitting with few adjustable modelling parameters at flame temperatures ~2400 K [132,133].

Given the highly dynamic and challenging environment of the RDC exhaust, the current work represents the first effort to evaluate the use of a robust two-beam hybrid fs/ps N_2 RCARS scheme similar to ref. [133] to perform thermometry in the exhaust of a non-premixed hydrogen/air RDC [16,51,134]. The RDC was operated at global fuel-rich conditions for 1.5 seconds with a detonation cycle frequency of ~4.1 kHz. Temperature measurements were made at 1 kHz repetition rate, and the relative position of the detonation wave with respect to the probing location was tracked using a high-speed camera synchronized with the RCARS system. A temperature map around the azimuth is plotted along with an ensemble-averaged azimuthal pattern factor from multiple cycles in the RDC exhaust. In parallel, data from a 3D non-premixed unsteady Reynolds averaged Navier Stokes (URANS) simulation using ~48.5 million cells are used to calculate the temperature profile at the exhaust for comparison with the experimental data. Using the flow-field characteristics from the URANS simulations, a theoretical estimate of the measurement uncertainty due to spatial gradients is performed. In addition, statistical distributions and computed

pattern factors are compared and show good correspondence with experimental temperatures. The kHz-rate fs/ps RCARS system performance is described in detail and delivers excellent precision for characterizing the RDC exhaust and validating numerical models of the full combustor geometry.

7.2 Experimental setup

7.2.1 RCARS instrument

The hybrid fs/ps N_2 RCARS approach employs simultaneous broadband fs pump (ω_{pump}) and Stokes (ω_{Stokes}) beams to impulsively excite rotational Raman transitions, followed by a time-delayed (τ_{probe}) narrowband ps beam to probe the evolving coherences in the frequency domain, as shown in Figure 7.1. The probe delay provides sufficient time to minimize background noise from the fast decaying (< 200 fs) nonresonant (NR) background signal. The phase-matching scheme based on momentum conservation for a two-beam RCARS setup with a crossing angle (θ) is shown in Figure 7.1 .

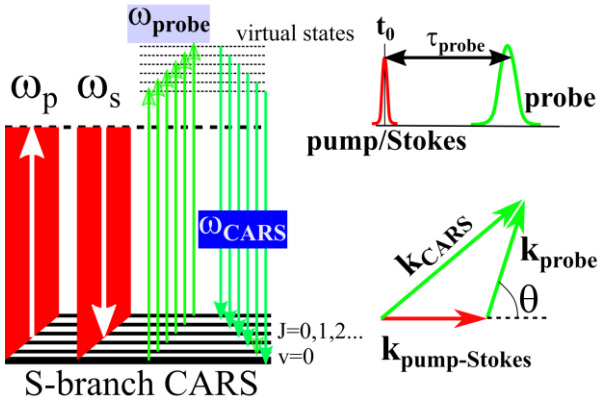

Figure 7.1: Energy level, time, and phase-matching diagrams for the fs/ps RCARS process.

Figure 7.2 shows a schematic of the two-beam RCARS system used for measurements in the RDC exhaust. The regeneratively amplified Ti:sapphire source laser (Solstice Ace; Spectra-Physics, Inc.) outputs nearly transform-limited kHz-rate 100 fs pulses at 800 nm with 7 mJ/pulse and spectral bandwidth of ~180 cm^{-1}. This output pulses are split into two, with 3 mJ/pulse routed to a half-wave plate (HWP) and thin-film polarizer (TFP) to control the energy of the pump/Stokes beam. The pump/Stokes beam energy is limited to ~100 µJ/pulse to avoid self-phase modulation

or plasma generation in the probe volume. The remaining 4 mJ/pulse from the source laser is used to pump an optical parametric amplifier (TOPAS Prime, Light Conversion, Inc.) and produce a 1064.4 nm beam with a bandwidth of 180 cm^{-1}, a pulse width of 100 fs, and energy of ~60 µJ/pulse for seeding an Nd:YAG narrowband spectral amplifier (NSA) [133]. The NSA has a volume Bragg grating (VBG) at the entrance to decrease the seed pulse spectral bandwidth to 1.9 cm^{-1}, which corresponds to 10 ps pulse duration. After frequency doubling, the NSA provides a 532.2 nm probe beam having 800 µJ/pulse at 1 kHz. A delay stage is introduced in the fs pump/Stokes beam path to delay the ps probe beam by ~20 ps.

The combined pump/Stokes and probe beams are routed towards the RDC exhaust over a path of ~8 m from the laser laboratory to the RDC probe volume. Near the RDC exhaust, the pump/Stokes and probe beams are focused with a single 300 mm lens (L1 in Figure 7.2), yielding a crossing angle of 10º. The spatial resolution can be approximated geometrically by $D_0/\sin(\theta)$, where D_0 is the focused diameter of the combined pump/Stokes beam, and θ is the crossing angle. For the current configuration, the measured beam-waist of 50 µm and 10º crossing angle results in an estimated spatial resolution of 700 µm along the beam propagation axis and 50 µm in the radial direction. A detailed view of the beam-arrangement at the RDC is shown in Figure 7.3Figure 7.3 (a). For the phase-matching scheme selected, the probe and the CARS signal co-propagate after the interaction volume. The CARS signal is collimated along with the probe beam using another 300 mm plano-convex lens (L2 in Figure 7.2) and routed back to a spectrometer in the laser laboratory. A half-wave plate (HWP) and polarizer/analyzer combination are introduced in the probe beam path before and after the probe volume, respectively, to allow for polarization suppression [41] of the residual probe beam. To eliminate the residual probe beam prior to dispersing the CARS signal, additional spectral filtering is introduced through a VBG notch filter (NF) and bandpass filter (BPF), as shown in Figure 7.2. After suppressing the residual probe, the CARS beam is focused on the spectrometer (Acton SP-500i, Princeton Instruments) with a 100 mm lens. A 1200 groove/mm grating is used to disperse the CARS signal onto an electron-multiplying (EM) CCD camera (Newton U971P, Andor). The EMCCD camera is synchronized with the 1 kHz primary laser and captures a vertically binned area of 250 (H) x 70 (V) pixels, providing a spectral resolution of 45 pixel/nm with a signal bit depth of 16-bits.

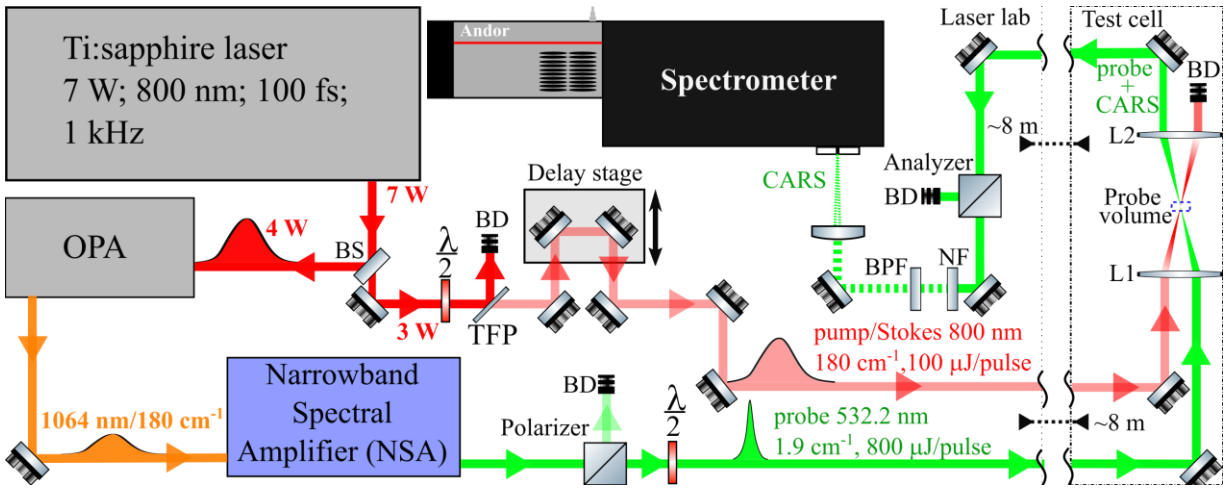

Figure 7.2: Optical arrangement of the CARS system. OPA – optical parametric amplifier, BS – Beam Splitter, λ/2 – Half Wave Plate, TFP – Thin Film Polarizer, L1 – Lens 1 (f = +300 mm), L2 – Lens 2 (f = +300 mm), BD – Beam Dump, NF – Notch Filter, and BPF – Band Pass Filter.

7.3 RDC description and test conditions

The hydrogen-air RDC has a mean annulus diameter of 128 mm and a combustion section length of ~100 mm. A cross-section view of the flow path for the RDC is shown in Figure 7.3 (b). High-pressure air enters from a plenum through a converging-diverging section with a throat gap of 1.45 mm. Fuel is injected radially through 100 equally spaced slots in the diverging section downstream of the throat and normal to the air stream. The slots have a diameter of 0.4 mm and a depth of 0.6 mm and are located at an area ratio (ε) of 1.16. The flow channel expands through a backward-facing step (BFS) leading into the combustor channel. The stainless-steel (SS304) outer body of the RDC has instrumentation ports for measuring surface temperature and pressure at multiple axial and azimuthal locations.

Table 2: RDC test conditions.

Case #	G_{air} ($kg/m^2/s$)	$\dot{m}_{air}$ (kg/s)	$\dot{m}_{fuel}$ (kg/s)	ϕ_{global}	τ_{probe} (ps)
1	750	0.44	0.0150	1.17	20
2	750	0.44	0.0215	1.68	20
3	750	0.44	0.0272	2.12	20

The hydrogen and air mass flow rates are metered using choked sonic nozzles. The dry air mass flow rate can be varied from 0.22 kg/s to 2 kg/s, corresponding to a global equivalence ratio (ϕ_{global}) range of 0.5 to 2. The uncertainty in the mass flow rate is computed to be ~3%. The computational model domain ends ~15 mm upstream of the experimental probe location, as shown in Figure 7.3 (b). This leads to a lower static temperature in the measurements than the CFD model predictions, as discussed in section 7.7.3. To capture the instantaneous detonation wave position during RCARS measurements, a high-speed camera (Photron SA-Z) with a 100 mm focal length lens is positioned to view an image of the exhaust plume of the RDC reflected by a 300 mm x 400 mm silver mirror, as shown in Figure 7.3 (a). The high-speed camera with an exposure time of 1 μs is synchronized with the 1 kHz CARS system. At the start of the test, cold air and fuel are flowed through the venturi at target pressures to achieve the desired mass flows (~0.5 s). Once the RDC is primed, detonations are initiated by introducing a pre-detonator discharging radially outward at an axial distance 12 mm downstream of the BFS. The CARS spectrometer camera and the exhaust plume camera are synchronized with the primary fs laser and triggered simultaneously during RDC priming. The RDC reaches a limit cycle in ~40 ms after the start of the test. The test duration is set to 1.5 s, producing ~1500 RCARS measurements per test. The RCARS data and the high-speed camera data are trimmed to the test duration in post-processing. In addition to exhaust temperature measurements, wall pressures and temperatures are sampled at 2 kHz repetition rates for condition monitoring of the experiment. In this study, three fuel-rich cases are explored with a throat air mass flux of G_{air} = 750 $kg/m^2/s$ at ϕ_{global} of 1.17, 1.68, and 2.12, as shown in Table 1. Case 1 is considered the baseline condition, for which extensive analysis is performed and experimental measurements of pressure and temperature were used to provide the boundary conditions to initiate the URANS simulations.

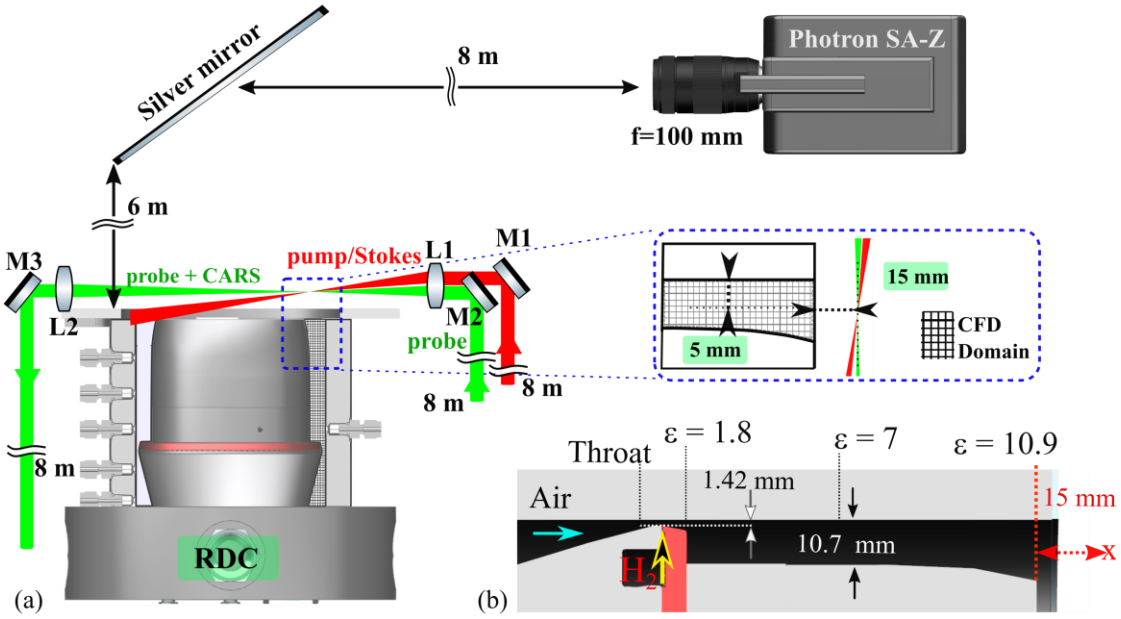

Figure 7.3: Experimental configuration for two-beam RCARS measurements. (a) Pump/Stokes and probe beam crossing arrangement through a single lens system. A silver mirror was placed ~6 m from the RDC exhaust plane to view the azimuthal position of detonation wave with respect to the probe volume location using a high-speed camera synchronized with the RCARS system; M1 – Broadband Mirror, M2/M3 – 532 nm mirror, L1/L2 – 300 mm plano-convex lens. (b) Cross-sectional view of the flow-path indicating the axial end of CFD domain and the relative location of CARS probe volume at X.

7.4 Numerical model

Unsteady Reynolds averaged Navier Stokes (URANS) simulations of the RDC were performed with the CFD++ (Metacomp [72]) flow solver. The solver was selected for its capability to model transonic/supersonic flow features and was validated in prior work by the current co-authors in non-reacting supersonic environments [73] and for capturing the spatio-temporal characteristics of hydrogen-air deflagration-to-detonation transition in a straight detonation tube [135].

The numerical domain in the current work was developed based on a grid independence and time-step study using this solver in an RDC geometry [136]. As shown in Figure 7.3 (a), it extends from the inlet plenum to the RDC's exhaust and consists of the air-inlet plenum, 100 discrete fuel injection holes, the air injection throat, the BFS, and the combustor annulus. A structured grid of ~48.5 million cells with boundary layer refinement to capture the laminar sublayer is built with Ansys ICEM. The 3D simulations were performed with a k–ω SST

turbulence model with a single-step chemistry reaction for hydrogen-air reactions following a method used in prior RDC simulations by Frolov *et al.* [74]. A detonation tube analysis was performed using this mechanism, and the predicted Chapman-Jouget (CJ) detonation wave speed was within 1% of the theoretical value at stoichiometric conditions.

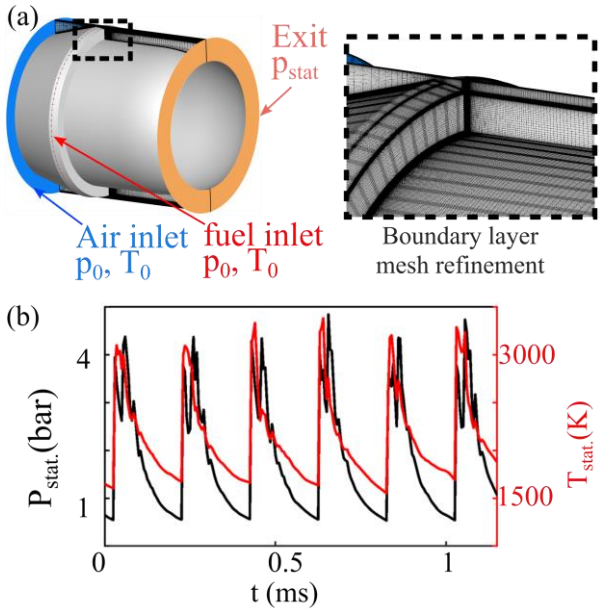

Figure 7.4 (a) Numerical domain and boundary conditions of the URANS simulation. A close view of the boundary layer mesh refinement focused on the injection system is shown in the inset. (b) Pressure and temperature variations at a location 25 mm downstream of the BFS during the limit cycle behavior of the URANS simulation after detonation initiation.

The numerical boundary conditions at the inlet plenum of air and fuel were supplied from static pressure measurements obtained for Case 1 in Table 1, with a total pressure of 5 bar and 290 K for the air inlet and 5.3 bar and 290 K for the hydrogen inlet. A mixed supersonic/subsonic boundary condition with a back pressure of one bar is imposed at the exhaust. Adiabatic non-slip wall conditions were applied for the wall boundaries. The initial simulations were performed with a coarse grid for ~30 cycles, and then boundary layer mesh refinements were imposed. The computational model was run on 120 high-performance computing (HPC) cores. The simulation results were obtained from a snapshot of ~30 cycles after reaching a limit cycle on the fine boundary mesh. The pressure and temperature data shown Figure 7.4 (b) was sampled at a 5 µs time interval located ~1 mm downstream of the BFS and a mid-annular radius of 5.9 mm. The RDC simulations converged to a steady-state value of 0.02 kg/s for hydrogen and 0.62 kg/s for air with a global equivalence ratio of 1.10 and a detonation cycle frequency of 4.6 kHz. The method

of applying measured pressures as boundary conditions resulted in a slightly higher predicted mass flow than in the experiments.

The potential difference in RDC operation for equivalence ratios of 1.10 and 1.17, corresponding to the simulation and experiments, was estimated using equilibrium detonation calculations using the NASA CEA solver [75]. These calculations show that the detonation product gas temperature would differ by only 2.25 K for such a difference in global equivalence ratio. Hence, the RDC's global thermal power output is expected to be minimally affected by the small difference in ϕ_{global} between the experiment and simulation.

A commonly used parameter to compare simulation results with experiments is the percent deviation of detonation cycle frequency with the experimental counterpart. Lietz *et al.* used a large eddy simulation (LES) model on a hexahedral grid with 90 million cells for a rotating detonation rocket engine (RDRE) and approached to within 8% of the experimental cycle frequency [137]. Sato et al. used a 28 million unstructured mesh in a non-premixed RDC and approached within 15% of the experimental cycle frequency at the same fuel-air combination in a comparable geometry [57]. In this work, the predicted RDC cycle frequency is within 7% of the experimental counterpart (4.3 kHz) at similar operating condition.

7.5 Evaluation of the fs/ps RCARS approach

An analysis is performed to estimate the measurement precision, bias errors due to limitations in spatial resolution, and measurement dynamic range for the selected fs/ps RCARS instrument at the temperatures and pressures imposed by the RDC exhaust. This is accomplished with the aid of (1) prior data using the same fs/ps RCARS technique in a fuel-rich hydrogen-air Hencken burner calibration flame [133], and (2) estimates of property gradients and conditions in the RDC exhaust using the URANS predictions.

7.5.1 Exhaust plume characterization

Pressure and temperature contours within the RDC exhaust from the URANS simulations are presented Figure 7.4 for Case 1 in Table 1, with a grid resolution of 100–300 μm in the tangential direction and from 30–300 μm in the radial direction. These data are used to perform a sensitivity analysis of a 700 μm long fs/ps RCARS probe volume, oriented along B-B' in Figure 7.5 (a), to

help estimate the effects spatial gradients and property fluctuations on the measurements. The exhaust contour plots show the azimuth angle reference (red line) at 0º, as used throughout this manuscript, with a thermal wave depicted near the fs/ps RCARS probe location at ~180º. The temperature and pressure distributions are relatively uniform in the azimuthal direction, except in the regions carrying the remnants of the rotating detonation wave within the combustor annulus. The predicted pressures and temperatures within the exhaust show a variation of 0.6–4 bar and 800–3000 K, respectively, at the exit plane, which can be used to estimate potential gradients within the RCARS probe volume.

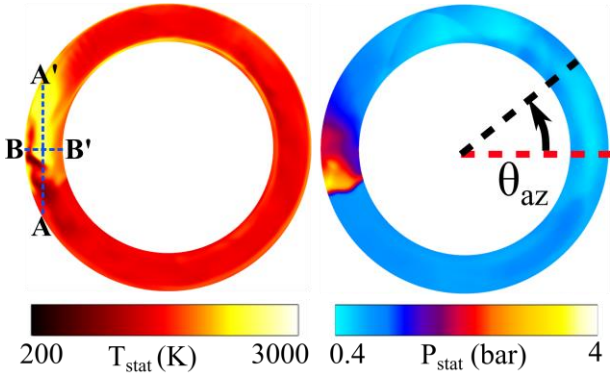

Figure 7.5: Exhaust contour profiles of temperature and pressure. Numerical data sampled along the lines A-A' (azimuthal) and B-B' (radial) are used for analyses of the effects of spatial averaging on the RCARS measurements (Section 7.5.2). In this work. the RCARS probe volume extends along the radial direction B-B'. The red line marked in the pressure profile references the 0° azimuth angle.

Figure 7.5 (a) and (b) provide detailed line plots of the temperatures and pressures, respectively, across the remnants of the detonation wave, in the azimuthal (A–A′) and radial (B–B′) directions shown in Figure 7.5. Based on these data, the pressures within the RCARS probe volume at any instant vary by only ~2×10^{-4} bar, while the temperatures can vary by as much as ~60 K, as discussed in the following section.

7.5.2 Precision and bias error due to spatial averaging

A key parameter in the selection of the pump/Stokes and probe beam-crossing angle is the size of the RCARS probe volume and its effects on measurement accuracy. In prior work, the current fs/ps RCARS approach was used in an fuel- rich hydrogen-air Hencken burner calibration flame

with a beam-crossing angle of 30º, leading to a limiting resolution down to 100 µm [133]. To ensure high signal levels for measurements in the RDC exhaust, the crossing angle was reduced to 10º, leading to a probe volume of 700 µm along the probe beam axis. Even longer probe volumes of several millimeters or centimeters have also been utilized in prior work, but at the expense of spatial averaging [101].

An estimate of the precision error associated with spatial averaging over a certain length is obtained from the percentage coefficient of variation (%COV). The %COV is obtained from the ratio of

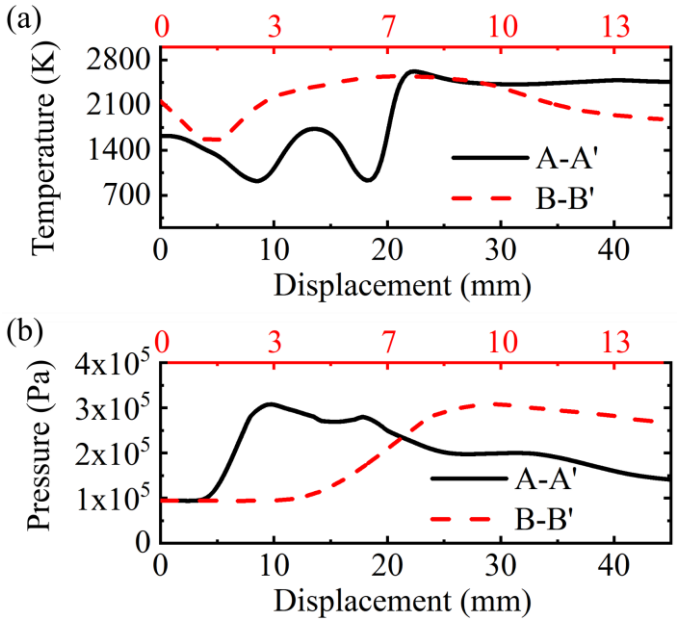

Figure 7.6: (a) Temperature and (b) pressure profiles along the A-A′ (azimuthal) and B-B′ (radial) directions.

the standard deviation in temperature to the mean temperature over a certain distance. For a 700 µm resolution, the URANS simulations estimate a %COV within 1.5% for both the tangential (A–A′) and radial (B–B′) directions. This temperature ambiguity is within the precision of 2% achieved using the same fs/ps RCARS technique in a steady laminar calibration flame [133]. Hence, the selection of a 10º beam-crossing angle in the current work appears to be a reasonable means of increasing signal levels while maintaining the high precision of the measurement system. For future reference, increasing the probe volume to a typical length of 2 mm, as used in prior work, would result in %COVs of 11% and 19% for the azimuthal and radial directions, respectively,

while increasing the probe volume length further to 4 mm would yield %COVs of 28% and 38%. This illustrates the potential uncertainties that can result from low spatial resolution for measurements in highly non-uniform flow fields present in the exhaust of RDCs.

Spatial averaging through a probe volume with large gradients in temperature can also lead to bias errors due to the non-linear dependence of CARS intensity on the local temperature. Consequently, low-temperature zones have a higher CARS signal contribution than high-temperature zones. Such bias errors due to spatial averaging are estimated using simulation results from a steep gradient zone (~20 mm) in Section A–A′, as shown in Figure 7.6(a). In this zone, temperatures range from ~1340–1420 K over the 700 μm RCARS probe length, with an average temperature of 1376 K and a standard deviation of 20 K. Theoretical CARS spectra were generated for this temperature range and were ensemble-averaged to emulate a spatially averaged RCARS spectrum. The ensemble-averaged spectrum was then used for curve fitting to obtain a predicted temperature of 1369 K. This results in a bias error of 7 K or 0.5% from the computed average, which is significantly smaller than the precision of the fs/ps RCARS measurements. However, the bias error could increase significantly for longer probe lengths, and together with spatial averaging portends the potential trade-off between signal levels and precision in regions with higher spatial gradients, such as in the interior of the RDC.

7.5.3 Sensitivity, SNR, and dynamic range

In addition to spatial averaging, a key aspect governing the selection of beam-crossing angle is the sensitivity of the measurements to the wide range of temperatures present in the RDC exhaust. As the two-beam RCARS signal generation is not a fully phase-matched process, higher Raman shifts suffer from enhanced phase-mismatch. As such, higher crossing angles yield reduced signal intensities for high *J*-transitions, reducing high-temperature sensitivity. For pure-rotational CARS, a spectral window of ~300 cm^{-1} is required for fitting rotational spectra up to a temperature of ~3000 K [115]. The relatively small Raman shifts of RCARS allow the interaction between combined pump/Stokes and probe beams to be nearly phase-matched over a wide range of crossing angles (θ) [119]. Thus, the 10º (~700 μm spatial resolution) crossing angle used in this work ensures minimal phase mismatch up to 300 cm^{-1} while offering sufficient spatial resolution, as discussed in the prior section.

Another important consideration of the measurement system is the SNR needed to ensure accurate fitting with theoretical spectra. While a precise threshold is difficult to define, a peak SNR of 10–30 is often used to ensure that the full range of rotational transitions can be captured at high temperatures [133]. To evaluate the dynamic range of the temperature measurements, a scaling of SNR is presented in Figure 7.7 (a) using prior measurements with a beam-crossing angle of 30º (100 µm probe length) in the 1 atm hydrogen-air calibration burner [133]. For a camera with a 16-bit dynamic range, a signal variation of ~4 orders of magnitude can be recorded, which in theory allows temperatures to be measured with sufficient SNR over a range of ~600 K to 3000 K.

Unfortunately, the RCARS signal degrades substantially during RDC operation because of beam steering and the subsequent loss of pump/Stokes and probe beam overlap due to vibrations and the presence of density gradients in the flow. As such, the beam-crossing angle of 30º was reduced to 10º to improve the likelihood of pump/Stokes and probe beam overlap and ensure sufficient temperature sensitivity through increased SNR, with adequate spatial resolution. While a theoretical increase in SNR of a factor of ~50 might have been expected because of the quadratic increase in RCARS signal with the size of the probe volume, the data in the RDC exhaust displayed significant fluctuations and an average increase by a factor of ~7 or less in the observed peak SNR as compared with prior data at a 30º crossing angle. Random variations in beam overlap during the 1.5 second tests were such that a peak SNR of ~100 might be observed at 2600 K, while SNRs might dip as low as 20 at 1200 K. Hence, the optical set up serendipitously ensured sufficient dynamic range for detection of the highest temperatures while also allowing non-saturated signals at the lowest temperatures, with measurement realizations reaching a validity rate of 20–33%.

7.5.4 Effects of pressure on optimal probe pulse width

Because the large line spacing of pure-rotational transitions allows individual rotational lines to be resolved, and avoids the line mixing effects in VCARS, the effects of pressure variations are less pronounced on the RCARS spectrum. Nonetheless, collisional dephasing can still increase at higher pressures and cause a drop in SNR. To illustrate the selection of an appropriate probe pulse, Figure 7.7 (b) shows the dependence of peak SNR on pressure near exhaust temperatures of ~2400 K for probe bandwidths of 1.9 cm^{-1} and 3.3 cm^{-1} at their respective optimal probe delays of 20 ps and 13 ps, respectively. As the URANS simulations predict a static pressure of up to ~4 bar in the RDC exhaust, the 1.9 cm^{-1} probe pulse maximizes SNR for the current work.

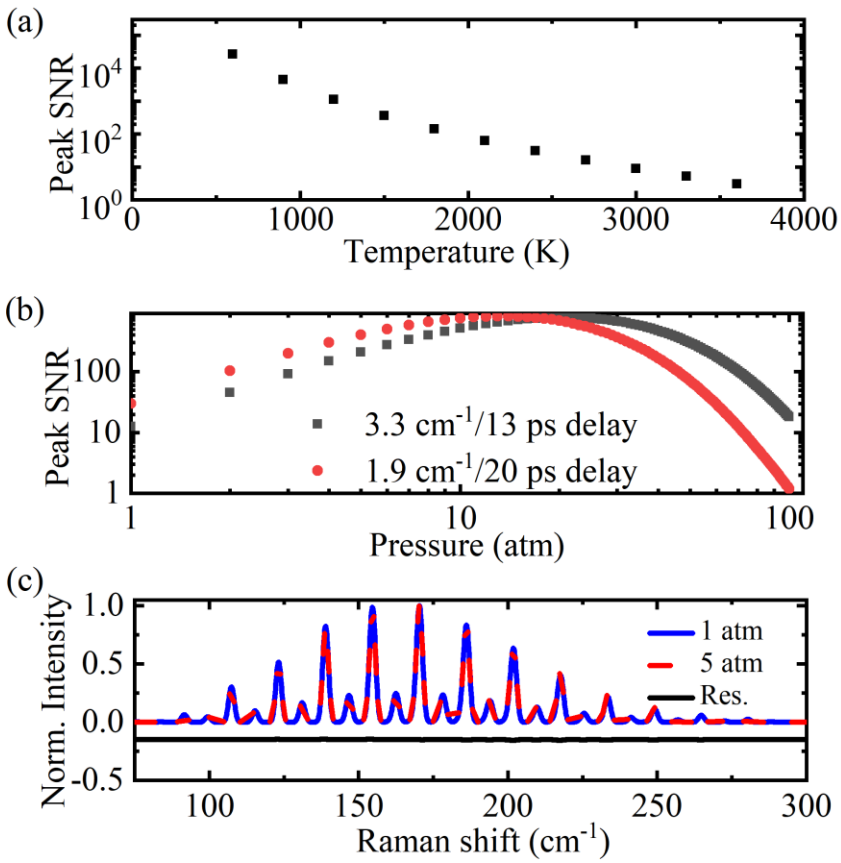

Figure 7.7: (a) Modeled variation of peak SNR vs. temperature in 1 bar calibration burner with 1.9 cm^{-1} probe, 20 ps probe delay, and 30^o crossing angle. (b) Peak SNR vs. pressure at 2400 K for two different probe pulse widths at their optimum probe delay. (c) Modeled N_2 RCARS signal for 2400 K at 1 and 5 bars.

At higher static pressures, such as within the interior of the RDC, the effects of collisional dephasing will be more pronounced, and a spectrally broad (e.g., 3.3 cm^{-1}) and temporally short (e.g., 5 ps) probe pulse may be more optimal. In that case, probing the molecule earlier in time would avoid effects of collisional dephasing, while reducing the probe pulse width would avoid NR background due to temporal overlap of the probe and pump/Stokes pulses.

A final consideration for the use of 1.9 cm^{-1} probe pulse is the potential for temperature-dependent collisional dephasing at the correspondingly longer probe delay of 20 ps. As lower-*J* transitions dephase faster than the higher *J* transitions, this can cause an apparent population shift to higher *J* numbers at high pressures [106]. As shown in Figure 7.7 (c), however, collisional dephasing has a negligible effect on the RCARS spectrum over the pressure range of up to 5 bar for the RDC exhaust in the current work.

7.6 Results

The results are organized into two sections, (1) a description of theoretical fitting for measured temperatures at various operating conditions of the RDC, and (2) a comparison of experimental results with URANS simulations, including temperature statistics and pattern factor estimation in the RDC exhaust. These data are used to illustrate the potential utility of fs/ps RCARS in quantifying temperature variations and spatial distributions for evaluating RDC performance characteristics as well as for validation of numerical models.

7.7 Fs/ps RCARS temperature measurements

7.7.1 Pre-processing and fitting to the RCARS spectra

Each RDC test provides a total of ~1500 data points for the 1.5-second-long test. Three filter steps were applied to each test case before curve fitting.

(1) Experimental data for shots that have lower signal were filtered with a peak SNR threshold of 10 to minimize uncertainties in the curve fitting procedure. Although the optical arrangement was theoretically capable of providing excellent SNR over the temperature range of interest, vibrations, and large density gradients during the inherently unsteady RDC operation caused a substantial drop in signal for some of the single-shot data.

(2) While the RDC was operated in a fuel-rich condition for all the three test cases (Table 1), to minimize oxygen line interference, the presence of oxygen line interference suggested the occurrence of intermittent incomplete combustion. These data points were removed before curve fitting. As the numerical results do not capture intermittent pockets of unburned fuel and air, it is anticipated that filtering such spectra may artificially improve comparisons with the experimental data.

(3) During the last ~100–300 ms of the test, the RDC's exhaust plume had sufficient water-vapor to decrease the SNR of the camera observing the detonation wave position. Although several datapoints that passed the first two pre-processing steps were present, these temperature points could not be appropriately assigned with any azimuth location and hence were eliminated for the pattern factor estimation. After applying several layers of filtering, approximately 50% to 75% of the data points were eliminated for each test case leaving ~300 to 600 datasets per test case.

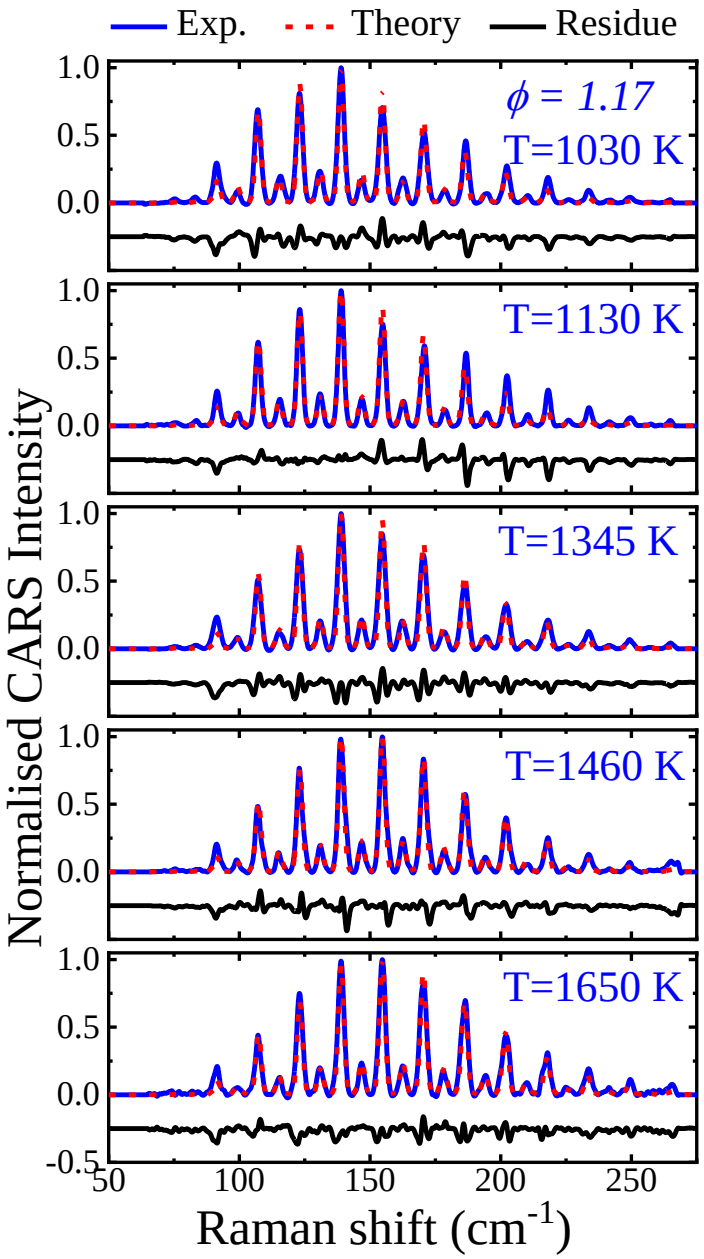

Figure 7.8: Typical single shot RCARS spectra and the corresponding theoretical fits showing the dynamic range of the measurement at the baseline condition Case 1 (Table 2).

A phenomenological N_2 RCARS model was implemented based on prior work [129,138,139] and is detailed in [140]. The pump/Stokes pulse was assumed to be impulsive in time-domain, i.e., having infinite bandwidth that was not included explicitly in the model. Rather the spectral response of the finite bandwidth pump/Stokes beam was imparted on the model with an experimentally obtained NR signal in argon at the RDC measurement location. This was used

along with the spectrometer instrument function and probe shape determined from N_2 RCARS data in a Hencken burner to generate a library of simulated spectra. Pre-processing of the N_2 RCARS data from the RDC included slight background subtraction, normalization to the peak intensity, and wavenumber-axis stretching. A least-squares fitting process was then performed with temperature and wavelength shift as the only floated parameters, with the latter being necessary only because of beam steering in the RDC and the >8 meters long path to the spectrometer. The minimum value of least-squared summation of the residue was used as the convergence criterion to determine the temperature, and datasets with large residues were removed in post-processing. The obtained temperatures were then mapped to the detonation wave position to obtain the azimuth temperature profile.

Typical single-shot experimental spectra and corresponding best-fit results for the baseline condition Case 1 (G_{air} = 750 kg/m^2/s, ϕ_{global} = 1.17) are shown in Figure 7.8. The CARS spectral library was computed in steps of 5 K to ensure a relatively high accuracy and efficient convergence criterion. The SNR of the RCARS spectra is sufficiently high for a wide range of temperatures. The relatively low residue appears to be dominated by local variations in the transition linewidths rather than peak amplitudes, potentially making the residue less sensitive to temperature via the Boltzmann distribution.

7.7.2 Temperature statistics in the RDC exhaust

The histograms in Figure 7.9 provide statistics to understand the temperature distribution at various operating conditions. For all three test cases of ϕ_{global} = 1.17, 1.68, and 2.12, G_{air} was set to 750 kg/m^2/s. The uncertainty in the global equivalence ratio was on the order of 2%. The number of data points included in the histograms for Cases 1, 2, and 3 are 530, 340, and 300, respectively.

Case 1 at ϕ_{global} = 1.17 is the case that is closest to a stoichiometric condition and shows a distribution centered at ~1500 K. The slight skew-normal trend towards high temperatures is likely due to products of the detonation wave that remain locally unmixed and lead to thermal transients. The histograms for Cases 2 and 3 show distribution peaks at ~1300 K, with substantially more low-temperature excursions than high-temperature excursions as compared with Case 1. This indicative of the lower temperatures, reaction rates, and combustion efficiencies further from stoichiometric conditions. The statistical distributions for Cases 2 and 3 suggest that the system's thermal power output has plateaued as additional hydrogen is supplied at fuel rich conditions, as

expected. The extra mass flow of hydrogen from Case 2 to Case 3, for example, represents only a 1% increase in the total mass flow for the RDC, which causes an insignificant drop in the mean exhaust temperature.

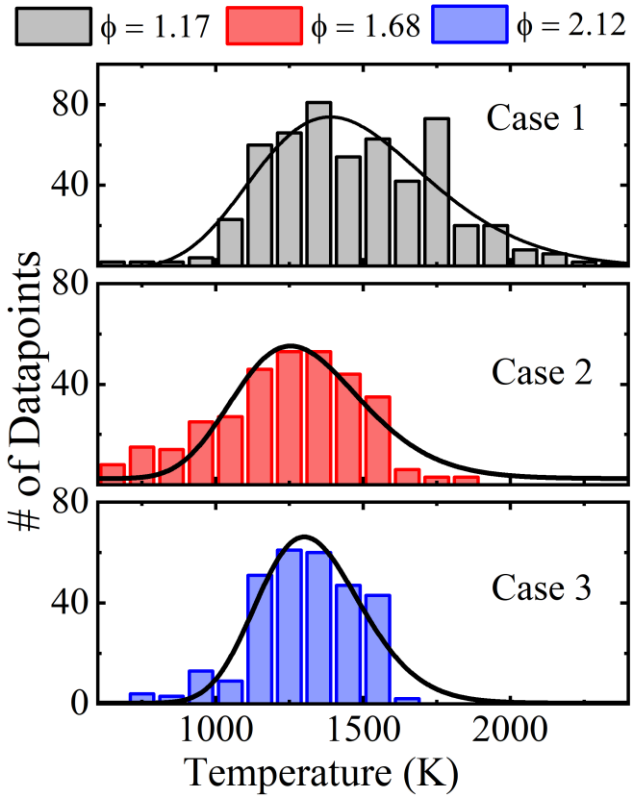

Figure 7.9: Temperature histograms from single-shot data for the three test cases at ϕ_{global} = 1.17, 1.68, and 2.12 for G_{air} = 750 kg/m^2/s.

7.7.3 Comparison of experimental and URANS data

Statistical temperature distributions

The experimentally measured statistical temperature distribution shown in Figure 10 (a) is obtained for Case 1 using data acquired over the duration of a test with a fixed probe volume location as indicated previously in Figure 5. These data are compared with the statistical temperature distribution in Figure 10 (b), which was obtained from the URANS prediction at all spatial locations within the exit plane of the RDC exhaust, as shown in Figure 7.10 (a). This comparison assumes a cyclic passage of the predicted detonation products through the RCARS probe volume.

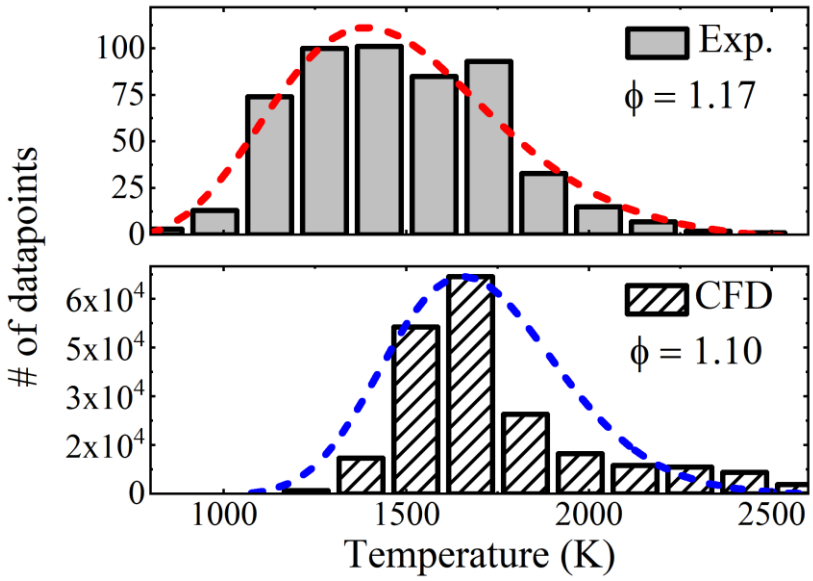

Figure 7.10: Temperature histogram from single-shot experimental data at the baseline condition (Case 1) compared with numerical predictions.

The histograms from the numerical predictions show a similar skew-normal distribution towards high temperatures as observed in the experimental data, indicating that the presence of thermal transients is captured by the URANS simulation. However, the computational plot shows a mean shift of ~200 K towards high temperatures compared to the experiments. As noted earlier, this difference is not attributable to the difference or uncertainty in ϕ_{global}, which would account for a change of <3 K. The primary contribution to the difference in mean temperature is due to the measurement volume being displaced ~15 mm downstream of the computational domain exit plane, as shown in Figure 7.3 (b). Supersonic flow expansion occurs between the end of the computational domain and the probe location, which causes a drop in measured static temperature. For the current RDC geometry, the inner body is contoured to expand from an area ratio of 7 to an area ratio of 10 at the computational exit plane. By approximating a linear decrease in the inner radius, the jet's area ratio at the probe volume is about ~14. This causes a static temperature reduction of ~8%, which accounts for ~125 K of the difference between the experimental and numerically predicted temperatures. The remaining 75 K difference in the mean shift in temperature can be attributed, in part, to wall heat losses and radiation. In fact, it is not unusual to report differences of 50–100 K in measured and equilibrium temperatures within a nearly adiabatic Hencken calibration burner [141]. In addition, the temperature histogram is broader in the

experiments than the URANS predictions, potentially because of the inability of the CFD to accurately capture the range of mixing and reaction rates within the non-premixed RDC (including the limitations of the single-step reaction kinetics). Nevertheless, there is relatively good agreement between the numerical predictions and the RCARS measurements in the exhaust of the RDC after accounting for expected differences in the mean temperatures.

7.7.4 Azimuthal temperature distribution and pattern factor estimation

The azimuthal temperature profile is obtained by correlating temperature measurements with the position of the detonation wave marked by the exit plume imaging system, as described in Figure 3. The detonation wave azimuth position (θ) for a representative single-shot image and the corresponding best-fit N_2 RCARS measurement at 2070 K are shown in Figure 7.11 (a). Measured temperatures are plotted as a function of the corresponding wave positions for an entire test duration in Figure 7.11 (b). These data, along with results from corresponding URANS exit temperatures, are binned into eight 45^o angular sectors and plotted as a function of the azimuth position in Figure 7.11 (c). In both the experimental and computed results, the leading edge of the high temperature products from the detonation wave should be near the 180^o location relative to the reference frame shown previously in Figure 7.5. It should be noted that locations upstream of this leading edge should have lower temperatures while locations downstream should have higher temperatures, depending on the direction of propagation of the detonation wave.

Comparing the mean temperature for each sector within one standard deviation shows statistically strong correlations between the simulations and the experiments. The temperature distribution in Figure 7.11 (c) shows a relatively small spread within each bin (~200 K) for both the experiments and the URANS simulations. On the left side of the 180^o position, a small increase in temperature is observed, attributed to the gradient arising from the detonation wave passage.

The variation in the mean temperature around the entire azimuth is limited to ~300 K. This moderate increase in temperature at the exit plane is more extensive than a typical gas-turbine combustor [142] and should be considered for downstream component design. As explained in Section 5.2.1 the URANS results also overpredict the mean temperature by ~200 K, primarily due to an offset in the location of the RCARS probe volume downstream of the simulated exit plane. Nonetheless, these profiles show a relatively small azimuthal variation in the exit flow temperatures due to product gas mixing.

Given the azimuthal temperature distributions, experimental and simulated combustor pattern factors can be estimated for the RDC. The combustor pattern factor is a non-dimensional number providing information on the product gas quality exiting the combustor in gas-turbine engines [142]. The pattern factor is defined as $PF = (T_3^{max} - T_3^{mean}) / (T_3^{mean} - T_2^{mean})$, where 2 and 3 correspond to the combustor inlet and exit locations. Ideally, the pattern factor is expected to be close to zero to have a uniform temperature profile at the exhaust. However, in practice, local flame conditions and turbulence leads to values greater than zero. For annular combustors, the PF value is dependent on the combustor length/diameter aspect ratio and the pressure loss factor. Modern gas turbine annular combustors have PF values in the range of 0.1 – 0.3 [142]. Prior work by Naples *et al.* provided an RDC PF value of 0.25 – 0.3 [91]. For the baseline condition (T_2^{mean} = 300 K), the PF for this RDC from the experiment is $PF_{Exp.}$ = 0.19 and for simulations is PF_{CFD} = 0.20. These values suggest that the inherent annular construction and aspect ratio of this RDC provides sufficiently mixed product gas resulting in PF values close to modern gas-turbine combustors. The reported PF precision is an improvement from that previously reported using thermocouples [91].

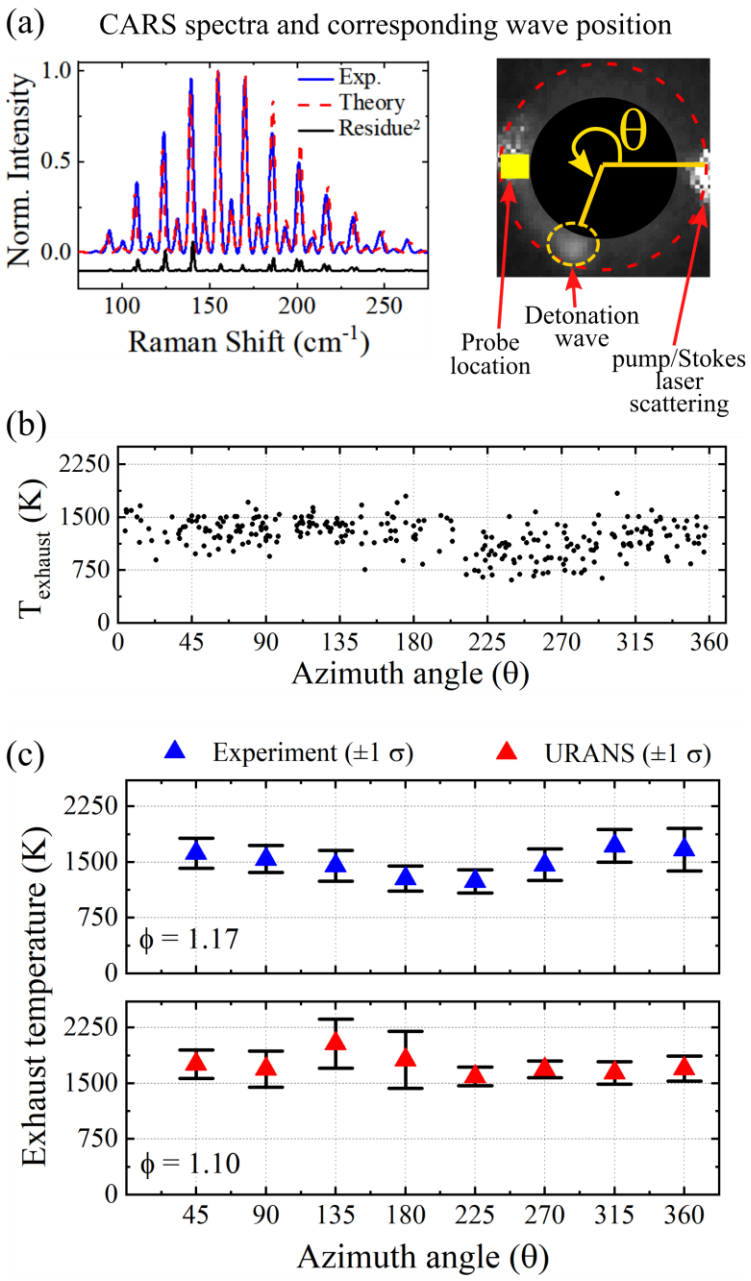

Figure 7.11: (a) Spectral fit for CARS temperature at 2070 K and the corresponding exhaust plume detonation wave position determined by azimuth angle θ. (b) Measured temperature distribution vs azimuthal position for case 1 over the entire 1 second duration (c) Azimuthal temperature profile at the baseline condition from experiments and URANS simulations.

7.8 Conclusions

Thermometry using hybrid fs/ps N_2 rotational CARS was performed at the exhaust of a non-premixed hydrogen-air RDC at 1 kHz repetition rate. The RDC was operated with an air throat mass flux of 750 kg/m^2/s and global equivalence ratios of 1.17, 1.68, and 2.12 to have minimal oxygen line interference in the resultant N_2 RCARS spectra for initial evaluation of this approach. The equivalence ratio of 1.17 was selected as the baseline condition. At this condition, complementary URANS simulations were performed on a ~48.5 million structured grid with boundary layer mesh refinement and a single-step chemistry model that was used in prior studies of hydrogen-air RDCs. Results from the model were compared with the experimental temperature measurements.

An extensive theoretical analysis was performed for the applicability of thermometry measurements in the RDC environment. Data from the URANS simulations were used to estimate the exhaust plane spatial temperature and pressure distributions. Bias errors and the effects of pressure, temperature, and probe volume length on the precision, sensitivity, SNR, and dynamic range were investigated. This characterization showed that the RCARS probe volume with a spatial extent of 700 μm induces uncertainties of <2% in temperature. Hence, this approach achieves sufficient spatial resolution (~700 μm) and high temporal resolution (20 ps). The kHz rate CARS instrument has a probe pulse amplification system that allows for temperature sensitivity over a dynamic range spanning the 800–2600 K variation of temperature in the RDC exhaust.

A high-speed camera was synchronized with the CARS instrument to capture the detonation wave position during the temperature measurement to map the azimuthal distribution of temperatures. The histogram of temperature obtained at the three operating conditions showed a skew-normal distribution with longer tails near the high-temperature zone attributed to high-temperature transients from unmixed products of the detonation wave. The CFD exhaust temperature histogram also had an analogous skew-normal distribution with a mean-shift in the higher temperature than the experimental results due to gas expansion at the RDC exit as well as heat losses. The experimental and computational profiles obtained in eight sectors along the azimuth allude to a sufficiently mixed product gas composition with a maximum mean-temperature variation of ~300 K. The combustor pattern factor for this RDC was estimated to be ~0.19, a nominal value compared with conventional constant-pressure gas turbine combustors.

Future work for RCARS thermometry includes (i) performing 1-D line-RCARS measurements and (ii) simultaneous measurement of O_2 and H_2 species for combustor performance evaluation. In combination with velocimetry techniques in the exhaust, the azimuthal temperature profile can also be used to describe the speed of sound at the exit plane and obtain corresponding Mach numbers for design of combustor transition and downstream components. Improvements in modelling at higher pressures may be needed to perform RCARS measurements in the interior of the RDC at conditions relevant for propulsion and power generation systems. The design and implementation of RCARS, including selection of the beam-crossing angle and probe volume dimensions, will also need to be considered within the interior of the RDC where the property gradients and fluctuations are significantly higher than in the exhaust.

8. SUMMARY AND FUTURE WORK

8.1 Summary

This research presented in this dissertation showcases the development and application high repetition rate qualitative and quantitative diagnostics in a modular and optically accessible RDC test platform to understand the physics of rotating detonations in non-premixed injection schemes. A novel optical RDC was designed, developed, assembled, and commissioned with the goal of having a modular combustor with optical access through the injection system and the combustion chamber.

The first set of qualitative measurements using MHz rate broadband chemiluminescence show the details of propagating detonation waves in non-premixed hydrogen air systems. These experiments revealed the presence of axial variation in detonation strength, marked by varying chemiluminescence intensity along the axial length. This variation is inherently dependent on the mixing effectiveness of the reactant ahead of the detonation wave. The wave height and axial luminosity variations from the injection nearfield to the injection far field also showed a non-linear scaling with increasing mass flux. In addition to the leading detonation wave, a trailing detonation wave was observed that warranted further exploration as to the source of the trailing detonation wave.

In order to understand the radial characteristics of the detonation wave, simultaneous MHz rate OH* chemiluminescence and OH PLIF was performed to indicate the presence of azimuthal reflected shock detonation, marked by a flame front less than 1.5 mm thick. These results not only confirm the axial variation in detonation, but it also shows the trailing combustion wave is indeed a detonation wave.

With the advent of high repetition rate imaging, Maximum Intensity Projection and sum-of-correlation PIV methods were used in parallel to understand the cellular propagation of detonations in non-premixed RDCs. The stratified reactant flow made the increasing cell sizes with increasing axial distance from the injection plane.

After completion of the backward facing step combustor characterization, an expanding annular channel, forming a ramp from the injection plane, was developed. Through the use of chemiluminescence and PLIF, the ramp was shown to perform at lower C-J speeds for the same

operating conditions due to the absence of the backward facing step. In addition to the wave speed dropping, the ramp design also had a leading freely propagating detonation with multiple trailing shock induced detonation waves in its wake. This trailing shock system can be explained by the presence of confinement, which minimizes reactant gas mixing and forms the trailing combustion systems.

Lastly, CARS thermometry was performed on the exhaust of the RDC to obtain a quantitative metric on the exhaust profile. These results were compared with the URANS simulations leading to good agreement in the experiments and CFD on the combustor pattern factor for RDCs.

8.2 Future work

The novel RDC test-platform is modular in nature and provides an excellent avenue for further research in the pressure gain combustion research area. The following areas are of immediate interest and would benefit from further investigation:

- Simultaneous MHz OH* and OH-PLIF in the ramp configuration to understand the structure of the trailing shock induced detonation waves.
- Combined use of Femtosecond-laser activation and sensing of hydroxyl (FLASH) tagging and fs/ps RCARS thermometry to obtain exhaust Mach number profiles across the azimuth.
- Vary the fuel composition to incorporate dilution in the fuel circuit to understand the effect of cooling and reformation technologies for carbon-free fuel injection of liquids such as ammonia.
- Vary the swirl in the air injection stream to understand the effect of induced azimuthal momentum on detonation propagation direction dependence.
- Incorporate higher temperature and pressures of the propellants to take the RDC into conditions relevant to stationary power generation gas turbines and rocket engines.
- Incorporate liquid injection systems in THOR for understanding spray breakup processes in detonating environment.
- Perform integrated turbine and compressor testing to study cycle level performance of RDCs for gas turbine applications.

- Studies on thermal heat load on the surface of the RDC using high temperature phosphor-based thermometry to design and develop cooling strategies for continuous operation of the RDC.

REFERENCES

[1] M. Hishida, T. Fujiwara, P. Wolanski, Fundamentals of rotating detonations, Shock Waves 19 (2009) 1–10.

[2] K. Kailasanath, Review of propulsion applications of detonation waves, AIAA J. 38 (2000) 1698–1708.

[3] F.A. Bykovskii, S.A. Zhdan, E.F. Vedernikov, Continuous spin detonations, J. Propuls. Power 22 (2006) 1204–1216.

[4] V. Anand, E. Gutmark, Rotating detonation combustors and their similarities to rocket instabilities, Prog. Energy Combust. Sci. 73 (2019) 182–234.

[5] B.A. Rankin, C.A. Fugger, D.R. Richardson, K.Y. Cho, J.L. Hoke, A.W. Caswell, et al., Evaluation of Mixing Processes in a Non-Premixed Rotating Detonation Engine Using Acetone PLIF Imaging n.d., https://doi.org/10.2514/6.2016-1198.

[6] H.Y. Peng, W.D. Liu, S.J. Liu, H.L. Zhang, W.Y. Zhou, Realization of methane-air continuous rotating detonation wave, Acta Astronaut. 164 (2019) 1–8.

[7] P. Wolański, Detonative propulsion, Proc. Combust. Inst. 34 (2013) 125–158.

[8] S.M. Frolov, V.S. Aksenov, V.S. Ivanov, Experimental proof of Zel'dovich cycle efficiency gain over cycle with constant pressure combustion for hydrogen-oxygen fuel mixture, Int. J. Hydrogen Energy 40 (2015) 6970–6975.

[9] Z. Liu, J. Braun, G. Paniagua, Characterization of a Supersonic Turbine Downstream of a Rotating Detonation Combustor, J. Eng. Gas Turbines Power 141 (2018) 031501.

[10] W.H. Heiser, D.T. Pratt, Thermodynamic cycle analysis of pulse detonation engines, J. Propuls. Power 18 (2002) 68–76.

[11] B.A. Rankin, D.R. Richardson, A.W. Caswell, A.G. Naples, J.L. Hoke, F.R. Schauer, Chemiluminescence imaging of an optically accessible non-premixed rotating detonation engine, Combust. Flame 176 (2017) 12–22.

[12] C.S. Goldenstein, C.A. Almodóvar, J.B. Jeffries, R.K. Hanson, C.M. Brophy, High-bandwidth scanned-wavelength-modulation spectroscopy sensors for temperature and H2O in a rotating detonation engine, Meas. Sci. Technol. 25 (2014) .

[13] V. Anand, A. St. George, R. Driscoll, E. Gutmark, Investigation of rotating detonation combustor operation with H2-Air mixtures, Int. J. Hydrogen Energy 41 (2016) 1281–1292.

[14] J. Tobias, D. Depperschmidt, C. Welch, R. Miller, M. Uddi, A.K. Agrawal, et al., OH∗ chemiluminescence imaging of the combustion products from a methane-fueled rotating detonation engine, J. Eng. Gas Turbines Power 141 (2019) .

[15] D.P. Stechmann, S. Sardeshmukh, S.D. Heister, K. Mikoshiba, Role of Ignition Delay in Rotating Detonation Engine Performance and Operability, J. Propuls. Power 35 (2019) 125–140.

[16] V. Athmanathan, J.M. Fisher, Z.M. Ayers, D.G. Cuadrado, V. Andreoli, J. Braun, et al.,Turbine-integrated High-pressure Optical RDE (THOR) for injection and detonation dynamics assessment. AIAA Propuls. Energy 2019 Forum, American Institute of Aeronautics and Astronautics (AIAA) (2019) .

[17] F. Chacon, M. Gamba,Development of an optically accessible continuous wave rotating detonation engine. 2018 Jt. Propuls. Conf., [publishername] American Institute of Aeronautics and Astronautics Inc, AIAA (2018) .

[18] H. Nakayama, J. Kasahara, A. Matsuo, I. Funaki, Front shock behavior of stable curved detonation waves in rectangular-cross-section curved channels, Proc. Combust. Inst. 34 (2013) 1939–1947.

[19] K. Schwinn, R. Gejji, B. Kan, S. Sardeshmukh, S. Heister, C.D. Slabaugh, Self-sustained, high-frequency detonation wave generation in a semi-bounded channel, Combust. Flame 193 (2018) 384–396.

[20] J.R. Burr, K. Yu,Detonation Wave Propagation in Cross-Flow of Discretely Spaced Reactant Jets, American Institute of Aeronautics and Astronautics (AIAA) (2017) .

[21] J.R. Burr, K.H. Yu, Experimental characterization of RDE combustor flowfield using linear channel, Proc. Combust. Inst. 37 (2019) 3471–3478.

[22] W.S. Anderson, S.D. Heister,Response of a liquid jet in a multiple-detonation driven crossflow. J. Propuls. Power, vol. 35, American Institute of Aeronautics and Astronautics Inc. (2019) , p. 303–312.

[23] C. Bedick, A. Sisler, D. Ferguson, P. Strakey, A. Nix, D. Billips, Development of a Lab-Scale Experimental Testing Platform for Rotating Detonation Engine Inlets n.d., https://doi.org/10.2514/6.2017-0785.

[24] R.Z.J. Wang, Numerical investigation of shock wave reflections near the head ends of rotating detonation engines (2013) 461–472, https://doi.org/10.1007/s00193-013-0440-0.

[25] J. Braun, B.H. Saracoglu, G. Paniagua, Unsteady Performance of Rotating Detonation Engines with Different Exhaust Nozzles, J. Propuls. Power 33 (2017) 121–130.

[26] V.R. Katta, K.Y. Cho, J.L. Hoke, J.R. Codoni, F.R. Schauer, W.M. Roquemore, Effect of increasing channel width on the structure of rotating detonation wave, Proc. Combust. Inst. 37 (2019) 3575–3583.

[27] C.A. Nordeen, D. Schwer, F. Schauer, J. Hoke, T. Barber, B. Cetegen, Thermodynamic model of a rotating detonation engine, Combust. Explos. Shock Waves 50 (2014) 568–577.

[28] H. Peng, W. Liu, S. Liu, Ethylene Continuous Rotating Detonation in optically accessible racetrack-like combustor, Combust. Sci. Technol. (2018) , https://doi.org/10.1080/00102202.2018.1498850.

[29] B.A. Rankin, J.R. Codoni, K.Y. Cho, J.L. Hoke, F.R. Schauer, Investigation of the structure of detonation waves in a non-premixed hydrogen – air rotating detonation engine using mid-infrared imaging, Proc. Combust. Inst. 37 (2019) 3479–3486.

[30] J. Sousa, J. Braun, G. Paniagua, Development of a fast evaluation tool for rotating detonation combustors, Appl. Math. Model. 52 (2017) 42–52.

[31] R.W. Miller, W.F.Z. Lee, C.J. Gomez, Measurement of Gas flow via critical flow venturis, ASME (1984) .

[32] R.W.W. Schefer, W.D.D. Kulatilaka, B.D.D. Patterson, T.B.B. Settersten, Visible emission of hydrogen flames, Combust. Flame 156 (2009) 1234–1241.

[33] D. Schwer, K. Kailasanath, Numerical investigation of the physics of rotating-detonation-engines, Proc. Combust. Inst. 33 (2011) 2195–2202.

[34] S.M. Frolov, V.S. Aksenov, V.S. Ivanov, I.O. Shamshin, Large-scale hydrogen-air continuous detonation combustor, Int. J. Hydrogen Energy 40 (2015) 1616–1623.

[35] D. Schwer, K. Kailasanath, Fluid dynamics of rotating detonation engines with hydrogen and hydrocarbon fuels, Proc. Combust. Inst. 34 (2013) 1991–1998.

[36] Y.T. Shao, M. Liu, J.P. Wang, Numerical investigation of rotating detonation engine propulsive performance, Combust. Sci. Technol. 182 (2010) 1586–1597.

[37] T.H. Yi, J. Lou, C. Turangan, J.Y. Choi, P. Wolanski, Propulsive performance of a continuously rotating detonation engine, J. Propuls. Power 27 (2011) 171–181.

[38] K. Mikoshiba, S. V. Sardeshmukh, S.D. Heister, On the response of annular injectors to rotating detonation waves, Shock Waves (2019) , https://doi.org/10.1007/s00193-019-00900-8.

[39] H. Wen, Q. Xie, B. Wang, Propagation behaviors of rotating detonation in an obround combustor, Combust. Flame 210 (2019) 389–398.

[40] M.D. Bohon, R. Bluemner, C.O. Paschereit, E.J. Gutmark, Measuring Rotating Detonation Combustion Using Cross-Correlation, Flow, Turbul. Combust. 103 (2019) 271–292.

[41] A.C. Eckbreth,Laser diagnostics for combustion temperature and species. Gordon and Breach Publishers (1996) .

[42] S. Krishna, R. V. Ravikrishna, Quantitative OH Planar Laser Induced Fluorescence Diagnostics of Syngas and Methane Combustion in a Cavity Combustor, Combust. Sci. Technol. 187 (2015) 1661–1682.

[43] D.R. Richardson, N. Jiang, D.L. Blunck, J.R. Gord, S. Roy, Characterization of inverse diffusion flames in vitiated cross flows via two-photon planar laser-induced fluorescence of CO and 2-D thermometry, Combust. Flame 168 (2016) 270–285.

[44] P.M. Danehy, P. Mere, M.J. Gaston, S. O'Byrne, P.C. Palma, A.F. Houwing, Fluorescence velocimetry of the hypersonic, separated flow over a cone, AIAA J. 39 (2001) 1320–1328.

[45] B.R. Halls, D.J. Thul, D. Michaelis, S. Roy, T.R. Meyer, J.R. Gord, Single-shot, volumetrically illuminated, three-dimensional, tomographic laser-induced-fluorescence imaging in a gaseous free jet, Opt. Express 24 (2016) 10040.

[46] S.W. Grib, P.S. Hsu, N. Jiang, J.J. Felver, S.A. Schumaker, C.D. Carter, et al., 100 kHz krypton planar laser-induced fluorescence imaging, Opt. Lett. 45 (2020) 3832.

[47] N. Jiang, M. Webster, W.R. Lempert, J.D. Miller, T.R. Meyer, C.B. Ivey, et al., MHz-rate nitric oxide planar laser-induced fluorescence imaging in a Mach 10 hypersonic wind tunnel, Appl. Opt. 50 (2011) A20–A28.

[48] J.R. Gord, J.D. Miller, M. Slipchenko, N. Jiang, T.R. Meyer, W.R. Lempert, Ultrahigh-frame-rate OH fluorescence imaging in turbulent flames using a burst-mode optical parametric oscillator, Opt. Lett. Vol. 34, Issue 9, Pp. 1309-1311 34 (2009) 1309–1311.

[49] Z. Wang, P. Stamatoglou, B. Zhou, M. Aldén, X.S. Bai, M. Richter, Investigation of OH and CH2O distributions at ultra-high repetition rates by planar laser induced fluorescence imaging in highly turbulent jet flames, Fuel 234 (2018) 1528–1540.

[50] C. Carter, C. Wuensche, S. Hammack, T. Lee, Continuous hydroxyl radical planar laser imaging at 50 kHz repetition rate, Appl. Opt. Vol. 53, Issue 23, Pp. 5246-5251 53 (2014) 5246–5251.

[51] V. Athmanathan, J. Braun, Z. Ayers, J. Fisher, C. Fugger, S. Roy, et al.,Detonation structure evolution in an optically-accessible non-premixed H2-air RDC using MHz rate imaging. AIAA Scitech 2020 Forum, Orlando, Florida American Institute of Aeronautics and Astronautics (2020) .

[52] C. Brackmann, J. Sjöholm, J. Rosell, M. Richter, J. Bood, M. Aldén, Picosecond excitation for reduction of photolytic effects in two-photon laser-induced fluorescence of CO, Proc. Combust. Inst. 34 (2013) 3541–3548.

[53] S. Roy, P.S. Hsu, N. Jiang, M.N. Slipchenko, J.R. Gord, 100-kHz-rate gas-phase thermometry using 100-ps pulses from a burst-mode laser, Opt. Lett. 40 (2015) 5125.

[54] F. Chacon, M. Gamba, OH PLIF Visualization of an Optically Accessible Rotating Detonation Combustor (2019) .

[55] J. Felver, M.N. Slipchenko, E.L. Braun, T.R. Meyer, S. Roy, High-energy laser pulses for extended duration megahertz-rate flow diagnostics, Opt. Lett. 45 (2020) 4583.

[56] L.F. K., B.E. M., Rotating Detonation Wave Propulsion: Experimental Challenges, Modeling, and Engine Concepts, J. Propul. Power 30 n.d.1125–1142.

[57] T. Sato, F. Chacon, L. White, V. Raman, M. Gamba, Mixing and detonation structure in a rotating detonation engine with an axial air inlet, Proc. Combust. Inst. (2020) , https://doi.org/10.1016/j.proci.2020.06.283.

[58] S. Jin, L. Qi, N. Zhao, H. Zheng, Q. Meng, J. Yang, ScienceDirect Experimental and numerical research on rotating detonation combustor under non-premixed conditions, Int. J. Hydrogen Energy 45 (2019) 10176–10188.

[59] D. Dausen, C. Brophy, R. Wright, J. Marder,Design of an Optically-Accessible Rotating Detonation Engine. 48th AIAA/ASME/SAE/ASEE Jt. Propuls. Conf. & Exhib., Reston, Virigina American Institute of Aeronautics and Astronautics (2012) .

[60] C.A. Fugger, K.Y. Cho, J. Hoke, M. Gomez Gomez, T.R. Meyer, S.A. Schumaker, et al.,Detonation Dynamics Visualization From Megahertz Imaging, American Institute of Aeronautics and Astronautics (AIAA) (2020) .

[61] K. Matsuoka, M. Tanaka, T. Noda, A. Kawasaki, J. Kasahara, Experimental investigation on a rotating detonation cycle with burned gas backflow, Combust. Flame 225 (2021) 13–19.

[62] P.S. Hsu, M.N. Slipchenko, N. Jiang, C.A. Fugger, A.M. Webb, V. Athmanathan, et al., Megahertz-rate OH planar laser-induced fluorescence imaging in a rotating detonation combustor, Opt. Lett. 45 (2020) .

[63] L.R. Boeck, F.M. Berger, J. Hasslberger, T. Sattelmayer, Detonation propagation in hydrogen–air mixtures with transverse concentration gradients, Shock Waves 26 (2016) 181–192.

[64] K. Ishii, M. Kojima, Behavior of detonation propagation in mixtures with concentration gradients, Shock Waves 17 (2007) 95–102.

[65] F. Ettner, K.G. Vollmer, T. Sattelmayer, Mach reflection in detonations propagating through a gas with a concentration gradient, Shock Waves 23 (2013) 201–206.

[66] Gaseous Detonations : their nature , effects and control. 1st ed. New York Chapman & Hall (1987) .

[67] C.A. Nordeen, D. Schwer, F. Schauer, J. Hoke, T. Barber, B.M. Cetegen, Role of inlet reactant mixedness on the thermodynamic performance of a rotating detonation engine, Shock Waves 26 (2016) 417–428.

[68] M. Zhao, M.J. Cleary, H. Zhang, Combustion mode and wave multiplicity in rotating detonative combustion with separate reactant injection, Combust. Flame 225 (2021) 291–304.

[69] M. Zhao, J.M. Li, C.J. Teo, B.C. Khoo, H. Zhang, Effects of Variable Total Pressures on Instability and Extinction of Rotating Detonation Combustion, Flow, Turbul. Combust. 104 (2020) 261–290.

[70] J. Sun, J. Zhou, S. Liu, Z. Lin, J. Cai, Effects of injection nozzle exit width on rotating detonation engine, Acta Astronaut. 140 (2017) 388–401.

[71] C.A. Fugger, P.S. Hsu, N. Jiang, S. Roy, M.N. Slipchenko, V. Athmanathan, et al.,Megahertz oh-plif imaging in a rotating detonation engine. AIAA Scitech 2021 Forum, (2021) .

[72] S. Chakravarthy, O. Peroomian, U. Goldberg, S. Palaniswamy,The CFD++ computational fluid dynamics software suite. AIAA SAE World Aviat. Conf. 1998, American Institute of Aeronautics and Astronautics Inc. (1998) .

[73] J. Braun, G. Paniagua, F. Falempin, B. Le Naour, Design and Experimental Assessment of Bladeless Turbines for Axial Inlet Supersonic Flows, J. Eng. Gas Turbines Power 142 (2020) .

[74] S.M. Frolov, A. V. Dubrovskii, V.S. Ivanov,Three-dimensional numerical simulation of operation process in rotating detonation engine. Prog. Propuls. Phys., vol. 4, Les Ulis, France EDP Sciences (2013) , p. 467–488.

[75] S. Gordon, B.J. McBride, F.J. Zeleznik, Computer Program for Calculation of Complex Chemical Equilibrium Compositions and Applications, NASA Ref. Publ. 1311 (1996) .

[76] V. Rodriguez, C. Jourdain, P. Vidal, R. Zitoun, An experimental evidence of steadily-rotating overdriven detonation, Combust. Flame 202 (2019) 132–142.

[77] D.T. Pratt, J.W. Humphrey, D.E. Glenn, Morphology of standing oblique detonation waves, J. Propuls. Power 7 (1991) 837–845.

[78] C.M. Guirao, R. Knystautas, J.H. Lee, W. Benedick, M. Berman, Hydrogen-air detonations, Symp. Combust. 19 (1982) 583–590.

[79] G. Ciccarelli, T. Ginsberg, J. Boccio, C. Economos, K. Sato, M. Kinoshita, Detonation cell size measurements and predictions in hydrogen-air-steam mixtures at elevated temperatures, Combust. Flame 99 (1994) 212–220.

[80] K. Kailasanath,Recent Developments in the Research on Pressure-Gain Combustion Devices. In: Gupta AK, De A, Aggarwal SK, Kushari A, Runchal A, editors. Innov. Sustain. Energy Clean. Environ., Singapore Springer Singapore (2020) , p. 3–21, https://doi.org/10.1007/978-981-13-9012-8_1.

[81] J. Jodele, A. Zahn, V. Anand, E. Gutmark, OH * Chemiluminescence Investigation of Rotating Detonation Wave Structure (2019) 1–7.

[82] M.I. Radulescu, A detonation paradox: Why inviscid detonation simulations predict the incorrect trend for the role of instability in gaseous cellular detonations?, Combust. Flame 195 (2018) 151–162.

[83] V. Athmanathan, Z. Ayers, J.M. Fisher, J. Braun, G. Paniagua, C.A. Fugger, et al.,MHz rate imaging of detailed detonation structure in a nonpremixed Hydrogen-air rotating detonation combustor. (2019) .

[84] J.M. Austin, F. Pintgen, J.E. Shepherd, Reaction zones in highly unstable detonations, Proc. Combust. Inst. 30 (2005) 1849–1857.

[85] R.A. Strehlow, R. Liaugminas, R.H. Watson, J.R. Eyman,Transverse wave structure in detonations. Symp. Combust., vol. 11, (1967) , p. 683–692.

[86] J. Westerweel, Fundamentals of digital particle image velocimetry, Meas. Sci. Technol. 8 (1997) 1379–1392.

[87] J.A.C. Kentfield, Thermodynamics of airbreathing pulse-detonation engines, J. Propuls. Power 18 (2002) 1170–1175.

[88] E. Wintenberger, J.E. Shepherd, Introduction to "To the Question of Energy Use of Detonation Combustion" By Ya. B. Zel'dovich, J. Propuls. Power 22 (2006) 586–587.

[89] P. Wolański, Application of the Continuous Rotating Detonation to Gas Turbine, Appl. Mech. Mater. 782 (2015) 3–12.

[90] S. Zhou, H. Ma, C. Liu, C. Zhou, D. Liu, Experimental investigation on the temperature and heat-transfer characteristics of rotating-detonation-combustor outer wall, Int. J. Hydrogen Energy 43 (2018) 21079–21089.

[91] A. Naples, J. Hoke, R. Battelle, F. Schauer, T63 Turbine Response to Rotating Detonation Combustor Exhaust Flow, J. Eng. Gas Turbines Power 141 (2019) 021029.

[92] F.A. Bykovskii, E.F. Vedernikov, Heat fluxes to combustor walls during continuous spin detonation of fuel-air mixtures, Combust. Explos. Shock Waves 45 (2009) 70–77.

[93] S.W. Theuerkauf, F.R. Schauer, R. Anthony, J.L. Hoke,Average and instantaneous heat release to the walls of an RDE. 52nd Aerosp. Sci. Meet., American Institute of Aeronautics and Astronautics Inc. (2014) .

[94] Z. Liu, G. Paniagua, Design of Directional Probes for High-Frequency Turbine Measurements, J. Eng. Gas Turbines Power 140 (2017) 011601.

[95] J. Kindracki, Temperature Measurements in the Detonation Chamber Supplied by Air from Centrifugal Compressor and Gaseous Hydrogen, Trans. Aerosp. Res. 2017 (2019) 7–23.

[96] L. Villafañe, G. Paniagua, Aero-thermal analysis of shielded fine wire thermocouple probes, Int. J. Therm. Sci. 65 (2013) 214–223.

[97] K. Muraleetharan, M.D. Polanka, L.P. Goss, R. Huff,Temperature response of rotating detonations using thin-filament pyrometry. AIAA Propuls. Energy 2020 Forum, (2020) , p. 1–13.

[98] A.P. Nair, D.D. Lee, D.I. Pineda, J. Kriesel, W.A. Hargus, J.W. Bennewitz, et al., MHz laser absorption spectroscopy via diplexed RF modulation for pressure, temperature, and species in rotating detonation rocket flows, Appl. Phys. B Lasers Opt. 126 (2020) 138.

[99] K.D. Rein, S. Roy, S.T. Sanders, A.W. Caswell, F.R. Schauer, J.R. Gord, Measurements of gas temperatures at 100 kHz within the annulus of a rotating detonation engine, Appl. Phys. B Lasers Opt. 123 (2017) .

[100] W.Y. Peng, S.J. Cassady, C.L. Strand, C.S. Goldenstein, R.M. Spearrin, C.M. Brophy, et al., Single-ended mid-infrared laser-absorption sensor for time-resolved measurements of water concentration and temperature within the annulus of a rotating detonation engine, Proc. Combust. Inst. 37 (2019) 1435–1443.

[101] S. Roy, J.R. Gord, A.K. Patnaik, Recent advances in coherent anti-Stokes Raman scattering spectroscopy: Fundamental developments and applications in reacting flows, Prog. Energy Combust. Sci. 36 (2010) 280–306.

[102] P.J. Wrzesinski, H.U. Stauffer, W.D. Kulatilaka, J.R. Gord, S. Roy, Time-resolved femtosecond CARS from 10 to 50 Bar: Collisional sensitivity, J. Raman Spectrosc. 44 (2013) 1344–1348.

[103] T. Lang, M. Motzkus, Single-shot femtosecond coherent anti-Stokes Raman-scattering thermometry, J. Opt. Soc. Am. B 19 (2002) 340.

[104] J.D. Miller, S. Roy, M.N. Slipchenko, J.R. Gord, T. Meyer, rotational hybrid femtosecond / picosecond coherent anti-Stokes Raman scattering, Opt. Express 19 (2011) 15627–15640.

[105] D.R. Richardson, R.P. Lucht, W.D. Kulatilaka, S. Roy, J.R. Gord, Theoretical modeling of single-laser-shot, chirped-probe-pulse femtosecond coherent anti-Stokes Raman scattering thermometry, Appl. Phys. B Lasers Opt. 104 (2011) 699–714.

[106] J.D. Miller, C.E. Dedic, S. Roy, J.R. Gord, T.R. Meyer, Interference-free gas-phase thermometry at elevated pressure using hybrid femtosecond/picosecond rotational coherent anti-Stokes Raman scattering, Opt. Express 20 (2012) 5003.

[107] H.U. Stauffer, K.A. Rahman, M.N. Slipchenko, S. Roy, J.R. Gord, T.R. Meyer, Interference-free hybrid fs/ps vibrational CARS thermometry in high-pressure flames, Opt. Lett. 43 (2018) 4911.

[108] A. Bohlin, F. Vestin, P. Joubert, J. Bonamy, P.E. Bengtsson, Improvement of rotational CARS thermometry in fuel-rich hydrocarbon flames by inclusion of N2;-H2; Raman line widths, J. Raman Spectrosc. 40 (2009) 788–794.

[109] F. Vestin, M. Afzelius, P.E. Bengtsson, Improved species concentration measurements using a species-specific weighting procedure on rotational CARS spectra, J. Raman Spectrosc. 36 (2005) 95–101.

[110] A.D. Cutler, L.M.L. Cantu, E.C.A. Gallo, R. Baurle, P.M. Danehy, R. Rockwell, et al., Nonequilibrium supersonic freestream studied using coherent anti-stokes Raman spectroscopy, AIAA J. 53 (2015) 2762–2770.

[111] G. Magnotti, A.D. Cutler, G.C. Herring, S.A. Tedder, P.M. Danehy, Saturation and Stark broadening effects in dual-pump CARS of N2, O2, and H2, J. Raman Spectrosc. 43 (2012) 611–620.

[112] R.J. Hall, L.R. Boedeker, CARS thermometry in fuel-rich combustion zones, Appl. Opt. 23 (1984) 1340.

[113] B. Lavorel, H. Tran, E. Hertz, O. Faucher, P. Joubert, M. Motzkus, et al., Femtosecond Raman time-resolved molecular spectroscopy, Comptes Rendus Phys. 5 (2004) 215–229.

[114] A.C. Eckbreth, T.J. Anderson, Dual broadband CARS for simultaneous, multiple species measurements, Appl. Opt. 24 (1985) 2731.

[115] S.P. Kearney, Hybrid fs/ps rotational CARS temperature and oxygen measurements in the product gases of canonical flat flames, Combust. Flame 162 (2014) 1748–1758.

[116] F. Vestin, D. Sedarsky, R. Collin, M. Aldén, M. Linne, P.E. Bengtsson, Rotational coherent anti-Stokes Raman spectroscopy (CARS) applied to thermometry in high-pressure hydrocarbon flames, Combust. Flame 154 (2008) 143–152.

[117] T.L. Courtney, N.T. Mecker, B.D. Patterson, M. Linne, C.J. Kliewer, Hybrid femtosecond/picosecond pure rotational anti-Stokes Raman spectroscopy of nitrogen at high pressures (1-70 atm) and temperatures (300-1000 K), Appl. Phys. Lett. 114 (2019) 101107.

[118] A. Bohlin, B.D. Patterson, C.J. Kliewer, Communication: Simplified two-beam rotational CARS signal generation demonstrated in 1D, J. Chem. Phys. 138 (2013) .

[119] A. Bohlin, C.J. Kliewer, Communication: Two-dimensional gas-phase coherent anti-Stokes Raman spectroscopy (2D-CARS): Simultaneous planar imaging and multiplex spectroscopy in a single laser shot, J. Chem. Phys. 138 (2013) .

[120] M. Schenk, T. Seeger, A. Leipertz, Simultaneous and time-resolved temperature and relative CO 2-N2 and O2-CO2-N2 concentration measurements with pure rotational coherent anti-Stokes Raman scattering for pressures as great as 5 MPa, Appl. Opt. 44 (2005) 5582–5593.

[121] F. Vestin, P.E. Bengtsson, Rotational CARS for simultaneous measurements of temperature and concentrations of N2, O2, CO, and CO2 demonstrated in a CO/air diffusion flame, Proc. Combust. Inst. 32 (2009) 847–854.

[122] F. Grisch, M. Péalat, P. Bouchardy, J.P. Taran, I. Bar, D. Heflinger, et al., Real time diagnostics of detonation products from lead azide using coherent anti-Stokes Raman scattering, Appl. Phys. Lett. 59 (1991) 3516–3518.

[123] S. Roy, N. Jiang, H.U. Stauffer, J.B. Schmidt, W.D. Kulatilaka, T.R. Meyer, et al., Spatially and temporally resolved temperature and shock-speed measurements behind a laser-induced blast wave of energetic nanoparticles, J. Appl. Phys. 113 (2013) 184310.

[124] C.E. Dedic, J.B. Michael, T.R. Meyer,Investigation of energy distributions behind a microscale gas-phase detonation tube using hybrid fs/ps coherent anti-Stokes Raman scattering. AIAA SciTech Forum - 55th AIAA Aerosp. Sci. Meet., American Institute of Aeronautics and Astronautics Inc. (2017) .

[125] D.R. Richardson, S.P. Kearney, D.R. Guildenbecher, Post-detonation fireball thermometry via femtosecond-picosecond coherent anti-Stokes Raman Scattering (CARS), Proc. Combust. Inst. (2020) , https://doi.org/10.1016/j.proci.2020.06.257.

[126] J.D. Miller, M.N. Slipchenko, T.R. Meyer, H.U. Stauffer, J.R. Gord, Hybrid femtosecond / picosecond coherent anti-Stokes Raman scattering for high-speed gas-phase thermometry, Opt. Lett. 35 (2010) 2430–2432.

[127] J.D. Miller, M.N. Slipchenko, T.R. Meyer, Probe-pulse optimization for nonresonant suppression in hybrid fs/ps coherent anti-Stokes Raman scattering at high temperature, Opt. Express 19 (2011) 13326.

[128] H.U. Stauffer, J.D. Miller, S. Roy, J.R. Gord, T.R. Meyer, Communication: Hybrid femtosecondpicosecond rotational coherent anti-Stokes Raman scattering thermometry using a narrowband time-asymmetric probe pulse, J. Chem. Phys. 136 (2012) 111101.

[129] S.P. Kearney, D.J. Scoglietti, C.J. Kliewer, Hybrid femtosecond/picosecond rotational coherent anti-Stokes Raman scattering temperature and concentration measurements using two different picosecond-duration probes, Opt. Express 21 (2013) 12327.

[130] M. Scherman, M. Nafa, T. Schmid, A. Godard, A. Bresson, B. Attal-Tretout, et al., Rovibrational hybrid fs/ps CARS using a volume Bragg grating for N2 thermometry, Opt. Lett. 41 (2016) 488.

[131] S.P. Kearney, D.J. Scoglietti, Hybrid fs/ps rotational coherent anti-Stokes Raman scattering at flame temperatures using a second-harmonic bandwidth-compressed probe, Opt. Lett. 38 (2013) 833–835.

[132] R. Santagata, M. Scherman, M. Toubeix, M. Nafa, B. Tretout, A. Bresson, et al., Ultrafast background-free ro-vibrational fs / ps-CARS thermometry using an Yb : YAG crystal-fiber amplified probe, Opt. Express 27 (2019) 32924–32937.

[133] K.A. Rahman, E.L. Braun, M.N. Slipchenko, S. Roy, T.R. Meyer, Flexible chirp-free probe pulse amplification for kHz fs/ps rotational CARS, Opt. Lett. 45 (2020) 503.

[134] Erik L. Braun, Kazi Arafat Rahman, Venkat Athmanathan, Mikhail N. Slipchenko, Sukesh Roy, Terrence R. Meyer,High-Energy Flexible Probe Pulse Generation for kHz fs-ps Rotational Coherent Anti-Stokes Raman Scattering. Opt. Sensors Sens. Congr. OSA Tech. Dig., Washington D.C. (2020) .

[135] F. Ornano, J. Braun, B.H. Saracoglu, G. Paniagua, Multi-stage nozzle-shape optimization for pulsed hydrogen-air detonation combustor, Adv. Mech. Eng. 9 (2017) 1–9.

[136] J. Braun, J. Sousa, G. Paniagua, Numerical Assessment of the Convective Heat Transfer in Rotating Detonation Combustors Using a Reduced-Order Model, Appl. Sci. 8 (2018) 893.

[137] C.F. Lietz, Y. Desai, W. Hargus, V. Sankaran,Parametric investigation of rotating detonation rocket engines using large eddy simulations. AIAA Propuls. Energy Forum Expo. 2019, American Institute of Aeronautics and Astronautics Inc, AIAA (2019) .

[138] H.U. Stauffer, J.D. Miller, M.N. Slipchenko, T.R. Meyer, B.D. Prince, S. Roy, et al., Time- and frequency-dependent model of time-resolved coherent anti-Stokes Raman scattering (CARS) with a picosecond-duration probe pulse, J. Chem. Phys. 140 (2014) 1–16.

[139] C.E. Dedic,Hybrid fs/ps coherent anti-Stokes Raman scattering for multiparameter measurements of combustion and nonequilibrium. Iowa State University (2017) .

[140] K.A. Rahman,Non-linear ultrafast-laser spectroscopy of gas-phase species and temperature in high-pressure reacting flows. Purdue University Graduate School (2019) .

[141] S. Roy, T.R. Meyer, R.P. Lucht, M. Afzelius, P.-E. Bengtsson, J.R. Gord, Dual-pump dual-broadband coherent anti-Stokes Raman scattering in reacting flows, Opt. Lett. 29 (2004) 1843.

[142] A.H. Lefebvre, D.R. Ballal,Gas Turbine Combustion. 3rd ed. CRC Press (2010) .

PUBLICATIONS

Accepted Journal Papers

Athmanathan, V., Rahman, K., Lauriola, D., Braun, J., Paniagua, G., Slipchenko, M., Roy, S., & Meyer, T. (2021). Femtosecond/picosecond rotational coherent anti-Stokes Raman scattering thermometry in the exhaust of a rotating detonation combustor. Combust. Flame, 231, 111504.

Douglawi, A., **Athmanathan, V.,** Slipchenko, M., Gord, J., & Meyer, T. (2019). Lifetime-filtered laser-induced exciplex fluorescence for crosstalk-free liquid-vapor imaging. Optics Letters, 44(6), 1399–1402.

Rahman, K., **Athmanathan, V.,** Slipchenko, M., Roy, S., Gord, J., Zhang, Z., & Meyer, T. (2019). Quantitative femtosecond, two-photon laser-induced fluorescence of atomic oxygen in high-pressure flames. Applied optics, 58(8), 1984–1990.

Rahman, K., **Athmanathan, V.,** Slipchenko, M., Meyer, T., & Roy, S. (2019). Pressure-scaling characteristics of femtosecond two-photon laser-induced fluorescence of carbon monoxide. Applied optics, 58(27), 7458–7465.

Smyser, M., Braun, E., **Athmanathan, V.,** Slipchenko, M., Roy, S., & Meyer, T. (2020). Dual-output fs/ps burst-mode laser for megahertz-rate rotational coherent anti-Stokes Raman scattering. Optics Letters, 45(21), 5933–5936.

Saavedra, J., **Athmanathan, V.,** Paniagua, G., Meyer, T., Straub, D., Black, J., & Ramesh, S. (2021). Scalable Heat Transfer Characterization on Film Cooled Geometries Based on Discrete Green's Functions. Journal of Turbomachinery, 1–24.

Yokoo, R., Goto, K., Kasahara, J., **Athmanathan, V**., Braun, J., Paniagua, G., Meyer, T., Kawasaki, A., Matsuoka, K., Matsuo, A., & others (2020). Experimental study of internal flow structures in cylindrical rotating detonation engines. Proceedings of the Combustion Institute.

Hsu, P., Slipchenko, M., Jiang, N., Fugger, C., Webb, A., **Athmanathan, V.,** Meyer, T., & Roy, S. (2020). Megahertz-rate OH planar laser-induced fluorescence imaging in a rotating detonation combustor. Optics Letters, 45(20), 5776–5779.

Manuscripts under preparation

Athmanathan, V., Braun, J., Ayers, Z., Webb A., Paniagua, G., Fugger, C., Roy, S. & Meyer, R. T., On the nature and origin of trailing detonation waves within annular combustion channels revealed by simultaneous MHz-rate OH-PLIF/ OH* chemiluminescence and numerical simulations. *(manuscript under review in Combustion and Flame)*

Athmanathan, V., Ayers, Z., Fugger, C., Roy, S. & Meyer, R. T., Transverse waves, and cellular propagation in non-premixed RDCs *(manuscript under review in short communication - Combustion and Flame)*

Athmanathan, V., Braun, J., Ayers, Z., Webb A., Paniagua, G., Fugger, C., Roy, S. & Meyer, R. T., Detonation structure investigations in straight and expanding annular combustors. *(manuscript under preparation for review in Combustion and Flame)*

Conference Proceedings

Rahman, K., **Athmanathan, V.,** Slipchenko, M., Meyer, T., Roy, S., & Gord, J. (2019). Pressure scaling of spatiotemporally resolved femtosecond two-photon laser-induced fluorescence of CO. In AIAA SciTech 2019 Forum (pp. 0571).

Douglawi, A., **Athmanathan, V.,** Ma, J., Slipchenko, M., Meyer, T., & Gord, J. (2019). Two-phase flow imaging of evaporating fuel droplets with temporally filtered laser-induced exciplex fluorescence. In AIAA SciTech 2019 Forum (pp. 0572).

Athmanathan, V., Fisher, J., Ayers, Z., Cuadrado, D., Andreoli, V., Braun, J., Meyer, T., Paniagua, G., Fugger, C., & Roy, S. (2019). Turbine-integrated High-pressure Optical RDE

(THOR) for injection and detonation dynamics assessment. In AIAA Propulsion and Energy 2019 Forum (pp. 4041).

Athmanathan, V., Braun, J., Ayers, Z., Fisher, J., Fugger, C., Roy, S., Paniagua, G., & Meyer, T. (2020). Detonation structure evolution in an optically-accessible non-premixed H2-Air RDC using MHz rate imaging. In AIAA SciTech 2020 Forum (pp. 1178).

Braun, E., Rahman, K., **Athmanathan, V.,** Slipchenko, M., Roy, S., & Meyer, T. (2020). High-Energy Flexible Probe Pulse Generation for kHz fs-ps Rotational Coherent Anti-Stokes Raman Scattering. In Laser Applications to Chemical, Security and Environmental Analysis (pp. LTu5C–3).

Fugger, C., Hsu, P., Jiang, N., Roy, S., Slipchenko, M., **Athmanathan, V.,** Webb, A., Fisher, J., & Meyer, T. (2021). Megahertz OH-PLIF Imaging in a Rotating Detonation Engine. In AIAA SciTech 2021 Forum (pp. 0555).